Performance under Pressure: Effect of Pumping Pressure on Additive Manufacturing of Lightweight Aggregate Concrete

Carla Matthäus
Technical University of Munich

Technische Universität München
TUM School of Engineering and Design

Performance under pressure: Effect of pumping pressure on additive manufacturing of lightweight aggregate concrete

Carla Irmgard Ingeborg Matthäus

Vollständiger Abdruck der von der TUM School of Engineering and Design der Technischen Universität München zur Erlangung des akademischen Grades einer Doktorin der Ingenieurwissenschaften (Dr.-Ing.) genehmigten Dissertation.

Vorsitz:	Prof. Dr.-Ing. Stefan Winter
Prüfer:innen der Dissertation:	1. Prof. Dr.-Ing. Christoph Gehlen
	2. Prof. Dr. Kathrin Dörfler

Die Dissertation wurde am 16.03.2022 bei der Technischen Universität München eingereicht und durch die TUM School of Engineering and Design am 20.06.2022 angenommen.

Acknowledgements

I want to express my sincere gratitude to my supervisor Christoph Gehlen for his feedback and for the possibility to take responsibility and follow my research interests during my time at the chair. I am grateful to Klaudius Henke and Daniel Talke for awakening in me the interest for the topic of additive manufacturing, for the fruitful collaboration in the research project, and for always being available for an advice. I am indebted to Daniel Weger and Thomas Kränkel for introducing me to material science, for supporting and cheering me up in frustrating phases, and providing me with valuable feedback and advice in academia and beyond.

Thanks to Kathrin Dörfler for the exchange, for forging ideas together, and for insights into the fascinating world of architecture. Many thanks also to Alisa Machner for being a role model, for great zoom-sessions, and for giving me an outstanding insight into how to work in the academic environment.

I want to thank Bettina Saile for her great support in the lab, for always thinking along and giving good advice. A big thanks also to Klaus Linz, Maik Hobusch and Barnabas Omozkopia for their great support in the lab, for their long working hours, and their endurance when having to clean after the pump tests. I also want to thank the students and student assistants who supported me with their great work: Matthias Dichtl, Lisa Forstmaier, Christoph Kaindl, Ronja Behnsen, Fabian Berndl and Max Dik. I am grateful to my colleagues, especially Mareike Thiedeitz, Fabian Diewald, Alexander Straßer and Maximilan Hechtl for great discussions, for inspiring new ideas, and for sharing sweets when needed.

A very special thanks to my family! Thanks Anke, Reinhard, Riccarda, Adrian, Philipp, Angelika, Konrad, Maren, and Johanna for supporting every project of mine, for suffering with me and cheering me up, for welcome distraction, for pragmatic input, and for making so many things possible in my life. From the bottom of my heart, I thank my husband David for the balance, joy and hope in my life, for bringing out the best in me and releasing energy that I forgot I have, for indispensable input, discussions, and proof-reading. Thank you for being my travel companion in life.

Abstract

Additive manufacturing enables the production of customized building components, which use material consciously depending on the function of the building components, e.g., the thermal insulation. The distinctive benefit of lightweight aggregate concrete lies in the combination of insulating and load-bearing properties. For successful use of lightweight concrete in additive manufacturing, here with a focus on concrete extrusion, the fresh material properties need to be adjusted to the specific, partly conflicting requirements of all phases of the extrusion process. Particularly, the requirements for pumping and layer-wise construction oppose each other.

In addition to the requirements arising from the individual phases, the evolution of material (e.g. stiffening) during the different phases must also be taken into account. In lightweight concrete, pumping pressure affects the fresh material properties. The causes and effects of these changes on the further extrusion process, in particular on buildability, are elucidated in this thesis.

It was found in this thesis that the density and the yield stress of lightweight aggregate concrete change under the pressure applied during pumping. Experiments show that this is caused by an increased water absorption and, irreversibly, by a slight surface destruction combined with ingress of cement paste into the lightweight aggregates under increased pressure. These changes in density and yield stress lead to a lower insulation capacity of the material, but at the same time to a significant improvement in buildability, i.e., more layers can be deposited in a shorter time without causing failure of the extruded element.

Based on existing predictive models for normal weight concrete, a model and associated test regime was developed to predict buildability, which incorporate the influence of pressure on the material. The newly developed approach enables to evaluate new materials for extrusion with less effort and, with regard to lightweight concrete, higher accuracy than existing models. It contributes to a simplified estimation of buildability, with a focus on feasible construction speeds, and necessary process parameters.

Kurzfassung

Additive Fertigung ermöglicht die Herstellung von individualisierten Bauteilen, bei denen Material bewusst angepasst an die Funktion des Bauteils eingesetzt wird. Ein besonderer Vorteil von Leichtbeton liegt in der Verbindung von Dämm- und Tragfähigkeit. Für den erfolgreichen Einsatz von Leichtbeton in der additiven Fertigung, hier mit Fokus auf die Betonextrusion, müssen die Frischbetoneigenschaften auf die spezifischen, teils widersprechenden Anforderungen aller Phasen des Extrusionsprozesses abgestimmt werden. Insbesondere die Anforderungen des Pumpens und des schichtweisen Ablegens stehen im Widerspruch.

Neben den Anforderungen, die sich aus den einzelnen Phasen ergeben, muss auch die Entwicklung des Materials innerhalb der Phasen berücksichtigt werden. Die Frischbetoneigenschaften von Leichtbeton werden z.B. durch den Pumpendruck beeinflusst. Die Ursachen und Auswirkungen dieser Veränderungen auf den weiteren Extrusionsprozess, insbesondere auf die Baubarkeit, werden in dieser Arbeit dargelegt.

Die Arbeit zeigt, dass sich die Rohdichte und die Fließgrenze von Leichtbeton unter dem beim Pumpen aufgebrachten Druck verändern. Es konnte experimentell gezeigt werden, dass dies durch eine erhöhte Wasseraufnahme und, irreversibel, durch eine geringfügiges Aufrauen der Oberfläche in Verbindung mit dem Eindringen von Zementleim in die Leichtzuschläge unter Druck verursacht wird. Diese Änderungen führen zwar zu einer Verringerung der Dämmwirkung, aber zu einer deutlichen Verbesserung der Baubarkeit, d. h. einer höheren Baugeschwindigkeit ohne ein Versagen des extrudierten Elements auszulösen.

Auf Grundlage bestehender Prognosemodelle für Normalbeton wurden ein Modell und ein zugehöriges Prüfverfahren zur Vorhersage der Baubarkeit entwickelt, die den Einfluss des Pumpendrucks auf das Material berücksichtigen. Der neu entwickelte Ansatz ermöglicht es, Materialien für die Extrusion mit weniger Aufwand und, im Hinblick auf Leichtbeton, mit höherer Genauigkeit zu bewerten und trägt zu einer vereinfachten Abschätzung der erreichbaren Baugeschwindigkeiten bei.

Table of Contents

List of Figures

List of Tables

List of Symbols

Symbol	Unit	Parameter	Symbol	Unit	Parameter
a	[-]	Amount of layers	t_p	[s]	Plastic failure time
A	[m^2]	Cross-section area	t_r	[s]	Re-flocculation time
A_{Blaine}	[cm^2/g]	Specific surface	t_{rest}	[s]	Time at rest
Ag	[kg]	Aggregate content	t_t	[s]	Object realization time
A_{thix}	[Pa/s]	Structuration rate	v	[m/s]	Velocity of printing head
C	[kg]	Cement content	V_{air}	[m^3]	Air void content
$C(t)$	[kN/m^2]	Cohesion	V_p	[m^3]	Paste volume
D_0	[−]	Initial bending stiffness	v_r	[min^{-1}]	Speed of rotation
d_50	[μm]	mean particle size	w	[kg]	Mixing water
E	[Pa]	Young's modulus	w_a	[kg]	Water absorption
E_0	[Pa]	Initial Young's modulus	w_t	[kg]	Total water
e_1, e_2, t_c	[−]	Fitting variables	$(w/b)_{eff}$	[−]	Effective water-to-binder ratio
g	[m/s^2]	Gravity constant			
h_i	[m]	Layer height	α_{geom}	[−]	Geometrical factor
h_v	[mm]	Vane-in-cup height	$\dot{\gamma}$	[s^{-1}]	Shear rate
H_{cr}	[m]	Critical height	δ_i	[m]	Layer width
$H_{f,b}$	[m]	Buckling failure height	δ	[m]	Object width
$H_{f,p}$	[m]	Plastic collapse height	λ	[W/mK]	Thermal conductivity
H_t	[m]	Object height	μ	[Pa · s]	Viscosity
I	[m^2]	2nd moment of area	ν	[−]	Poisson rate
k	[−]	Flow coefficient	ξ_E	[s^{-1}]	Curing rate in elasticity
l_i	[m]	Layer length	$\xi_{\sigma,c}$	[s^{-1}]	Curing rate in compression
$\dot{l}$	[s/layer]	Time per layer			
L	[m]	Object length	ρ	[kg/m^3]	Density
M	[Nm]	Torque	ρ_f	[kg/m^3]	Fresh concrete density
n	[−]	Flow index	σ_c	[Pa]	Green strength
P	[bar]	Pressure	σ_v	[Pa]	Induced vertical stress
$\dot{P}$	[bar/s]	Increase in Pressure	$\tau(t)$	[Pa]	Shear stress
Q	[l/min]	Flow rate	τ_0	[Pa]	Yield stress
r_v	[mm]	Radius of vane device	$\tau_{0,D}$	[Pa]	Dynamic yield stress
R_{thix}	[Pa/s]	Re-flocculation rate	$\tau_{0,S}$	[Pa]	Static yield stress
$\dot{s}$	[m/s]	Vertical building rate	ϕ	[°]	Friction angle
t_e	[s]	Time of exposure	Φ_{fill}	[%]	Pore filling
t_h	[s]	Low structuration time	Φ_{void}	[−]	Open void fraction
t_m	[s]	Min. object real. time	Ω	[rad/s]	Rotational speed

1 Introduction

Additive manufacturing (AM, popularly 3D-printing) is set to become a disruptive technology as it promises enlarged architectural possibilities by a high level of freedom of form and customization, a reduction of manual labor and associated negative health impacts, a reduction of resource consumption and an improvement in quality and velocity of built structures (Wangler et al., 2016; Tay et al., 2017; de Schutter et al., 2018; Perrot, 2019; Wangler et al., 2019). A cornerstone of this vision is the development of suitable materials for the AM processes.

One of the first trials in additive manufacturing for constructions was already conducted in the 1930s and 1940s by building a wall layerwise with a machine (Urschel's wall, Urschel and Urschel (1941)). The idea was rediscovered in the 90s by Pegna (1997) conducting particle-bed based additive manufacturing approaches and by Khoshnevis (1999) deposing concrete strands. In the last decade, there happened an exponential growth of research and applications in the field. A historical outline and an overview of projects of additive manufacturing in construction can be found in existing literature, e.g. Lim et al. (2012); Henke (2016); Bos et al. (2016); Camacho et al. (2018); Paolini et al. (2019); Sartipi and Sartipi (2020).

Additive manufacturing in that sense is defined as the automatic successive joining of small volumes of material and can be described as a layered construction method. Nowadays, it is mainly based on a digital model. Even though other materials are 3D-printable, e.g., glass, ceramics or plastics, the additive manufacturing for construction is dominated by concrete as building material. Concrete as a building material which goes naturally from a fluid to a solid state gives great flexibility in terms of material handling and placing. In additive manufacturing, the potential of concrete and cementitious materials can be exploited even better.

Common technologies for AM in construction are divided into depositing technologies, e.g., extrusion and shotcrete-3D-printing, as well as selective binding technologies, which are particle-bed based, see Figure 1.1. A summary and classification of the available techniques can be found

in Buswell et al. (2020). They vary in building rate, freedom of form, resolution and precision. This thesis focuses on the extrusion of concrete.

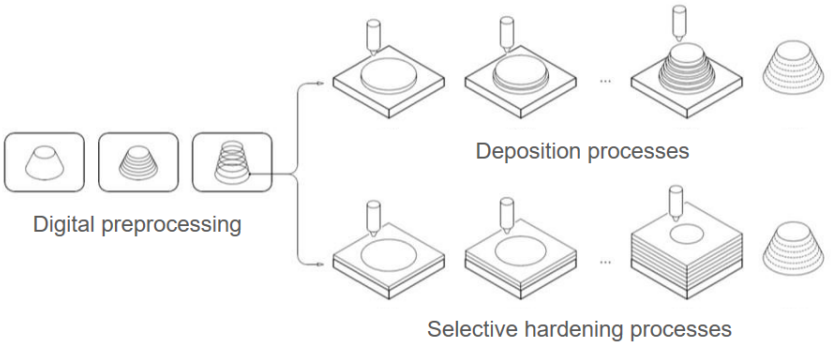

FIGURE 1.1: Scheme of depositing and selective binding AM technologies according to (Henke, 2016)

Additive manufacturing enables to integrate multiple functions and to use material consciously depending on the function of the building components. A successful qualification of lightweight concrete for AM can open even more possibilities for application and function integration than with normal weight concrete only. A distinctive benefit of lightweight aggregate concrete lies in the combination of insulating and load-bearing properties.

Lightweight concrete is not an invention of modern times, but was already used by the romans for the Pantheon, which was constructed by tuff lightweight concrete with a density between 1350 $\frac{kg}{m^3}$ and 1600 $\frac{kg}{m^3}$ with decreasing density towards the top of the building (Mark and Hutchinson, 1986). Wesche (1993) states that the main advantages of lightweight concrete are: lower dead weight of the components, lower transport and assembly weight, better thermal insulation, lower thermal expansion, good damping of vibrations and earthquakes due to low Young's modulus, lower steel requirements and smaller foundation dimensions. Furthermore, building at low temperatures is possible due to slower drainage of the hydration heat. With regard to functional application, lightweight concrete provides good airborne sound insulation due to its porous structure and is favorable for fire resistance. Using lightweight concrete, the dead weight of building components can be reduced by approximately 20-25 % in comparison to normal weight concrete (Wesche, 1993). Thus, adding storeys to buildings or existing structures is easier than with normal weight concrete. The low thermal conductivity of lightweight concrete enables an easier fulfillment of building physics requirements without complex sandwich construction. This can also lead to better recyclability of the elements in comparison to the combination of normal weight concrete and insulation. Note that 3D-printing the building with one material

facilitates the freedom of form and reduces the number of working steps in comparison to a multi-layered construction. However, these advantages are also offset by some disadvantages such as high costs for aggregates, high cement content for extrusion, difficulties with pumping, limited strength (lower tensile and shear strength as well as lower strength at local surface loading than normal weight concrete), and greater required care in production and quality assurance. These disadvantages need to be addressed during material qualification for extrusion.

Lightweight concrete has rarely been used for extrusion up to now. First investigations cover wood chip lightweight concrete extrusion (Winter et al., 2016; Henke et al., 2016, 2017). Furthermore, investigations on lightweight aggregate concrete have been conducted in the associated research project to this thesis (Matthäus et al., 2019, 2020, 2021). In addition, tests on foamed lightweight concrete for 3D-printing (Falliano et al., 2020), tests on lightweight structures (Li Wang et al., 2020) and first investigations with lightweight concrete conveyed by a piston pump (Rahul and Santhanam, 2020) have been performed. They mainly focus on application areas and mechanical strength of lightweight structures.

In this thesis, the suitability of lightweight aggregate concrete is analyzed for extrusion from a material science perspective. For successful use of lightweight aggregate concrete in additive manufacturing, the fresh material properties need to be adjusted to the specific, partly conflicting requirements of the extrusion process. The extrusion of concrete includes the delivery of fresh concrete to the nozzle, the deposition, which is spatially controlled by a manipulator, and the layerwise construction of the desired object by stacking the deposited strands on top of each other. The process is divided into four phases for a better overview: mixing and pumping, deposition, layer-by-layer construction as well as hardening and curing. The phases and the requirements in each phase are summarized in Figure 1.2.

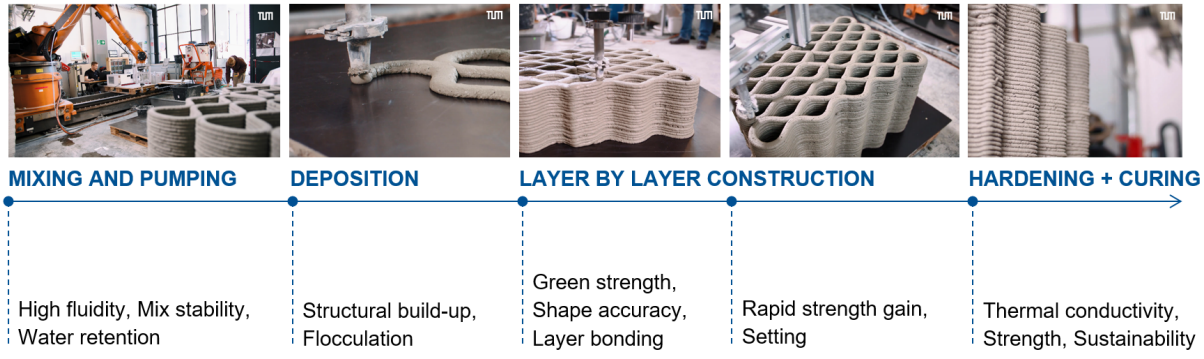

Figure 1.2: Phases of lightweight concrete extrusion and its related requirements on the concrete

Overall, the main requirements in the first phase can be referred to as 'pumpability' and in the layer-by-layer construction as 'buildability'. In contrast to normal weight concrete, the lightweight aggregates change the fresh material properties noticeably during the pumping phase, especially the density and the rheology. The main objectives of this thesis are

1. to analyze whether lightweight concrete is suitable for extrusion,
2. to investigate the material properties and their change during extrusion, especially how pumping pressure affects the performance of lightweight concrete in extrusion,
3. and to assess the effect of these changes on buildability and failure prediction of 3D-printed construction elements.

To achieve these goals, experimental tests are performed and existing models are extended. The investigations cover three scales: On a micro scale the lightweight aggregates are analyzed, on a meso scale tests are performed on lightweight aggregate concrete to determine fresh and hardend properties and on a macro scale the pumpability and buildability of the lightweight aggregate concrete is investigated, see Figure 1.3.

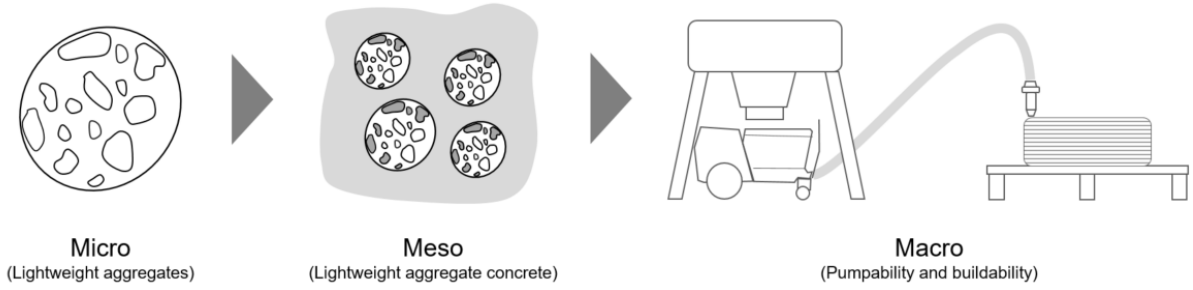

FIGURE 1.3: Scales of investigation

The thesis is divided into three main chapters and a summary. It is structured as follows: Chapter 2 provides background on the state of the art in normal weight concrete extrusion as there is not yet information on material requirements or prediction models especially for lightweight concrete extrusion. It is hypothesized that basic concepts of normal weight concrete extrusion are also valid for lightweight concrete extrusion. Thus, basic information on requirements in the individual phases of extrusion, on buildability models, and on conflicting design goals are presented on which to build when considering lightweight concrete. Furthermore, the fundamentals on rheology are summarized with focus on the parameters relevant for concrete extrusion.

Finally, information on lightweight concrete, in particular on its pumpability and the water absorption of lightweight aggregates, is compiled.

Chapter 3 gives an overview on the methods applied including materials, mix design, and test procedures. Chapter 4 presents the results of the experiments and the associated discussion. The key drivers for the increase in density are investigated and identified in Section 4.1 and Section 4.2. Section 4.3 presents the implications on pumpability. Furthermore, the effect of the increase in density on the buildability as well as the applicability of buildability models developed for normal weight concrete is analyzed (Section 4.4). Based on this, a model and associated test regime for buildability prediction is developed, which includes the influence of pumping pressure on the material properties. With regard to possible application areas, the effect of changes during pumping on hardened concrete properties is shortly presented in Section 4.5. Finally, Chapter 5 provides a summary and outlook for future research on extrusion of lightweight concrete.

Overall, this thesis focuses on the relationship between lightweight concrete rheology, pumping pressure and buildability. The understanding of this relationship is crucial for material optimization, process development, modelling, and design of lightweight concrete for extrusion, and thus, for future interdisciplinary research and application.

2 Theoretical background

2.1 Basics of concrete extrusion

Only by understanding the basics of the extrusion process, one acknowledge the challenges during material development for extrusion. The extrusion of concrete includes the delivery of fresh concrete to the nozzle, the deposition which is spatially controlled by a manipulator and the layerwise construction of the desired object by stacking the deposited strands on top of each other. The process is again divided into four phases: mixing and pumping, deposition, layer-by-layer construction as well as hardening and curing. The phases are schematically depicted in Figure 2.1.

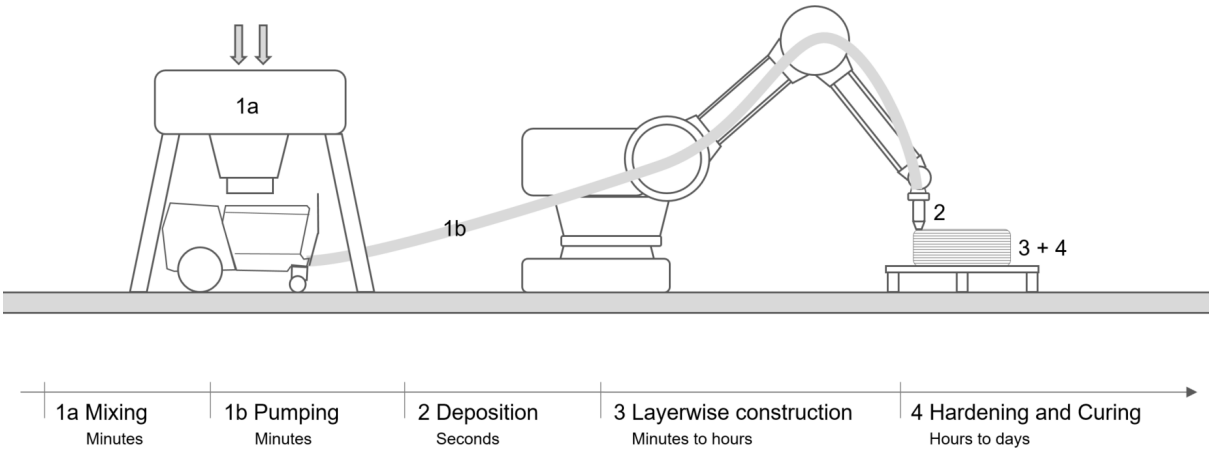

FIGURE 2.1: Phases and respective duration of the extrusion process

Based on literature (e.g., Le et al., 2012a; Lim et al., 2012; Marchon et al., 2018; Roussel, 2018) and practical investigations, the requirements in the different phases are summarized in the following. Each phase will be discussed in more detail in the following sections 2.3.1 to 2.3.5.

Mixing is not considered as a separate category as the requirements in this phase are not special for concrete extrusion in comparison to conventional techniques. In general a homogeneous mixing and even distribution of the materials is aimed for and assumed for this work.

Phase 1, Pumping: The rheological properties of the fresh concrete determine its workability, mixing stability and robustness. The required properties are strongly dependent on the process (e.g. the way the material is conveyed). To ensure that the material is conveyable and that the hose or the nozzle are not blocked, a time window for printability must be defined (Kazemian et al., 2017). This corresponds to the time required to mix, convey and discharge the material (phases 1 and 2). The open time of the concrete, i.e. the time between mixing and setting, must at least correspond to the printability time window plus the operation window (see phase 3). The main requirement in this phase can be referred to as 'pumpability'. Pumpability is defined as the ease with which a material moves through a delivery system (Le et al., 2012a; Lim et al., 2012).

Phase 2, Deposition of the first layer: Phase 2 covers the deposition of the material. The requirements at deposition are in a conflict between the diametrically opposed requirements for the conveying phase and for the construction phase where the load bearing and contour accuracy of the layers is targeted. Immediately after deposition, the strand must be able to bear its own weight and retain its shape (see Section 2.3.2). In order to avoid deformations, the internal structure of the material should start to build up as soon as the material is at rest, which continues until solidification in phase 4. The speed and amount of this time-dependent structural build-up in the deposited strands limits the achievable component height (see Section 2.3.2). In order to solve the conflict between flowability and load-bearing, the use of a thixotropy enhancing material that behaves in a shear-thinning manner during shear (conveying) and rebuilds a structure at rest (after deposition) as a function of time might be favorable (Roussel, 2006). In this phase, the process characteristics are decisive parameters. The nozzle shape, the printing speed and the pressure which is applied during deposition affect the material behavior. Thus different material characteristics are needed depending on the process characteristics.

Phase 3, Layer-by-layer construction: After the deposition of the first layer, the subsequent layers are deposited. The time between the layers (layer cycle time) depends on the printing speed and the layer length. The load of the subsequent layers acts on the lower layers. In addition to the green strength and the structural build-up, shape accuracy is essential in phase 3. The main requirement in this phase is referred to as 'buildability'. Buildability indicates the ability of a material to bear its own weight and the weight of subsequent layers and thus allows for layerwise

construction without formwork (Le et al., 2012a; Lim et al., 2012). Defining the buildability as the ability to bear loads, deformation is included in that category. This ultimately has a strong influence on the achievable freedom of shape and precision of the component. With optimal shape accuracy, neither the dead weight nor the applied loads would cause deformations and the material would retain the shape obtained during deposition. However, in order to ensure a good layer bonding between the deposited layers, the material must not yet have solidified. The layer bonding is significantly dependent on the time span between the placement of the individual layers (cf. Section 2.3.4). The faster the next layer is deposited, the better the layers bond between the two as the hydration might still occur across the layers. Depositing "fresh in fresh" is therefore aimed for (Panda et al., 2017; Roussel, 2018). However, the achieved green strength of a layer and the resulting possibility of bearing the weight of subsequent layers is higher, the longer the time between the deposition of two layers. In the literature, this is referred to as an operation window (Wangler et al., 2016), which defines the period in which the next layer can be printed. The operation window is limited by workability loss due to restricted open time and green strength development (Lim et al., 2012) and must be selected accordingly so that both aspects are fulfilled and the best possible final strength and shape accuracy of the component can be achieved, see Section 2.3.2. Phase 3 thus clearly determines the freedom of shape that can be achieved within the process.

Phase 4, Hardening and curing: In phase 4 the concrete in the respective layer first sets and then hardens. During setting, the yield stress increases and during hardening, the strength increases rapidly. In this phase it is essential to achieve the required hardened concrete properties. To this end, it must be ensured that the reactions are controlled and that the shape accuracy as well as the surface quality are still guaranteed.

In contrast to 3D-printing with synthetic materials (e.g., Fused Layer Modeling), each layer is in a different state during the concrete extrusion process. This is due to the time-dependent structural build-up and hardening. The lowest layers will thus reach the hardened state earlier than later deposited layers. The hardened concrete properties are influenced by the material composition and the reaction times. This will be discussed in Section 2.3.4. However, the main challenge lies in the building process itself.

With regard to the material, the major process parameter is the building rate, i.e. the speed with witch a building component is manufactured. The building rate influences significantly the success of the process as it affects the speed at which the next layers are deposited (Le et al., 2012a; Lloret et al., 2015) and thus the requirements on buildability. Furthermore, it determines

the amount of material needed at a time and thus the pumping speed, which itself determines the requirements for pumpability.

Pumpability and buildability are often summarized in literature by a category called extrudability or printability defining the suitability for extrusion in total. However, the term is also used in literature to complement the categories defining the ease of deposition through a nozzle. In the thesis at hand, the ease of deposition is subsumed under pumpability and the terms extrudability and printability are used for the global phenomenon. While pumpability and buildability are focusing on the fresh material and are leading to strong requirements on the rheology of the material, the hardened concrete properties focus on the properties of the finished element.

2.2 The role of rheology in concrete extrusion

Rheological properties characterize the complex behavior of the fresh lightweight concrete in the extrusion process. This thesis focuses on the rheological parameters that are significant for concrete extrusion—namely, static and dynamic yield stress, viscosity, thixotropy, and structuration. Detailed descriptions on the fundamentals of rheology of concrete as well as explanations on their background can be found in literature (e.g., Haist, 2010; Lowke, 2013; Mezger, 2016).

The **yield stress** is the shear stress, that is necessary to set a material into motion (static yield stress) or keep a material in motion (dynamic yield stress). The static yield stress $\tau_{0,S}$ corresponds to the breakage of the network of colloidal interactions (Roussel et al., 2012) and defines the flow onset on a macroscopic level (Tattersall and Banfill, 1983). It must be distinguished from a second type of static yield stress which corresponds to the end of the linear elastic material behavior and on a microscopic level to the breakage of early hydrates (Roussel et al., 2012). This work focuses on static yield stress $\tau_{0,S}$ in terms of flow onset, not on the end of the linear elastic regime. The static yield stress $\tau_{0,S}$ is a measure of the strength of the resting structure and is larger than the dynamic yield stress $\tau_{0,D}$ which reflects the state of equilibrium of the material after breaking the structure (Lowke, 2013).

The yield stress of extruded materials is governed by the behavior of its cement paste and thus by attractive interactions between particles (flocculation) as well as by the growth of hydration products. In general, flocculation is a reversible process while hydration is an irreversible process. Reversibility is assessed in the following with regard to thixotropy.

The static yield stress $\tau_{0,S}$ of the material is mainly relevant for buildability as it defines the resistance of the material to loads and deformation. In terms of pumpability, it is only relevant with regard to the force that is needed for the material to start flowing. However, the dynamic yield stress $\tau_{0,D}$ might be of relevance for pumpability.

The **viscosity** results from friction between particles when moved relatively to each other—the higher the friction, the higher the viscosity. Different types of viscosity must be distinguished: dynamic, plastic, and apparent viscosity. Concrete is a non-Newtonian material as it has a yield stress. Hence, dynamic viscosity, which is only valid for Newtonian fluids, will be disregarded. For non-Newtonian fluids the so-called plastic viscosity $\mu(\dot{\gamma})$ is a function of the shear rate $\dot{\gamma}$ and describes the material properties after exceeding the dynamic yield stress. The plastic viscosity μ is not dependent on the duration of the shear, but only on the shear rate (Mezger, 2016).

Depending on the mixture proportioning and the applied shear stress, concrete can behave in shear thinning, Bingham, or shear thickening manner. The plastic viscosity is the slope of the flow curve in a τ-$\dot{\gamma}$-diagram. With increasing shear rate a shear thinning mixture displays a decreasing plastic viscosity, whereas a Bingham material has a constant plastic viscosity μ_B at varying shear rate and a shear thickening material displays an increasing plastic viscosity with increasing shear rate, see Figure 2.2. Concrete might also have a dilatant material behavior which is shear thinning up to a critical shear rate and shear thickening above this critical shear rate. Below the critical shear rate inter-particle forces dominate while above it hydrodynamic effects and the friction between particles are decisive (Galindo-Rosales et al., 2011).

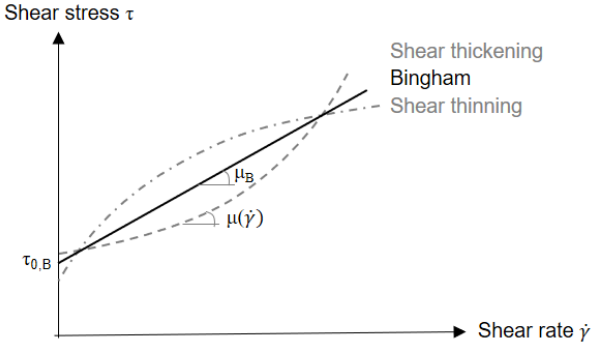

FIGURE 2.2: Flow curve for non-Newtonian material

For shear dependent materials (i.e. shear thickening or shear thinning), the viscosity is not a material constant, but depends on the applied shear rate $\dot{\gamma}$. The plastic viscosity is a measure

of cohesion and as a consequence affects the stability of the material. Thus it has an particularly important effect on the particle migration and the formation of a lubrication layer during pumping, see Section 2.4.4.

Thixotropy is a time dependent material behavior. It describes the reversible reduction of viscosity and yield stress due to destruction of the microstructure under shear followed by a structural build-up through formation of an internal structure at rest, see Figure 2.3.

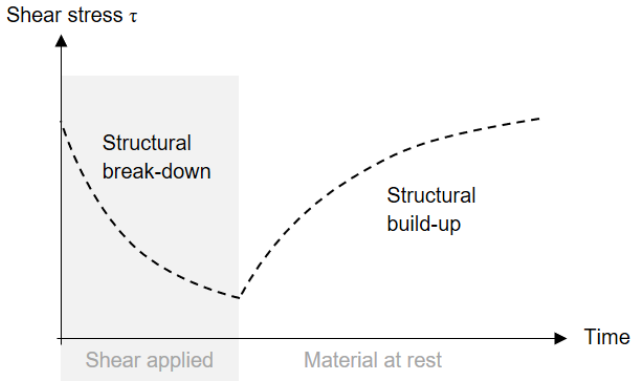

FIGURE 2.3: Scheme of thixotropic material behavior

In relation to concrete it should be noted that thixotropy describes a reversible material behavior on a macroscopic perspective (Lapasin et al., 1983; Papo, 1988; Barnes et al., 1989; Roussel et al., 2005; Roussel, 2006). Opinions differ on whether it is a completely reversible process on all levels (Wallevik, 2005) or whether the effects on a microscopic level might be partly irreversible considering the breakage of early hydrates (Roussel, 2006; Lowke, 2013). Early hydrates can reform spontaneously within a couple of seconds at rest (Jiang et al., 1995; Nonat et al., 1997; Roussel et al., 2012). According to Roussel et al. (2012) the thixotropy is influenced both by colloidal interactions, e.g., van der Waals attractive forces and by CSH nucleation. Following this theory, there is a short term thixotropy (few seconds) due to colloidal flocculation and a long term thixotropy due to ongoing hydrates nucleation which is build-up within 30 to 100 s (Roussel et al., 2012). Over large time spans, the hydration processes dominate the reversible physical and chemical processes (Kovler and Roussel, 2011). After some time these developments start to be irreversible. At least at the start of solidification the amount and strength of connections between the particles is so high that the process is not reversible even at high shear rates and thus limits the thixotropic effects in time (Lowke, 2013).

With regard to extrusion, thixotropy is important for pumpability and the deposition of the first layers. When the material is sheared in the pump, its viscosity and yield stress decrease and

when the material is deposited, the structure rebuilds.

In this thesis, the term **structuration** will be used to describe the evolution of yield stress over time at rest. It includes thixotropy and early hydration processes before setting. During the dormant period of the hydration reaction, the static yield stress continuously increases over time (Tattersall and Banfill, 1983; Barnes et al., 1989; Roussel et al., 2005). The structuration and its velocity is crucial for buildability as it limits the printing speed, see Section 2.3.2.

Different measures to increase the structuration during the layerwise construction process have been studied by, e.g., Marchon et al. (2018); Reiter et al. (2018). They range from short-term increases of the structuration over chemically inert admixtures to accelerators. The short-term structuration is influenced, e.g., by the interaction with superplasticizers, the water absorption or an increase in viscosity (Brumaud et al., 2014; Bessaies-Bey et al., 2016; Palacios and Flatt, 2016; Reiter et al., 2018). As superplasticizers decrease interparticle forces and lead to less space for early hydration products on the cement particles (Roussel, 2012), a low amount of superplasticizer is recommended for the building phase during extrusion. Furthermore, the addition of, e.g., nano silica, polymers or clay minerals (Lowke, 2013) is suitable in terms of short-term structuration (thixotropy).

Besides, for larger time scales the structural build-up increases with increasing solid fraction in the cement paste or increasing fineness of cement and additives (e.g., silica fume or fine limestone powder). Chemically inert admixtures modify the flocculation by changing the effective solid content, e.g., VMAs (Khayat and Mikanovic, 2012) or nanoclays. Finally, accelerator, e.g., inorganic salts, shotcrete accelerators or CSH-seeds as well as increasing temperatures also lead to enhanced structuration (Petit et al., 2006), mainly by an accelerated hydration.

In summary, the required rheological properties during extrusion are as follows: for mixing and pumping a low viscosity and yield stress is favorable. Among others, this can be achieved by a material with thixotropic properties. At deposition the yield stress must be sufficiently high to withstand deformation. During the layerwise construction phase a fast structuration is positive for buildability. Finally, during hardening and curing, rheology is less important, but the mechanical properties of the material.

2.3 Requirements in concrete extrusion

2.3.1 Overview of pumping and material requirements for pumpability

In general, pumping is a low price, fast, continuous and flexible method to convey material evenly to any place. It has particular advantages in cramped building sites or when access to the location is poor. The pressure difference between inlet and outlet cross section of the pump unit creates and maintains a continuous flow of the material. The pump pressure should be limited: on one hand it must be small enough not to lead to segregation of the material and on the other hand it must be larger than the sum of all resistances in the pipe, thus compensating the pressure loss due to friction, bending and vertical height (Hermann, 1974).

The pumpability of a material depends on the pumping system used, e.g., technology, pumping distance and height as well as the hose diameter. However, the interdependencies and physical phenomena in concrete are similar for different pumping systems. Pumpability is not an actual concrete feature (Kaplan et al., 2005), but a complex concept to classify the ability of concrete to be conveyed in a pump. The assessment of pumpability is based on different approaches involving direct pumping tests and rheological investigations and aims for the optimization of the concrete composition as well as pumping parameters (Feys, 2009; Mechtcherine et al., 2014; Abebe, 2017; Secrieru, 2018).

One possibility to evaluate pumpability is the comparison of mixtures by pressure over flow rate during pumping (Kaplan et al., 2005). The smaller the slope of the curve, the better is its pumpability. Furthermore, a test setup called Sliper (Sliding Pipe Rheometer by Schleibinger Geräte GmbH) can provide results which classify the pumpability of the material, see e.g. Kasten (2010). In order to estimate the pumpability, tribumeters are also used, see e.g. Feys et al. (2016b).

A material is pumped more easily than another one if it needs less pressure to be pumped at a constant flow rate. In a simplified manner, the material has to be flowable enough and not too sticky (Feys et al., 2013; Secrieru et al., 2017). For the pumping of concrete, it has been shown that the material must not necessarily be completely flowable. It is sufficient if the material is able to build a so called lubrication layer to be pumpable. The existence of this lubrication layer and its relevance for pumpability have been intensively discussed by, e.g., Tattersall and Banfill (1983); Kaplan (2001); Haist and Müller (2005); Kaplan et al. (2005); Jacobsen et al. (2008); Choi et al. (2013); Secrieru (2018).

The formation of the lubrication layer is related to hydrodynamic effects, especially to flow-induced particle migration (Fataei et al., 2021). Due to shear localization in a small zone at the interface of the pipe walls, particle migration takes place. This could be described as dynamic segregation (Thrane et al., 2007). Apparently, coarse particles move towards the center of the pipe and form a so called plug zone where the material is unsheared. The fine particles and the water stay close to the wall surface building a lubrication layer which is exposed to shear, see Figure 2.4. According to Feys et al. (2010), the magnitude of the plug flow zone depend on the yield stress. For high yield stresses, only the lubrication layer is sheared.

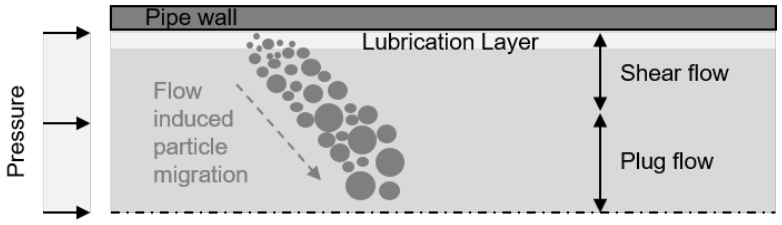

FIGURE 2.4: Lubrication layer in a hose based on (Secrieru, 2018)

As soon as a lubrication layer forms, the rheology of the bulk is less decisive for pumpability (Kaplan et al., 2005; Choi et al., 2013). Still, the characteristics, especially the rheology, of the material before pumping influence the ability to form a lubrication layer. The lubrication layer is similar to the associated mortar of the pumped concrete (Choi et al., 2013), but might vary in maximum aggregate size.

After formation of the lubrication layer, an equilibrium evolves. This happens the latest when the maximum packing density in the plug flow zone is reached. As a consequence, the thickness of the layer as well as its rheological properties stay constant (Browne and Bamforth, 1977; Kaplan et al., 2005; Secrieru, 2018). The thickness of the lubrication layer depends more on the composition of the pumped material than on the pumping speed and might be a few mm to 10 mm thick (Choi et al., 2013). Furthermore it depends on the roughness of the pipe wall—decreasing in thickness when the friction at the wall increases.

In order to form a lubrication layer, the paste volume of the mixture must be high enough. Secrieru et al. (2018) conducted filtration tests in order to determine the ability of a material to built a lubrication layer. They applied a force on the material and measured the amount of filtrated water over time. The amount of filtrate depends on the specific surface of the fines and on the plastic viscosity of the material (Secrieru, 2018). Lower plastic viscosity leads to a higher filtrate amount. According to Secrieru (2018), the amount of filtrate and its rate of formation

determine to a great extent the formation of a lubrication layer as it indicates the free water in the system. It should be noted, that the amount of filtrate does not only depend on the specific surface which is possible to determine with Blaine measurements, but also on the water demand, which is influenced by the particle shape (Secrieru, 2018). Furthermore, the relationship only holds if the mixture itself is stable. Moreover, some admixtures, e.g. superplastizisers, have an effect on the filtration amount as they affect the rheologically effective water and the adhesively bound water (Sakai et al., 2006).

The lubrication layer reduces the friction between pipe wall and coarse aggregates as well as between the coarse aggregates themselves. The thickness of the lubrication layer depends on the pipe diameter and might be thinner with increasing pipe diameter (Secrieru, 2018). The size of the system, i.e., the conveying length and the diameter, must match the rheology of the material. The yield stress at the nozzle, for example, is affected by the residence time (the time a material spends in the delivery system) (Reiter et al., 2018). If the residence time is too long, the risk for blockage increases. If the residence time is too short, the structural build-up in the hose might not be enough for the material to sustain its own weight after deposition (see Section 2.3.2). The distribution of the residence time can be different over the cross-section of a pipe as shown in Reiter et al. (2018) leading to partial clogging.

If the flow conditions are not laminar, e.g., in screws or in contracting zones, the shear does not localize as described and shown in Figure 2.4 and it can be expected that the whole material is sheared. This can also be the case in tapered nozzle geometries (Roussel, 2018). The type of flow in the hose depends on the pump and hose characteristics as well as the rheology of the material (Feys et al., 2015). The pumping pressure without plug flow is mainly related to the viscosity of the pumped material.

Roussel (2018) suggests that the influence of the yield stress can mainly be neglected for 3D-printable materials with regard to pumpability. This is supported by Wallevik and Wallevik (2011) who state, that pumpability depends more on the plastic viscosity μ and less on the yield stress τ_0. A reduction in yield stress only decreases the initial force to start the movement. However, such a change does not necessarily improve the pumpability of the concrete (Secrieru, 2018). Thus, the previously used slump or flow table values in order to predict pumpability are not applicable to all types of concrete and viscosity is more appropriate to describe the flow resistance (Secrieru et al., 2017).

Browne and Bamforth (1977) differentiate between "unsaturated" mixtures, which have an insufficient cement paste content leads to friction between the aggregates, and "saturated" mixtures, where direct contact of the aggregates is avoided. They prove mathematically that higher pressures are required in order to pump unsaturated mixtures.

The beginning of pumping poses a major challenge as the friction between dry pipe walls and the material is high. Providing an initial lubrication layer by pre-wetting the pipe or hose with water or a primer helps to convey the material more easily (Liu et al., 2017). Primers are often polymer-based and replace cement grout which was used conventionally to prepare the pipes for pumping. Primers don't mix as much with the concrete and thus less material has to be disposed.

Concerning the material composition, major effects on pumpability are listed in literature like water content, grain size distribution, shape of aggregates and admixtures. The water content of the mixture significantly influences the plastic viscosity of the material and influences the formation of a lubrication layer. Materials with a low water-content tend to have high yield stress, high plastic viscosity and little ability to form a lubrication layer and therefore require high pumping pressures. Another important parameter affecting pumpability is the grain size distribution of the mixture. Grading curves according to EN 206:2017-01 between reference curve A and B are recommended (Secrieru, 2018). Higher contents of fine materials influence the formation of a lubrication layer positively (Secrieru, 2018) and lower the plastic viscosity. However, if the content of fine particles in fully saturated concretes is too high, the flow resistance of the concrete might increase significantly resulting in worse pumpability (Browne and Bamforth, 1977). This can be traced back to the high surface area of the particles which reduces the movable water for the formation of the lubrication layer and might be critical if no superplasticizer is added. For a similar reason, round aggregates favor pumpability compared to crushed aggregates due to the higher surface area of the latter (Secrieru et al., 2017). Furthermore, rounded aggregates decrease the plastic viscosity while crushed aggregates increase it. The amount of silica fume and superplasticizer content also significantly influence pumpability. Silica fume has ultra-fine spherical particles and might thus initiate a "ball-bearing effect" reducing the friction between cement particles. The prerequisite is an even distribution of the grain size. Replacing the cement in a moderate quantity, the silica fume reduces the plastic viscosity (Vikan and Justnes, 2003). Choi et al. (2015) find an enhancement in pumpability when replacing 5 % of the cement by mass. Increasing the silica fume further leads to an increase in yield stress and plastic viscosity

and to an impairment of pumpability (higher pressure at equal flow rate) (Choi et al., 2015; Secrieru, 2018). Furthermore, silica fume influences the structural build-up and setting of the fresh concrete (Neroth and Vollenschaar, 2011). Thus, the time for which the material is pumpable, might be shortened.

Using superplasticizers reduces the flocculation by dispersing the particles (e.g., by steric hindrance) and lowers the surface tension of the water. Thus, otherwise "trapped" water is more effective for flowability or the formation of a lubrication layer. However, potential destabilization of the mixture must be taken into account. If superplastizisers are used, the combination with other additives must always be considered (Jeong et al., 2016). Using air-entraining agents might also affect pumpability as the loss of air is compensated (Jacobsen et al., 2008; Vosahlik et al., 2018).

The shear rate during pumping lies in the range of 1-100 s^{-1} (Kaplan, 2001). For pumping of mortar in a progressive cavity pump the shear rate is supposed to be approximately 20-30 s^{-1} (Kaplan, 2001; Roussel, 2006). High shear rates cause the particles to disperse and thus increases flowability of the material. While low shear allows for the material to flocculate and build structure (Wallevik and Wallevik, 2017).

Concrete may change its characteristics during pumping. Feys et al. (2016a) find that the viscosity decreases with increasing pumping time and flow rate for self-compacting concrete and attribute this to shearing of the concrete during the pumping process leading to dispersion of the cement particles. They identify the water to binder ratio and the paste volume to have a major effect on the changes in viscosity (Feys et al., 2016a). They also find an increase in compressive strength. No uniform trend for yield stress was reported (Feys et al., 2016a). Takahashi and Bier (2014) state that the shearing and mixing in the pump has a considerable influence on the rheological properties of the concrete. For longer shearing and mixing they report a decrease in yield stress, an increase in viscosity, and an increase in early strength. Furthermore, the content of air might vary and smaller air bubbles might coalesce during pumping (Aitcin and Flatt, 2015). The rheological properties and their evolution during pumping carry through to the final product as they also change the hardened concrete properties such as mechanical performance, durability and sustainability (Aitcin and Flatt, 2015).

2.3.2 Material requirements for buildability

Strength and failure types

In general, the strength development of the concrete determines the possible printing speed, probability of failures and application areas. The strength is important both in fresh and hardened state. The following three aspects must be taken into account:

1. The development of strength of fresh concrete to bear loads during the building process and restrict deformations (buildability);
2. The strength of layer bond to avoid delamination and predetermined breaking points;
3. The strength of hardened concrete to bear external loads applied on the building component.

During extrusion, the strength determines the feasibility and, with regard to deformations and shape accuracy, the quality of the final object. At the same time, the evolution in strength must be limited in order to ensure a good bond between the individual layers, see Section 2.3.3. Finally, the strength development as well as the layer bond determine the hardened concrete properties and consequently define possible use cases for a built structure. This last aspect is not the focus of the thesis and will only be discussed as an aside.

The so-called **buildability** describes the ability of a layer to bear its own weight and the load induced by subsequent layers without significant deformation or failure during the manufacturing process. Along with pumpability, it is the most important factor to ensure extrudability. After the material has been extruded through the nozzle and before setting (phases 2 and 3, cf. Figure 2.1), the immediate load-bearing capacity (green strength) of a deposited layer and its increase over time are of essential importance for the extrusion process.

The building rate, which defines how fast a component can be manufactured, depends strongly on the development of the green strength and thus, on the rheological properties of the material. The green strength is predominantly determined by the yield stress of the material. At deposition, the yield stress is decisive. If the yield stress is too low, the material deforms, implying bad contour accuracy or even failure of the printed element. If the yield stress is too high, the layers do not bond sufficiently and so-called layering occurs (see layer bonding in Section 2.3.3). The time-window for structuration between layers is process and object-length-scale dependent (Wangler et al., 2016). The shorter the layer cycle time, the higher the necessary increase in yield

stress. In order to ensure an increase in yield stress, thixotropy enhancing agents are favorable as well as the application of accelerators. The effect on pumpability must always be kept in mind. In order to separate the material properties in the different phases, admixtures might also be added at the nozzle (Reiter et al., 2018).

The main requirements for buildability on the layers are as follows: Firstly, the layers must be self-supporting upon placing. Thus, a small slump flow is desired which corresponds to a low flowability of the material. Secondly, they must support the weight of subsequent layers.

With regard to failure during the building process, mainly two mechanisms are described in literature: Buckling failure and plastic failure (see Figure 2.5). The buckling failure describes a stability failure and depends strongly on the Young's modulus of the material and the geometry of the printed object (Suiker, 2018; Wolfs et al., 2018; Wolfs and Suiker, 2019). It corresponds to the wall tipping-over or bulging.

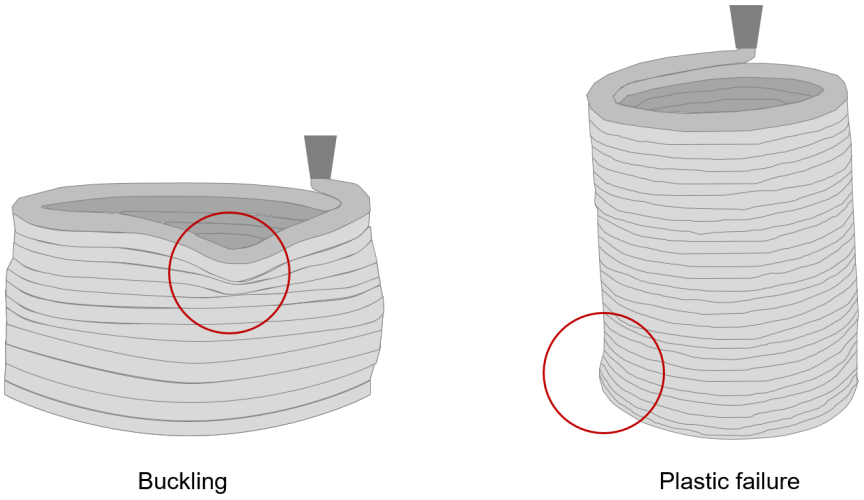

FIGURE 2.5: Failure types during the building process – beginning of buckling and plastic failure

The plastic failure is a material failure and occurs usually in the lowest or second-lowest layer if the stress applied by subsequent layers exceeds the critical stress in these layers (Roussel, 2018). It corresponds to a deformation of the layer and a slump-down of the element. According to Suiker et al. (2020), the probability for the plastic collapse in the second-lowest layer is higher than in the lowest layer. This is due to the bearing conditions and ground friction for which the bottom layer is constrained and limited in plastic deformation while the second layer is not.

Structuration

Calculation models for buildability are based on the most relevant rheological properties of the material as presented in Section 2.2. The shear stress $\tau(t)$ of fresh concrete increases with time

at rest starting from the static yield stress $\tau(0) = \tau_{0,S}$. In addition, the elastic shear modulus increases with time at rest (Wolfs et al., 2018). As a consequence, the material becomes stronger and more rigid during the 3D-printing process. The structuration rate A_{thix} (increase in static yield stress with time) is assumed to be constant (Roussel, 2006; Roussel et al., 2012; Roussel, 2018) and the shear stress thus develops linearly with time

$$\tau(t) = \tau_{0,S} + A_{thix} \cdot t.$$

This increase is due to fluccolation and early hydration processes in the dormant period of the concrete (Roussel et al., 2012). The linear development is in contrast to other literature, which state that the static yield stress of the material develops exponentially with time (e.g., Mettler et al., 2016). These results usually consider larger periods of time and are thus more influenced by the hydration process itself. During the first 3 hours of hydration the structuration develops exponentially.

Normal weight concrete which is optimized for 3D-printing can—already after a few minutes—reach a static yield stress exceeding the measurement capacities of standard rheometers. The requirements on yield stress for normal weight concrete in extrusion lie between approx. 150 Pa for a single layer to approx. 100,000 Pa for a construction element (Wangler et al., 2016; Roussel, 2018).

Thus, the measurement range must be suitable for this application. Preferably, the yield stress should be processed and measured in-line providing a direct feedback during the process. However, the in-line measurement still represents a great need of research. In order to evaluate the static yield stress and its evolution over time different methods can be found:

1. Rheological measurements with a vane-in-cup measuring device can be used to evaluate the increase in yield stress over time. For static yield stress measurements, single measurements at individual time spots or multiple discontinuous measurements are possible (see, e.g. Billberg (2003)). However, this technique might not be suitable for every type of concrete or mortar due to shear localization and fracturing at stiff materials. Note that, due to the use of different mathematical models, the results can only be compared if the same measuring device and evaluation method is used.

2. Alternatively, uniaxial unconfined compression tests, where a cylindrical test specimen is directly loaded with a force, can be conducted (Kränkel et al., 2010; Perrot et al., 2016;

Wolfs et al., 2018). This method can be conducted prior to printing tests to simulate the load of subsequent layers. Preferably cylinders with a height corresponding to 2 times the diameter are used to avoid transfer expansion hindrance. The estimation is made by evaluating the peaks in the load-deformation diagram followed by a conversion to stress and strain. Multiple samples must be prepared and tested at different material age. Note that the susceptibility to the influence of human error is relatively high, e.g., when removing the formwork or placing the cylinders in the test apparatus.

3. Mettler et al. (2016), Reiter et al. (2018), and Reiter (2019) propose to conduct penetration tests with a sufficiently large needle. This method allows to quantitatively relate the penetration force to the yield stress of stiff materials. The method has a measuring range of 1,000-200,000 Pa (Reiter, 2019) and is usually conducted process-parallel on the extruded material. Furthermore, Pott and Stephan (2021) describe a method to perform continuous penetration tests. However, the comparison to conventional yield stress determination still needs to be validated with a larger number of tests.

4. Calorimetric measurements allow to qualitatively compare different materials with regard to their structuration. The rate of hydration can be monitored. However, this method is of limited interest for extrusion as the most challenging part with regard to the material requirements occurs before hydration.

5. Ultrasound measurements to evaluate an approximated strength evolution on basis of the change of the dynamic Young's modulus is also possible. Calibration is needed in order to compare the values to absolute values of strength. However, this method is not yet suitable to determine early structuration.

6. The so-called slug test (Ducoulombier et al., 2020) is a gravity driven test recently developed specifically for extrusion. The length of the extruded material strand before tearing-off is evaluated and converted to an equivalent yield stress. However, this test can only be carried out during extrusion and does not allow the yield stress to be estimated in advance.

Plastic failure

According to Roussel (2018), the gravity-induced stress in a deposited layer, which is due to its dead weight and approximated by hydrostatic pressure, is dominantly shear stress and in the order of $\sigma_v = \rho g h_i$ due to the flat shape of the layers, with density ρ, layer height h_i and gravity constant g. This is supported by the investigations of Wangler et al. (2016). Based

on Schowalter and Christensen (1998), Wangler et al. (2016) introduce an additional geometry constant $\alpha_{geom} = \sqrt{3}$ considering the wall-like shape of the 3D-printed object resulting in a shear stress of $\sigma_v = \rho g h_i / \alpha_{geom}$.

The gravity induced-stress on the deposited layers increases with increasing amount of layers reaching its maximum at the final height of the object H_t. Thus, the worst case in terms of loads occurs in the bottom layer when the final height of the 3D-printed object H_t is reached. For walls the geometry is usually slender comparing its height, width, and length. This slender geometry of the final object results in dominantly extensional stresses in the bottom layer in the range of $\sigma_{v,t} = \rho g H_t / \alpha_{geom}$ (Perrot et al., 2016; Wangler et al., 2016). Thus, the ratio between initial and final static yield stress correlates to H_t / h_i (Wangler et al., 2016).

In most cases, failure is due to the static yield stress not being able to support the gravity-induced stress, while influence of inertia stress and surface tension can be neglected. The vertical stress resulting from the subsequently deposited layers increases step by step with the deposition of each layer. The stepwise increase of induced stress due to the subsequently deposited layers can be simplified by a linear approximation of the same on the safe site, see Figure 2.6. An average wall growth rate $\dot{s}$ can be calculated using a constant building rate and thus, an constant increase in height over time. The parameter $\dot{s}$ is dependent on the nozzle velocity v, the contour length l and the layer thickness h_i, with $\dot{s} = v h_i / l$.

As constant building rates are targeted in extrusion processes, the static yield stress of any layer should increase at least according to the weight of subsequent layers to enable continuous production without deformation (Reiter et al., 2018). The lowest layer must have sufficient yield stress in combination with structural build-up to bear its own weight and the weight of subsequent layers (approximated by hydrostatic pressure). Thus, the static yield stress needs to develop at least linearly over time to bear the linearly increasing load of the additional layers. The induced vertical stress σ_v can be described in a simplified way assuming constant building rate by

$$\sigma_v = \frac{\rho g \dot{s} \cdot t}{\alpha_{geom}}. \tag{2.1}$$

To avoid plastic failure the critical green strength σ_c in the lowest layer must be larger than the vertically induced stress $\sigma_c > \sigma_v$. The critical stress corresponds to the static yield stress. For a linear approximation of the static yield stress evolution, the requirement can be rewritten as

$$\tau_{0,S} + A_{thix} \cdot t \geq \frac{\rho g \dot{s} \cdot t}{\alpha_{geom}}. \tag{2.2}$$

Figure 2.6 depicts the green strength over time in the lowest layer (σ_c). Furthermore, it shows the stepwise increase of induced stress due to the subsequently deposited layers ($\sigma_{v,real}$) and the simplified linear approximation of the same on the safe side (σ_v). Plastic failure occurs at the intersection of the lines.

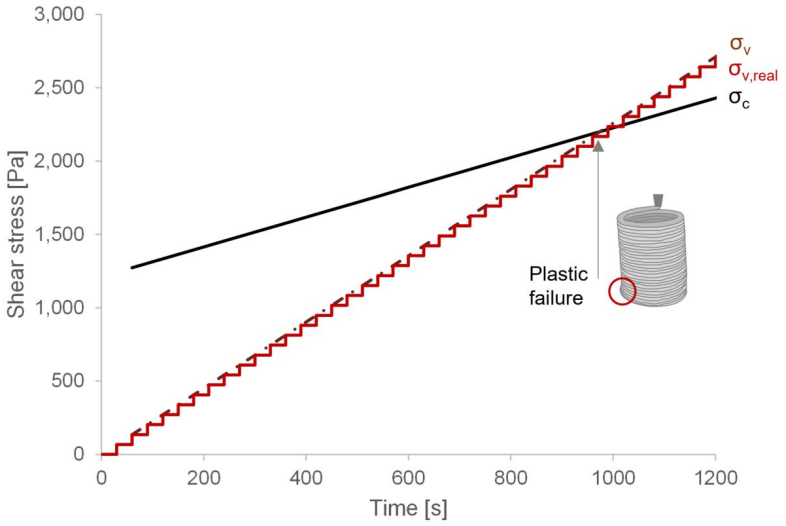

FIGURE 2.6: Plastic failure at the intersection of critical green strength σ_c in the bottom layer and induced stress σ_v

For materials with an initial yield stress, the critical failure time for plastic failure t_p is

$$t_p = \frac{t_{0,S}}{\rho g \dot{s}/\alpha_{geom} - A_{thix}} \tag{2.3}$$

assuming linear evolution of the static yield stress (Roussel, 2018).

However, Lecompte and Perrot (2017) and Perrot et al. (2016) state that the evolution of the yield stress is not linear over time before setting. Lecompte and Perrot (2017) developed a non-linear model for the increase of yield stress due to structural build-up in self compacting concrete. They state, that the structural build-up is almost linear in the first tens of minutes, but consequently increases non-linearly. They develop a model accounting for the growth of the cement grains and obtain good results in their validation for additive manufacturing. Perrot et al. (2016) uses the following exponential model for the calculation of the static yield stress over time:

$$\tau(t) = \tau_{0,S} + A_{thix} \cdot t_c \cdot \left(e^{\frac{t_{rest}}{t_c}} - 1 \right), \tag{2.4}$$

where t_{rest} describes the time at rest and t_c is a factor which is adjusted for an optimal fit of the model and the experimental values. t_c needs to be calibrated with failure tests prior to printing

(Perrot et al., 2016). Assuming that at the time of plastic failure t_p the vertical stress is equal to the critical stress $\sigma_v = \sigma_c = \tau(t)$ and the material is at rest for the whole time $t_{rest} = t_p$, the factor t_c can be calculated by solving

$$t_c \cdot e^{\frac{t_{rest}}{t_c}} - t_c = \frac{\sigma_v/\alpha_{geom} - \tau_{0,S}}{A_{thix}}. \tag{2.5}$$

In their model, Perrot et al. (2016) neglect the dead weight of the first deposited layer. To validate their model, Perrot et al. (2016) perform uniaxial compression tests: they place fresh concrete between two parallel plates and increase the load in 1.5 N increments in fixed time increments to simulate the layer by layer construction. The time increments in different tests correspond to building rates ranging from 1.1 to 6 $\frac{m}{h}$. Furthermore, they conduct oscillatory measurements to determine the static yield stress at flow onset (see Section 2.2). They assume that sample failure is reached when both, fracture onset at the surface and increase in displacement rate occur. They show that the slower the building rate, the later plastic failure occurs. Perrot et al. (2016) state that for time exposure longer than 25 minutes, the exponential model describes the evolution of yield stress over time more accurately than the linear model of Roussel (2006). Furthermore, they note that the critical failure time t_p (see equation 2.3) is only valid for $t_p < t_c$. If t_p is in the order of the setting time of the concrete, the structure remains stable and no failure occurs in terms of plastic failure of the lowest layer (Perrot et al., 2016).

The exponential function could also be fitted to the measured values to reduce the effort of performing actual failures. For the fitting to the measured values by a least error square approach two fitting variables e_1 and e_2 are used. In order to avoid plastic failure, the requirement in equation (2.6) must be fulfilled.

$$\tau_{exp}(t) = \tau_0 + e_1 \cdot e^{e_2 \cdot t} \geq \frac{\rho g \dot{s} \cdot t}{\alpha_{geom}}. \tag{2.6}$$

The failure time can not be solved analytically, but e.g., graphically.

Kruger et al. (2019b) develop a bi-linear model for the evolution of yield stress over time. The varying slopes account for the re-flocculation (R_{thix}) and the structuration (A_{thix}) mechanisms. In this way, they try to describe as accurately as possible the condition of the material immediately after it has been deposited, also taking into account its shear history. The bi-linear model consists of the two equations (2.7) and (2.8). Depending on the time t_r in which re-flocculation

occurs with $t_r = \frac{\tau_{i,S} - \tau_{0,S}}{R_{thix}}$, either equation (2.7) or equation (2.8) is used:

$$\tau(t) = \tau_{0,S} + R_{thix} \cdot t \text{ for } [t \leq t_r], \tag{2.7}$$

$$\tau(t) = \tau_{i,S} + A_{thix} \cdot (t - t_r) \text{ for } [t > t_r]. \tag{2.8}$$

Since failure relevant to lightweight aggregate concrete extrusion normally occurs after a time greater than the re-flocculation time, the following equation (2.9) can be drawn up based on Kruger's equation (2.8):

$$\tau(t) = \tau_{0,S} + R_{thix} \cdot t_r + A_{thix} \cdot (t - t_r) \geq \frac{\rho g \dot{s} \cdot t}{\alpha_{geom}}. \tag{2.9}$$

Thus, the plastic failure time is

$$t_p = \frac{\tau_{0,S} + R_{thix} \cdot t_r - A_{thix} \cdot t_r}{\rho g \dot{s} / \alpha_{geom} - A_{thix}} \text{ for } [t > t_r]. \tag{2.10}$$

Based on the failure time, the amount of layers at failure $a_f = \frac{t_p \cdot \dot{s}}{h_i}$ as well as the predicted failure height $H_f = a_f \cdot h_i = t_p \cdot \dot{s}$ can be calculated. Furthermore, in order to extrude an object with a given total height H_t without failure, the minimum time allowed per layer is interesting in order to set the print parameters suitably. For this purpose the minimum object realization time t_m is determined. For the linear approach, it is

$$t_{m,lin} = \frac{(\rho_f \cdot g \cdot H_t / \alpha_{geom}) - \tau_{S,0}}{A_{thix}}$$

and for the bi-linear approach

$$t_{m,bl} = \frac{(\rho_f \cdot g \cdot H_t / \alpha_{geom}) - \tau_{S,0} - R_{thix} \cdot t_r + A_{thix} \cdot t_r}{A_{thix}} \text{ for } [t > t_r].$$

On basis of these values, the minimum time per layer

$$\dot{l}_i = \frac{t_m}{a_t} \tag{2.11}$$

is determined which is an indicator for the possible construction speed without failure at a total number of layers $a_t = \frac{H_t}{h_i}$.

In addition, there are further models, e.g. by Wolfs et al. (2018); Kruger et al. (2020), based on the Mohr-Coulomb approach predicting failure similarly as for soils. The model of Wolfs et al. (2018) is based on compression and shear tests and is closely related to their studies on buckling failure during extrusion. They differentiate in plastic collapse due to compression failure and due to pressure-dependent shear failure. The input parameters are internal friction ϕ and Cohesion $C(t)$ of the material, the so-called shear parameters (also called Mohr-Coulomb parameters). Due to the similarity of the deformation behavior of stiff concretes to that of soils, the Mohr-Coulomb yield stress is proposed as a means to describe the time-dependent evolution of the material properties in the buckling failure evaluation. For compression failure, the yield stress is equal to the uniaxial compressive strength in accordance with the maximal stress theory (Suiker et al., 2020). The predicted height for a plastic collapse $H_{f,p}$ is calculated on basis of the results of compression tests (see Section 3.7.3). The approach is almost the same as for the linear approach, but does not include the geometrical factor α_{geom}:

$$H_{f,p} = \frac{\tau_0}{\rho g - \frac{\tau_0}{\dot{s}} \cdot \xi_\sigma} = \frac{\tau_0}{\rho g - \frac{A_{thix}}{\dot{s}}}, \tag{2.12}$$

Summarizing, the vertical stress depends on the building rate (see equation 2.1) while the critical stress of the lowest layer or second lowest layer respectively depends on the structural build-up. According to literature, this is usually approximated either linearly, bi-linearly or exponentially. In total, the building rates aimed for, depend on the structural build-up of the material.

Buckling failure

The failure mode buckling is understood to be the stability failure of thin-walled structures with a centrally applied compressive load or shear load in their plane that is greater than the critical resistance of the material. Those geometries tend to evade higher loads prematurely by moving sideways. This deflection often occurs suddenly, without clear notice, and can occur well before the material reaches its current maximum green strength, reducing its load-bearing capacity. The loss of the stable equilibrium, due to compressive or shear loading, results in deformations perpendicular to the plane (Suiker, 2018).

Roussel (2018) presents a model for buckling of objects with rectangular cross-sections. Self-buckling due to the dead weight of the material happens at a critical height $H_{cr} = (\frac{8EI}{\rho g A})^{\frac{1}{3}}$ with Young's modulus E, quadratic moment of inertia I and cross-section area A. For a wall with width δ, this can be simplified to $H_{cr} = (\frac{2E\delta^2}{3\rho g})^{\frac{1}{3}}$ and the critical Young's modulus for an object of total height H_t can be written as $E_c \geq 3\rho g H_t^3 / 2\delta^2$ (Roussel, 2018). This approach based on the

Young's modulus allows for a rough estimation—underestimating the printable layers. However, it does not include time-dependent and geometry-dependent effects. According to the approach, the material requirements to avoid buckling scale with the power of 3 in the height whereas the material requirements for plastic failure scale linearly with the height of the object. Thus, under a certain transition height $H_T = 2\delta\sqrt{\frac{1+\nu}{3\sqrt{3}\gamma}}$ with Poisson coefficient $\nu \approx 0.3$, the probability for plastic failure is higher while above this critical value, buckling is the major reason for failure (Roussel, 2018).

The higher the slenderness of an object, the higher the required Young's modulus (Reiter et al., 2018). Thus, the larger the width of an object, the lower the probability for buckling failure. As a consequence, the larger the width of the object, the longer plastic failure is the critical failure mechanism.

Suiker (2018) develops a parametric model on basis of the Mohr-Coulomb material failure criterion in order to evaluate the strength and stability of a wall-type structure for varying process parameters (e.g., printing velocity) as well as material properties (e.g., curing rate and geometric parameters). Suiker et al. (2020) conduct experiments to validate this approach and find that the main (dimensionless) parameters to analyze buckling are

$$H_{cr}^{*} = \left(\frac{\rho g \delta}{D_0}\right)^{1/3} \cdot H_{cr} \text{ and} \tag{2.13}$$

$$\xi_E^{*} = \left(\frac{D_0}{\rho g \delta}\right)^{\frac{1}{3}} \cdot \frac{\xi_E}{\dot{s}}, \tag{2.14}$$

with initial Young's modulus E_0, density of the material ρ, thickness of the wall δ, critical height of the wall H_{cr}, Poisson coefficient ν, setting rate ξ_E, wall growth velocity $\dot{s}$ and initial bending stiffness D_0

$$D_0 = \frac{E_0 \cdot \delta^3}{12 \cdot (1-\nu^2)}. \tag{2.15}$$

To calculate the predicted buckling height $H_{f,b}$, the equation (2.13) is converted and H_{cr} is approximated by $H_{cr} = 1.986 + 0.996 \cdot (\xi_E^{*})^{0.793}$ according to Suiker et al. (2020) resulting in equation (2.16)

$$H_{f,b} = \frac{1.986 + 0.996 \cdot (\xi_E^{*})^{0.793}}{\left(\frac{\rho g \delta}{D_0}\right)^{\frac{1}{3}}}. \tag{2.16}$$

Thus, the buckling failure depends on the geometry and on the process parameters. These include: component height, component thickness which is dependent on the layer width, the component or layer length and the support conditions. Furthermore, the deposition velocity, layer height, number of layers and nozzle geometry have an effect on the buckling tendency. Martínez-Rocamora et al. (2020) were able to show that due to the higher resistance to overturning forces of curved walls the material consumption could be reduced by 61 % and the estimated costs by 53 %.

Summarizing, the buckling failure depends strongly on the geometry of the 3D-printed object. Increasing the width, the probability for buckling failure decreases. Furthermore, a high quadratic moment of inertia is favorable. Applying inner structures of the element where the individual strands are connected to each other, a high width at low required material volume can be reached. This is beneficial from an thermal and structural point of view and reduces the material requirements due to buckling (Roussel, 2018). Furthermore, structural and morphological effects can reinforce the printed object against buckling (Roussel, 2018).

2.3.3 Layer bonding

During concrete extrusion, each layer is in a different condition as resting time and curing (i.e., hydration and related setting and hardening) progress vary. For a good strength development of the overall structure, it is important that individual layers are well connected to each other. If the bond is poor and so called cold joints occur, anisotropic material properties arise. High structuration rates as well as long cycle times or pauses can result in weak layer interfaces, also called cold joints (Roussel, 2006; Zareiyan and Khoshnevis, 2017a). If the strength between the layers is lower than in the layers and thus becomes a weak point of the 3D-printed object, the strength of the object varies direction-dependently (Bos et al., 2016).

In general, to achieve a good bond between the layers, the physical-chemical reactions during hydration should take place across the layer boundary. For this purpose, hydration in the lower layer must not be advanced when the next layer is placed. In addition, the water content at the layer boundary and the presence of larger air voids also have an effect. In order for subsequently deposited strands to have a good bond, an upper limit for the static yield stress and the structuration rate is required. The upper limit for layer cycle time $\dot{l}_{i,max}$ according to

Roussel (2018) depends on the structuration rate A_{thix} and is given as

$$\dot{l}_{i,max} = \frac{\sqrt{\frac{(\rho g h_i)^2}{12} + \left(\frac{2\mu v}{h_i}\right)^2}}{A_{thix}} \tag{2.17}$$

with plastic viscosity μ and velocity of the print head v.

The actual evolution of yield stress also depends on process and external parameters, e.g., time between mixing and printing, temperature change, printing speed, and material flow rate. According to Wangler et al. (2016), neglecting the initial yield stress, the minimum velocity of the print head must be $v > \frac{\rho g h_i^2}{4\mu}$.

Another factor for weak layer bonding might be superficial drying of the resting layer. Keita et al. (2019) vary the waiting time between the deposition of layers and, in one case, protected the strands from drying while, in the other case, left them unprotected. In splitting tensile strength, they documented a strong decrease due to drying for the normal specimen while the specimens that were protected from drying did not show a significant reduction at waiting times of 2 h. This drying phenomenon might be even stronger when using accelerators due to the associated temperature increase. Concluding, in addition to the material properties, layer bonding seems to be dependent on the printing environment (e.g., temperature and humidity). Concerning the ambient conditions, increasing temperature has to be taken into account as it leads to earlier setting of the concrete (Springenschmid, 2018) which significantly influences the evolution of the yield stress over time. Evidence for the effect on layer bond, particularly for different types of materials, is still needed.

In addition to the physical-chemical layer bond, the mechanical interlocking of the layers also represents a possibility to improve the layer bonding (Zareiyan and Khoshnevis, 2017a), e.g., by applying tongue and groove systems or reinforcement perpendicular to the layers.

2.3.4 Hardened concrete properties

The hardened concrete properties are on one hand affected by the strength of the material itself as in conventional construction. On the other hand, the quality of layer bonding plays a significant role for the hardened concrete properties of a completed 3D-printed construction element. Roussel and Cussigh (2008) report that cold joints can severely affect the mechanical cohesion between the layers for self-compacting concrete. Long waiting time leads to deterioration of the

mechanical properties. This interrelation between process parameters and mechanical characteristics is also reported by other authors in the field (Le et al., 2012b; Feng et al., 2015; Panda et al., 2017; Zareiyan and Khoshnevis, 2017a,b; Panda et al., 2018). The effect of the layer bonding on the hardened concrete properties might be material dependent. Especially, high acceleration or a strong structural build-up affect the bond between the layer negatively when the process parameters are not adapted considerably.

As for conventional concrete, the strength of the material itself is affected by the water-cement-ratio ($\frac{w}{c}$-ratio)—influencing the porosity by the formation of capillary pores—as well as by the cement type. Furthermore, the hardened concrete properties are influenced by process parameters. This is known for extruded concrete elements (e.g., Paul et al., 2018; Panda et al., 2019), but only very limited interdependencies with the printability requirements are established. Pumping might also influence the hardened concrete properties if the material properties, especially the density, change.

In terms of hardened concrete properties, the durability of the concrete is also relevant. The granulometry of the material has a significant influence on the tightness and thus on durability and strength of an element (Neroth and Vollenschaar, 2011). The questions of the physical nature of the cold joints and their effect on the durability still needs to be addressed.

2.3.5 Conflicting design goals

According to Perrot et al. (2016), concrete extrusion is confronted with two contradicting requirements concerning the fresh concrete. One contradicting requirement concerns the production rate. The layer cycle time and thus the waiting time between two layers must be sufficiently long for the underlying layer to develop adequate mechanical strength and short enough to ensure good layer bonding. For an optimization of the time gap, the shortest layer cycle time is crucial that still ensures stability of the object.

The second contradicting requirement appears directly at the deposition of the material and concerns the conflicting requirements for pumpability and buildability. Looking at the requirements for pumpability and buildability, they seem diametrically different. The material has to be flowable enough for pumpability and stiff enough for buildability. However, the requirements for pumpability are mainly affecting the viscosity of the material and only set an upper limit to yield stress while the requirements for buildability are mainly affecting the static yield stress and structural build-up of the material. There is also an upper limit to the yield stress resulting

from layer bonding to avoid so-called cold joints. The upper bound to avoid cold joints affects only a short time after the layers have been deposited, i.e. the time until the subsequent layer is deposited, so that the considered layer can bond with the next layer, see Figure 2.7. Thus, both, pumpability and layer bonding set an upper limit for the static yield stress.

The conflicting requirements might be counteracted by addition of admixtures. Marchon et al. (2018) provide an overview of the admixture types suitable for the individual phases of extrusion. Table 2.1 sums up the main results and assigns them to the listed categories.

TABLE 2.1
Admixtures for phases of extrusion

This table gives an overview on potential admixtures according to Marchon et al. (2018).

Phase	Desired properties	Admixture type
Pumping	Flowability and Stability	Superplasticizers, Viscosity modifying admixtures (VMA)
Deposition	Retain shape	VMA, Fibers, Entrained Air
Buildability	Retain shape, controlled open time	Retarders for controlled open time, Accelerators for rapid strength gain
Hardening, Curing	Controlled setting, no cracks	Saturated lightweight aggregates, Shrinkage-reducing admixtures

For an optimization of the material in this conflicting target frame, the focus lies on rapid structural build-up instead of a high initial yield stress. The evolution of the yield stress strongly depends on the material components. Thixotropy enhancing agents as well as viscosity-modifying admixtures are often used as the thixotropic build-up enhances the structuration in the first minutes (see Section 2.2). Furthermore, the thixotropic build-up can be reversed by pumping. Thus, the upper bound placed by the pumping requirements might be modified. An alternative is a phase change at the nozzle introduced, e.g., by addition of accelerators.

In order to clarify the requirements in the first contradicting aspect, the bottom layer of a 3D-printed object is considered. The bottom layer is subject to a variety of requirements in terms of its yield stress. Right after deposition until finalizing the second layer, it has an upper bound due to layer bonding and a lower bound due to deformation limitation. Furthermore, over time, the lower bound increases to avoid plastic failure and buckling while the upper bound becomes negligible, see Figure 2.7. To guarantee good extrusion results, an optimal evolution of yield stress must be found between the upper and lower bounds (marked areas in Figure 2.7) over time since placing. The same requirement applies for every layer after its deposition independent of the material age.

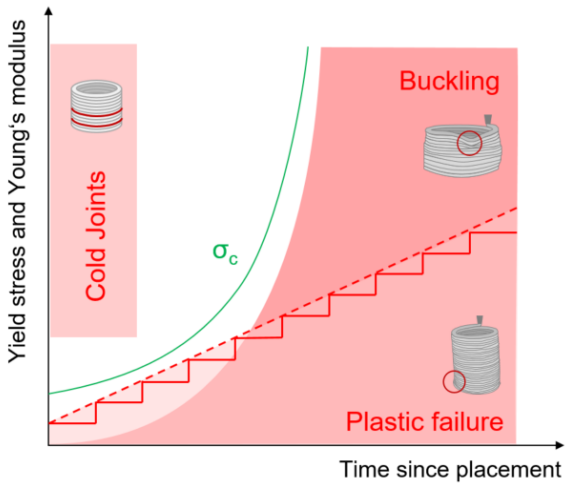

FIGURE 2.7: Requirements on yield stress and Young's modulus for extrusion (red areas) as well as optimal range of yield stress and Young's modulus for each layer (green line) following Reiter et al. (2018)

2.4 Lightweight concrete

2.4.1 Classification of lightweight concrete

Concrete is categorized in dependence of its density into heavy-weight concrete, normal weight concrete, and lightweight concrete. According to EN 206:2017-01 lightweight concrete has a dry density between 800 $\frac{kg}{m^3}$ and 2000 $\frac{kg}{m^3}$. Due to the low density, the thermal conductivity is significantly reduced compared to normal weight concrete.

The low density can be achieved by producing the porosity in different ways (Wesche, 1993; Faust, 2003; Thienel, 2018):

1. Grain porosity: the closed structure of the normal weight concrete is retained and the dense normal aggregates are replaced by porous lightweight aggregates, e.g., structural lightweight aggregate concrete

2. Matrix porosity: the binder matrix is expanded or foamed, e.g., aerated lightweight concrete or foam concrete

3. No fines porosity: the closed structure is turned into a porous structure by reducing the fine grain and matrix content

A combination of the categories is also possible. This thesis investigates a structural lightweight aggregate concrete (short LAC, which corresponds to category 1). This type of lightweight

concrete is similar to normal weight concrete, but the dense aggregates are replaced by porous lightweight aggregates (Thienel, 2018). According to EN 206:2017-1, lightweight aggregates are defined as aggregates of mineral origin in oven-dry state, with grain density smaller or equal to 2000 $\frac{kg}{m^3}$ and bulk density smaller or equal to 1200 $\frac{kg}{m^3}$. The lightweight aggregates can be volcanic (e.g., pumice, tuff), processed natural products (e.g., expanded clay), industrial by-products (e.g., blast furnace slag) or processed industrial by-products (e.g., expanded glass granulate). This thesis focuses on expanded glass granulates.

The basic product recycled glass is a by-product of industrial production. Expanded glass is produced by a thermal manufacturing process. Processed recycled glass is ground into fine glass powder and sintered at 900 °C with the addition of water glass as an adhesive and a carbon-based blowing aid (Faust, 2003). The optimum properties of a high-quality expanded granulate are the ideally spherical shape of the grain, an evenly distributed porosity and a densely sintered outer skin without coarse cracks to keep water absorption as low as possible. Only through careful preparation, uniform materials can be produced, which are preferable over natural lightweight aggregates (Faust, 2003).

2.4.2 Properties of lightweight aggregate concrete

In contrast to other lightweight concretes (e.g., foam concrete), structural lightweight aggregate concrete has a mixture composition and micro-structure similar to normal weight concrete (Faust, 2003). The main ingredients are water, cement, aggregates and possibly additives and admixtures.

The strength and compactness of the concrete are significantly influenced by the water-to-cement ratio ($\frac{w}{c}$-ratio). Besides, admixtures determine the strength development. In lightweight aggregate concrete, the lightweight aggregates have a major impact on the strength of the material. Due to the low density, the mechanism for load-bearing changes in comparison to normal weight concrete (Lusche, 1972). The higher the strength of the lightweight aggregate, the higher the critical strength. The critical strength is reached when the Young's modulus of the matrix exceeds that of the aggregate, so that the aggregates no longer participate in the transmission of forces in accordance with their volume fraction (Thienel, 2018). The strength evolution is similar in lightweight and normal weight concrete. Over time, the total strength of normal weight concrete is higher than of lightweight concrete. Thus, the strength evolution in percentage terms

is faster for lightweight concrete—it reaches already approx. 90 % of its strength after 7 days while the normal weight concrete has reached only approx. 70 % of its strength (Wesche, 1993).

The compressive strength and Young's modulus are generally reduced by the targeted insertion of pores and are thus lower in lightweight concrete than in normal weight concrete. The Young's modulus of the lightweight aggregates lies between 3,000 MPa and 18,000 MPa and thus reaches only a fraction of the Young's modulus of normal aggregates, which are in the range of 20,000 MPa to 115,000 MPa depending on the aggregate type (Wesche, 1993). Depending on the type of aggregate, compressive strength and bulk density of the concrete, the Young's modulus of structural lightweight concrete is between 5,000 MPa and 24,000 MPa. It depends linearly on the density as shown in Thienel (1992). For the same strength class, the Young's modulus of lightweight concrete is only about 30 to 70 % of the values of normal weight concrete. Therefore, the elastic deformations are on average 1.5 to 3.0 times greater for the same stress (Wesche, 1993).

The load-bearing behavior depends on the strength and stiffness ratio of aggregates and matrix. In normal weight concretes, the Young's modulus of the aggregates is usually higher than the Young's modulus of the cement matrix. Thus, the compression stress trajectories are directly running from aggregate to aggregate, see Figure 2.8, left (Lusche, 1972).

For lightweight concrete, the strength initially develops in the same way and the phenomena are the same as in normal weight concrete. However, during hardening, the stiffness and strength of the matrix can exceed that of the aggregates. Thus, the ratio of elasticity reverses, resulting in different force flows: The compressive stress trajectories are in the cement matrix and run around the aggregates (see Figure 2.8, right). The lightweight aggregates increasingly escape the higher load and the mortar layers are subjected to compressive stress. This creates tensile stress above and below the lightweight aggregates orthogonal to the compression trajectories. If the tensile stress exceeds the matrix tensile strength, cracks begin to form. Furthermore, the tensile forces are gradually transferred to the aggregates until finally their tensile strength is reached as well. Thereby, the lightweight concrete reaches its load bearing capacity. This so-called grain fracture determines the upper limit of the compressive strength of the lightweight concrete. (Lusche, 1972; Thienel, 2018)

At the same time, the characteristics of the contact zone in lightweight concrete differ from normal weight concrete. The absorbency and surface porosity of the lightweight aggregates have a positive effect on the contact zone. The formation of water films is prevented and in

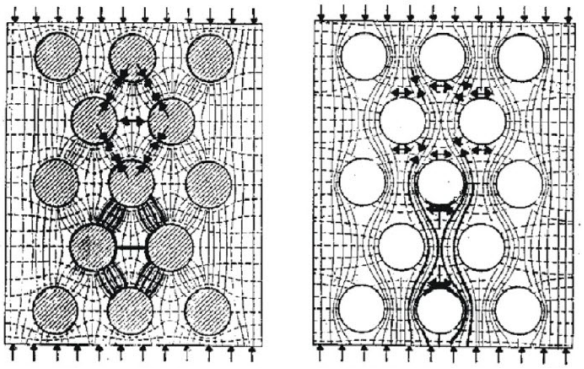

FIGURE 2.8: Load-bearing of normal (left) and lightweight concrete (right) (Lusche, 1972)

addition, mechanical interlocking is sometimes created by the penetration of cement paste into the aggregates.

Besides its influence on the contact zone, the porosity of the lightweight aggregates also affects the characteristics of the concrete. In comparison to normal weight concrete, the low density of the lightweight aggregates leads to a lower thermal conductivity which enables to integrate insulating functions into monolithic building components. The thermal conductivity depends mainly on the air content in the matrix and in the aggregates. The dryer the aggregates, the lower the density. Especially the pore size and the pre-wetting of the lightweight aggregates influence the water content inside the aggregates. Pre-wetting the aggregates leads to higher densities as the voids are filled with water instead of air. It must be noted, that the thermal conductivity is inversely proportional to the strength of the material.

Furthermore, lightweight concrete shows higher temperatures during hydration than normal weight concrete of the same composition due to the lower thermal conductivity and the resulting slower discharge of the heat of hydration (Wesche, 1993). Thus, when drying out or cooling down, there is a greater gradient of moisture and temperature between the surface and the core, which can lead to greater tensile stresses and thus to the formation of cracks on the surface regardless of favorable deformation ratios (low Young's modulus). Despite the internal curing potential through the absorbed core water (Marchon et al., 2018), the lightweight concrete must therefore be carefully protected from drying out and cooling down too quickly (Wesche, 1993). The internal stresses might furthermore reduce the flexural tensile strength by up to 60 % compared to the strength when stored in water (Wesche, 1993) which is compensated as soon as a moisture equilibrium is reached.

However, the internal curing due to the moisture stored in the lightweight aggregates does also have positive effects. Due to its good internal curing, lightweight concrete is at least as durable as a correspondingly composed normal weight concrete (Thienel, 2018; Thienel et al., 2020). The classification of lightweight concrete into exposure classes is not based on strength, but is essentially dependent on the composition of the matrix ($\frac{w}{c}$-ratio, cement content, air void content) as well as the type of aggregates (Thienel et al., 2000). In terms of freeze-thaw exposure and exposure to de-icing salt, lightweight concrete has a better durability than normal weight concrete and thus, is often applied in such areas (Thienel, 1992).

2.4.3 Water absorption of lightweight aggregates

When studying the behavior of lightweight aggregate concrete, the degree of saturation and the absorption behavior of the lightweight aggregates should be taken into account (Faust, 2003). The water absorption in lightweight aggregate concrete is usually greater than that in normal weight concrete and is only approximately the same when the grain surface is well sintered. Nevertheless, the waterproofness of hardened lightweight aggregate concrete, i.e., the penetration depth under water pressure, as well as the water vapor permeability is about the same as those of normal weight concrete (Wesche, 1993).

In artificial lightweight aggregates, the grain pores usually amount to more than 45 % of the grain volume. Dry aggregates are able to absorb water and even to extract water from fresh concrete. This might happen during mixing of the concrete, but also in the period until the lightweight concrete sets. It leads to stiffening of the concrete and the water absorption might even accelerate the setting of the fresh concrete. The stiffening can be reduced by pre-saturation. However, a distinction must be made between the various lightweight aggregate types. Depending on the aggregate, the water absorption can differ in speed and in the amount of water absorbed (Thienel, 2018). It is determined by the pore structure and above all by the density of the outer skin of the lightweight aggregate grains. According to Hermann (1974) the water absorption varies between 3 and 20 % by mass which corresponds to a filling of 10 to 60 vol.% of the pores of the aggregates. The water absorption per time unit is considerably larger in the beginning. According to Hermann (1974) the water absorption in the first seconds under atmospheric pressure correspond to 50 % of the water absorption over 60 minutes. The declining course is due to the increasing pressure inside the aggregates (Rossig, 1974). Note that the theoretical water absorption according to the Boyle-Mariotte law (which states that the pressure of ideal gases

at constant temperature is inversely proportional to the volume) is larger than the real water absorption in lightweight aggregate concrete (Rossig, 1974). Domagała (2015) states, that the water absorption in lightweight aggregate concrete might be 60-100% of the absorption when the lightweight aggregates are surrounded by water depending on the fresh concrete properties.

In order to evaluate the real water absorption of lightweight aggregates, the time of prewetting must be considered. If dry lightweight aggregates are pre-wetted directly before mixing with water, the outer area of the grain will be saturated first and the core will initially remain dry. Also, fully saturated lightweight aggregates start drying from the outside, while the core remains saturated (Thienel, 2018). The status of the drying process influences the water absorption during mixing and pumping. If the lightweight aggregates started to dry again after pre-saturation, they absorb more water than freshly pre-saturated aggregates (Faust, 2003).

When exposed to pressure, the water absorption increases compared to atmospheric pressure (Bauer and Poppy, 1974). Under pressure, a maximum value of water absorption is reached in a short time, which then remains almost constant, since the air cannot necessarily escape, but is compressed according to the Boyle-Mariotte law. Therefore, at any given pressure, only a certain amount of water can enter the grains. Since the volume of air decreases hyperbolically with increasing pressures, the correlation between pressure and water absorption is also hyperbolic. Thus, a further increase in pressure leads only to insignificant increase in water absorption.

The water absorption decreases with increasing grain density. However, the degree of pore filling of the heavy, i.e., low-pore material is particularly high. The assessment of water absorption should therefore always be based on several reference values (Bauer and Poppy, 1974). When water absorption is shown in relation to grain weight, there are even greater differences between various lightweight aggregates than in relation to grain volume (Bauer and Poppy, 1974). Long-term tests showed that even after 100 days the water absorption is still not complete (Bauer and Poppy, 1974). Bauer and Poppy (1974) states, that the water absorption of a grain size distribution is significantly influenced by the different grain size fractions. Different grading curves therefore show different water absorption.

Furthermore, Bauer and Poppy (1974) found that the water absorption increases with mechanical stress or when the surface of the lightweight aggregates is not well sintered. This is due to the accessibility of the pores for water.

Bauer and Poppy (1974) found that the compressed air in the pores of the lightweight aggregates expands after a pressure drop (e.g., at the end of the pumping process) and part of the water

leaves the pores. This phenomenon starts rapidly and continues over a long period of time. Overall, the remaining water saturation in the pores stays higher for aggregates which were exposed to pressure than for aggregates at atmospheric pressure. Furthermore, Bauer and Poppy (1974) state that the water absorption is almost identical in cement paste as in water, but the water release is less when the lightweight aggregates are surrounded by cement paste as the resistance of the stiffened cement paste is higher than of water. When hydration continues to progress and the pore structure of the hardened cement paste becomes finer some of the water is released from the lightweight aggregates again via the increasing capillary effect. It can take years to achieve an equilibrium moisture content in the concrete. This results in a long-lasting internal curing of the concrete. However, the excess water up to that point increases thermal conductivity and can reduce resistance to freeze-thaw cycles and fire, as well as increases the influence of shrinkage and creep. Thus, the pre-saturation must be limited (Bauer and Poppy, 1974; Wesche, 1993).

All in all, the water absorption is dependend on the time, pressure, mechanical stress and material characteristics. Up to now, the methods to avoid water absorption like sintering, making it water-repellend or coating are either technically imperfect, and thus not working under pressure, or mechanical stress or cost-intensive.

2.4.4 Pumpability of lightweight aggregate concrete

The pumping of lightweight concrete is not studied and understood as much as normal weight concrete. However, in the 70s and 80s there has been research on the challenges in pumping of lightweight aggregate concrete (e.g., Aurich, 1971; Weigler and Karl, 1972; Bauer and Poppy, 1974; Rossig, 1974; Hermann, 1974). They mention the high water absorption of the lightweight aggregates under pressure as the cause of the malfunctions during pumping. This is still studied in more recent literature (e.g., Haist et al., 2003; Haist and Müller, 2005; Arkhipkina et al., 2019). Nübling (1971) categorizes concrete as Bingham substance for which the pumpability is defined by shear viscosity and shear stress, if the pipe diameter and the pumping velocity are known. However, (Weber, 1963; Rossig, 1974) found that coarser aggregates migrate so that lightweight concrete is also expected to flow as a plug and form a lubrication layer on the peripheral of the pipe (see Section 2.4.4). With increasing viscosity, the magnitude of the plug decreases (Rossig, 1974).

During pumping, the water absorption increases due to the pressure generated during pumping. Rossig (1974) observed water absorption in the range of 54-74 % of the pore volume of the lightweight aggregates leading to a change of the fluidic effective w/c-ratio in the cement paste from 0.5 to 0.3 and thus to a stiffer consistency. A stiffening effect was also observed by, e.g., Hermann (1974) and Rahul and Santhanam (2020). The increased water absorption leads to a depletion of the lubrication layer making the concrete stiffer and impeding its pumpability (Rapp, 1971; Wesche, 1993). Rapp (1971) found an increase in density and decrease in the spread flow (which suggests an increase in yield stress) during pumping. Rossig (1974) also found a decrease in spread flow from 480 mm to 400 mm and noted an increase in both, viscosity and yield stress due to decreasing w/c-ratio. Furthermore, he found an increase in density from 1.7 kg/dm³ to 2.3 kg/dm³ which corresponds to a difference of 0.6 kg/dm³. The changes during pumping also lead to an increase in strength and thermal conductivity (Arkhipkina et al., 2019).

At the end of pumping, i.e. after pressure discharge, partial release of the absorbed water might occur. The water leaves the aggregates as the encapsulated air inside the aggregates relaxes (Bauer and Poppy, 1974), see also Section 2.4.3. Thus, the behavior of lightweight aggregate concrete exposed to a pumping pressure is not only compressible but also elastic (Faust, 2003). Concerning concrete extrusion, this might be an advantage, i.e. providing internal curing (Marchon et al., 2018), over normal weight concrete, where cracks might occur due to drying out resulting from the lack of formwork (Roussel, 2018).

The water absorption is one of the main differences to normal weight concrete. According to Rossig (1974), lightweight aggregate concrete with dry aggregates might behave as a time-dependent rheopectic fluid while with pre-wetted lightweight aggregates it has a nearly time-independent Bingham behavior. According to Faust (2003) and Haist and Müller (2005), it is therefore particularly important to pre-saturate the lightweight aggregates when pumping lightweight concrete. Hermann (1974) compared differently pre-saturated lightweight aggregates with each other. He found that the consistency of the concrete changes drastically during pumping when using dry aggregates and an elevated mixing water content. Also at minor pre-saturation of approx. 10 - 30 vol.% of the grain pores, the consistency of lightweight aggregate concrete changed from plastic to stiff consistency. Applying a vacuum pre-saturation of 50 - 60 vol.% of the grain pores, only minor changes in consistency occurred (Hermann, 1974). This is in line with the findings of Reilly (1972) who investigated pre-saturation of approx. 70 vol.%. However, according to Wesche (1993) the phenomenon of water absorption and stiffening of the concrete during pumping may even be the case despite a preceding, longer (24 hours) water

storage of the lightweight aggregate. Even if the aggregates are vacuum treated, the consistency is still noticeably affected during pumping (Wesche, 1993).

Hermann (1974) suggests to estimate the amount of absorbed water during pumping based on the fresh concrete density. An exact calculation is not possible as the air void content of lightweight concrete can not reliably be measured in the fresh state. He calculates the absorbed water volume as

$$V_{w_a} = \frac{C}{\rho_C} + \frac{Ag}{\rho_{Ag}} + \frac{w_t}{\rho_w} + V_{air} - \frac{C + Ag + w_t}{\rho_f}, \tag{2.18}$$

with cement content C, cement density ρ_C, aggregate content Ag, mean density of the aggregates ρ_{Ag}, total water content w_t, density of water ρ_f, air void content V_{air}, and fresh concrete density ρ_f. The additional water absorption during pumping is estimated based on the difference between the absorbed water w_a before and after pumping. Depending on the aggregate type, Hermann (1974) found additional water absorption of up to $60\,\mathrm{dm^3/m^3}$. This is in the magnitude of the results of Rossig (1974) on the lightweight aggregate Liapor when calculating them in the same manner. Even though the change in consistency was minor for the vacuum pre-saturated mixtures, the additional absorption of water cannot be denied even in this case (Hermann, 1974). Besides, it has to be kept in mind that these amounts of water involve the described worsening effect on shrinkage and creep, see Section 2.4.3.

The air in pores, which were not filled with water before pumping, allows further water absorption only according to its compression. At strokewise pumping, the alternating pressure in individual pump strokes (Hermann, 1974) leads to an increase in the water remaining in the aggregates (Rossig, 1974). The water absorption increases with the number of pressure cycles. Thus, pumping of material at alternating pressure is suspected to lead to a higher absorption of water and as a consequence to stiffening of the concrete and an increasing potential for blockages in the hose. This is in line with the findings of Bauer and Poppy (1974), that the water absorption is higher than the release at alternating pressure and thus the surrounding cement paste stiffens and might loose its pumpability. This is not reversible and according to Bauer and Poppy (1974) cannot be completely avoided by pre-saturation. Rossig (1974) found that blockages occur especially at bends and when the pump is not run homogeneously, but in on-off-mode.

The formation of a lubrication layer, which enhances pumpability, is deteriorated if less water and cement paste are at disposal, see Section 2.4.4. Thienel (2018) and Haist et al. (2003) assume that under pressure, parts of the cement particles will also enter the porous grain together with

the absorbed water. This increases the strength of the concrete, but also its density (Thienel, 2018). According to Rossig (1974), only water and air can enter the open pores driven by the pressure difference due to the permeability of the lightweight aggregates and the viscosity of air, water and cemente paste (ratio of approx. 1:55:16,000). However, he also states that due to partial destruction and grain abrasion cement paste intrusion might be possible. According to Thienel (2018), the changes in density can be remedied by specially adapted, very flowable formulations. In contrast, Hermann (1974) states that it is not sufficient to define a consistency in the beginning as the stiffening effect will nevertheless prevent pumping over longer distances. Furthermore, with regard to the work at hand, a very flowable mixture is not suitable for 3D-printing as the requirements on contour precision can not be fulfilled. Thus, a prediction of the effects during pumping and a targeted design for the desired application have to be studied.

The pumpability of lightweight concrete can not be predicted based on models for normal weight concrete when not completely saturated (Rossig, 1974). The water absorption of lightweight aggregates can lead to a significant deviance in the pumping behavior and the the properties of the lightweight aggregate concrete. Up to now there are only very few investigations on lightweight concrete extrusion, e.g. Rahul and Santhanam (2020) who conducted tests with a piston pump and reported de-watering and stiffening of the lightweight concrete during pumping partially leading to blockages. Furthermore, Li Wang et al. (2020) conducted research with different ratios of coated lightweight ceramsite sand to silica sand. However, they did not focus on the fresh material properties, but on the mechanical strength of different hollow structures. The connection between pumpability and buildability is not yet analyzed satisfactorily. Especially, the prediction of material changes during pumping of a material and their influence on the buildability need further investigations.

3 Methods and test environment

3.1 Overview of objectives and investigations

The major objective of this thesis is to analyze how the evolution of material characteristics during extrusion affect lightweight aggregate concrete extrusion and vice versa. The investigations cover three different scales: on a micro scale the evolution of the characteristics of the lightweight aggregates, on a meso scale the material characteristics of fresh and hardened lightweight aggregate concrete and on a macro scale the effect of the material characteristics on pumpability and buildability of lightweight aggregate concrete, see Figure 1.3. As the properties of lightweight aggregate concrete change during pumping, the investigations must include material tests before and after pumping as well as basic research on the effects introduced by pressure.

Figure 3.1 gives an overview of the investigations, which are conducted during this thesis. In general, experiments are conducted on a laboratory mixer (see left part in Figure 3.1) and on the extrusion system itself (see right part in Figure 3.1). The laboratory tests are conducted in order to profoundly analyze the influence of individual parameters taking into account the reproducibility of effects. Tests on the lightweight aggregates are conducted (see Section 3.5) as they are crucial for the characteristics of lightweight aggregate concrete in contrast to normal weight concrete. In the extrusion setup, the amount and condition of the lightweight aggregates is examined (micro scale), material is analyzed in fresh state before and after pumping (meso scale), and mould prisms are produced for tests on hardened concrete (meso scale). Furthermore, extruded elements are cut in prisms for hardened concrete investigations including the effects of layerwise deposition.

For pumpability, mixtures are compared with regard to pressure and flow rate in real pumping tests with a progressive cavity pump (macro scale, see Section 3.6). The results on yield stress, structural build-up, density and green strength are used to draw conclusions about the changes

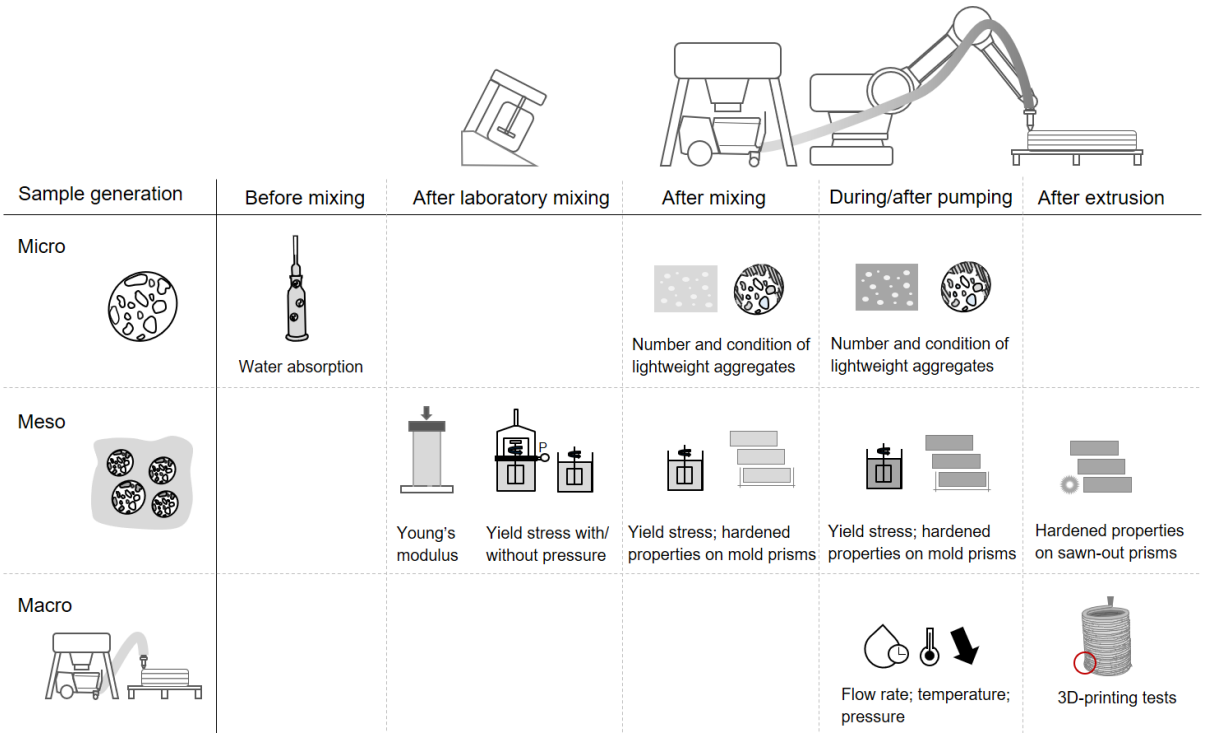

FIGURE 3.1: Overview of investigations conducted in laboratory tests and on the extrusion setup

during pumping and their effect on extrusion. Especially, rheology and green strength are investigated to calculate possible building rates. Based on the static rheological measurements, buildability is calculated according to models developed for normal weight concrete as well as according to further models developed thereupon (see Section 3.7). The results are validated with real buildability tests (macro scale) on the setup of lightweight aggregate concrete extrusion as described in Section 3.4. Investigating interdependencies between pumpability, buildability and rheological parameters, a prediction of the suitability for extrusion is targeted.

All experiments are conducted at laboratory atmosphere at 20±3 °C and 65±5 % relative humidity. A uniform mixing order is established to eliminate confounding effects, see Section 3.3. For laboratory testing, the mixing is conducted in a laboratory mixer type R02 by Eirich at a speed of rotation of 840 rpm. For the larger tests, the mixing regime is kept the same, but is conducted at a concrete mixer with a volume of 100 l and a speed of rotation of 56 rpm.

Simultaneously to the fresh concrete tests, specimen for hardened material properties are produced. In order to evaluate the application possibilities of the extruded lightweight aggregate concrete (see Section 4.5), mould prisms as well as prism sawn-out of extruded elements are

produced. Mettler et al. (2016) show the adequacy of standard compression and shear mechanical tests for printable materials. The prisms sawn-out of extruded elements help to evaluate the effect of the layerwise production without external compaction. Furthermore, the thermal conductivity and the density are examined on the prisms (see Section 3.8).

3.2 Materials

The lightweight aggregate concrete contains an Ordinary Portland Cement (OPC) with a density of 3.1 $\frac{kg}{dm^3}$, a mean particle size of $d_{50,C} = 7.9\,\mu m$ and a specific surface of $A_{Blaine,C} = 6,040\,\frac{cm^2}{g}$. Furthermore, the binder contains limestone powder (LSP) with a density of 2.7 $\frac{kg}{dm^3}$, a mean particle size of $d_{50,LSP} = 15.7\,\mu m$ and a specific surface of $A_{Blaine,LSP} = 3,610\,\frac{cm^2}{g}$. The chemical composition and the particle size distribution of OPC and LSP are depicted in Table 3.1 and Figure 3.2.

Table 3.1
Chemical composition of cement and limestone powder

	SiO_2 [wt.%]	CaO [wt.%]	Al_2O_3 [wt.%]	Fe_2O_3 [wt.%]	Other [wt.%]
OPC	20.7	62.5	5.6	2.5	8.5
LSP	2.8	53.2	0.7	0.4	43.8

Furthermore, silica fume (Sf) with $d_{50,Sf} = 0.15\,\mu m$ and a density of 2.3 $\frac{kg}{dm^3}$ was used.

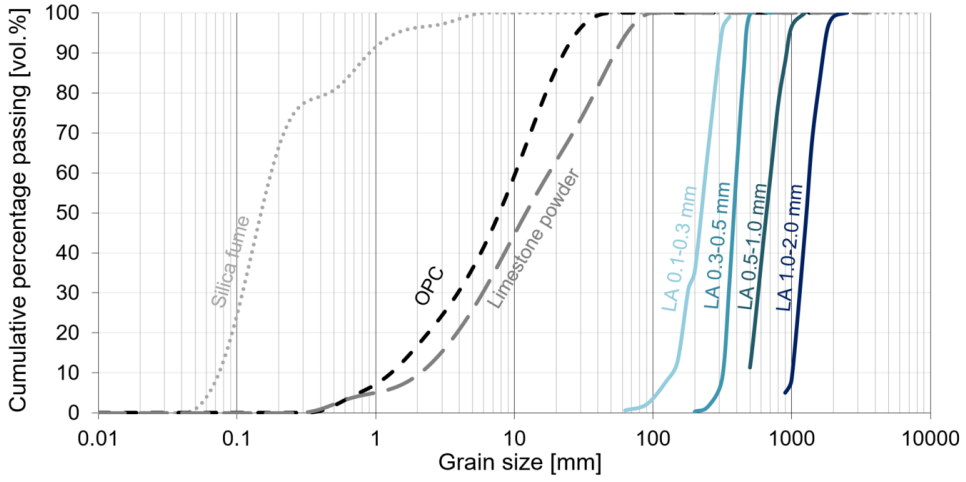

Figure 3.2: Grain size distribution of cement (OPC), limestone powder, silica fume and lightweight aggregate grain size fraction 0.1-0.3 mm (LA 0.1-0.3 mm), 0.25-0.5 mm (LA 0.3-0.5 mm), 0.5-1.0 mm (LA 0.5-1.0 mm) and 1.0-2.0 mm (LA 1.0-2.0 mm)

A polycarboxylate ether (PCE) based superplasticizer was added. It has a solids content of 40 %. The water content is counted towards the water added. Furthermore, a polymer based air void stabilizer and a synthetic co-polymer based thixotropy enhancing agent were used in order to increase the elasticity of the lightweight concrete strands and avoid segregation and tearing-off as well as to reduce the conflict between pumpability and buildability.

Expanded glass granulate with a maximum grain size of 2 mm is used as lightweight aggregate. The particle size distribution of the lightweight aggregates is constant for all experiments (Figure 3.2). The density of the expanded glass granulates is 0.3-0.9 $\frac{kg}{dm^3}$ depending on the grain size and the grain strength is in the range of 1.4 MPa to 2.8 MPa, see Table 3.2. As it is a mineral aggregate, expanded glass granulate does not influence the reaction of the concrete (Neunast and Lange, 2001; Faust, 2003). To avoid segregation or blocking in the pump, the grain size distribution is designed as coarse to medium grained comparable to the A-curve in EN 206:2017-01.

The lightweight aggregates absorb water depending on both, the prevailing pressure P and the time of exposure t_e. The pressure in the pump is however, among others, dependent on the water content of the mixture and the material composition as will be studied in Chapter 4. Thus, the total amount of absorbed water w_A cannot be calculated precisely in advance (Matthäus et al., 2019). Since the pressure during pumping is at least equal to the atmospheric pressure, the water absorption at atmospheric pressure for different exposure times $w_{A,atm}(t_e)$ as provided by the producer can be regarded as lower limit for water absorption during pumping. The maximum amount of absorbed water $w_{A,max}(\Phi_{void})$ is determined by the open void fraction of the lightweight aggregates Φ_{void}.

TABLE 3.2
Characteristics of lightweight aggregates according to Dennert Poraver GmbH (2018)

	Density [kg/dm^3]	Grain strength [MPa]	Water absorption at 5 bar over 5 min [wt.%]
0.1-0.3 mm	0.9	4.5	35
0.25-0.5 mm	0.7	2.6	21
0.5-1.0 mm	0.5	2.0	18
1.0-2.0 mm	0.4	1.6	19

For the mix design the water which the aggregates absorb according to the producer over a time of 5 minutes at a pressure of 5 bar is added to the mixing water w to account for the water absorption in the pump. The water required for each aggregate grain size fraction is calculated

using the quantity of lightweight aggregates and the sum of predicted water absorption w_A is added to the mixing water w.

In order for the material properties not to change drastically during pumping, the aggregates are pre-wetted with two thirds of the total water $w_t = w + w_A$ over 5 minutes before preparing the lightweight aggregate concrete. The pre-wetting is considered in the mixing regime, see Section 3.3 (Table 3.4).

3.3 Mix design

In this thesis, the focus lies on a mixture used to produce extruded lightweight aggregate concrete elements. In addition, variations are used to better investigate individual effects, especially during pumping and under pressure. The compositions are referred to as lightweight aggregate concretes in the tradition of literature on extrusion whereby they correspond to mortars in the nomenclature of general building materials concerning the maximum grain size.

Table 3.3 gives an overview on all mixtures. The 'main' mixture M.PS 5min was developed for concrete extrusion (Matthäus et al., 2021). It consists of limestone cement with 80 vol.% OPC and 20 vol.% LSP, which is equal to 82.2% OPC and 17.8% LSP by mass. Furthermore, the binder contains 10 wt.% silica fume. This results in a final composition of 74 wt.% OPC, 16 wt.% LSP and 10 wt.% silica fume. Furthermore, a PCE with 0.45 wt.% w.r.t. cement, a polymer based air void stabilizer (AVS) with 0.5 wt.% w.r.t. cement, and a synthetic co-polymer based thixotropy enhancing agent (TEA) at a dosage of 0.5 g/l water are added. The water/binder ratio is w/b=0.39 by mass excluding water for water absorption. The concrete composition consists of 47 vol.% paste (V_p) and 53 vol.% aggregates (V_{Ag}): $\frac{V_p}{V_{Ag}} = 0.89$. The volume fractions of the aggregates are 22 vol.% 0.1-0.3 mm; 21 vol.% 0.25-0.5 mm; 22 vol.% 0.5-1.0 mm and 35 vol.% 1.0-2.0 mm. The mix design is summarized in Table A.1 in the Appendix.

The air void stabilizer and the thixotropy enhancing agent are omitted for some investigations in order to exclude the influence of the admixtures in basic research as well as to be able to reliably perform sensitive tests with more flowable consistency. Those mixtures are referred to as 'simplified mixtures' S, see Table 3.3.

TABLE 3.3
Overview on mix designs

The overview on the mixtures involves the type of admixtures, the pre-saturation (PS) time, the lightweight aggregate (LA) grain size fractions, and the volume ratio between LA and cement paste. The types of admixtures include PCE superplasticizers, thixotropy enhancing agents (TEA), and air void stabilizers (AVS).

	Mixture	Admixtures [-]	Pre-saturation [min/d]	LA grain size fractions [mm]	Approx. volume ratio LA:paste
Main	M.PS 5min	PCE, TEA, AVS	5 min	0.1-2.0	1:1
	M.PS 9d	PCE, TEA, AVS	9 d	0.1-2.0	1:1
Simplified	S.PS 5min	only PCE	5 min	0.1-2.0	1:1
	S.PS 2d	only PCE	2 d	0.1-2.0	1:1
	S.PS 7d	only PCE	7 d	0.1-2.0	1:1
Grain size fraction	LA0.3 V1:2	only PCE	5 min	0.1-0.3	1:2
	LA0.5 V1:2	only PCE	5 min	0.25-0.5	1:2
	LA1.0 V1:2	only PCE	5 min	0.5-1.0	1:2
	LA2.0 V1:2	only PCE	5 min	1.0-2.0	1:2
	LA2.0 V1:4	only PCE	5 min	1.0-2.0	1:4

Based on results in preliminary investigations (Forstmaier and Matthäus, 2020), the influence of the pre-saturation on the behavior during the pumping process helps to understand the effects during pumping of lightweight aggregate concrete. The effect of pre-saturation (PS) is investigated on both types of reference mixtures M.PS 5min and S.PS 5min. All mixtures contain the same amount of silica fume, the same distribution of lightweight aggregates, the same volume ratio between cement paste and aggregates and a w/b-ratio of 0.39 by mass excluding the water for water absorption. The reference mixture M.PS 5min (pre-saturation of 5 minutes) is compared to mixture M.PS 9d, where the lightweight aggregates are pre-saturated over 9 days. In addition, the mixture S.PS 5min is compared to mixtures with a pre-saturation time of 2 days (S.PS 2d) and 7 days (S.PS 7d) for a more detailed investigation.

All mixtures are mixed according to a uniform mixing regime (see Table 3.4) and the lightweight aggregates are pre-saturated with 2/3 of the mixing water. In order to be able to compare the mixtures with pre-saturation times longer than 5 minutes, the amount of pre-wetting water is adapted for every pre-saturation time span until the same consistency is achieved as for

the reference mixture. Thus, the total w/b-ratio is larger for the mixtures, which are pre-saturated longer than 5 minutes, due to the dependency of the water absorption of the lightweight aggregates on pre-saturation time (see Section 3.2).

TABLE 3.4
Mixing regime

This table describes the mixing procedure. The timeline refers to the addition of the mixing water.

	Duration [s]	Timeline [min : s]
Mixing of dry aggregates and absorption water (pre-wetting)	60	-6:00
Rest period (water absorption)	240	-5:00
Cement addition (and if applicable powdery admixtures)	60	-1:00
Addition of mixing water and PCE, mixing	45	0:00
Homogenization (with a scraper)	60	0:45
Further mixing	45	1:45
End of mixing process	-	2:30

3.4 Process parameters for lightweight concrete extrusion

For the extrusion of lightweight aggregate concrete, a progressive cavity pump is attached to a manipulator via a 10 m hose. The hose has a inner diameter of 25 mm and consists of a flexible synthetic material. As manipulator, a six-axis industrial robot is used, c.f. Figure 3.3.

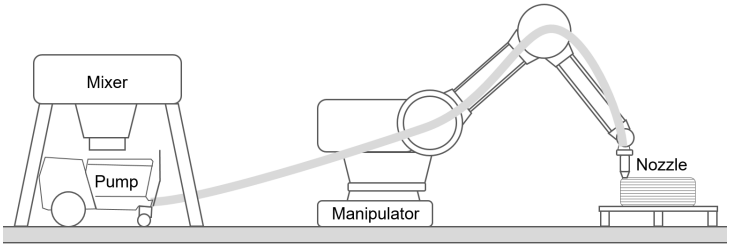

FIGURE 3.3: Setup of lightweight aggregate concrete extrusion in this thesis

The progressive cavity pump PFT Swing L FC-400V is optimized for mortar applications and limits the maximum grain size to 2 mm or 4 mm depending on the applied stator and rotor. The premixed material is transported via a screw conveyor in the filling container to the eccentric screw pump connected in series. The material is further pumped through a hose with a inner diameter of 25 mm. A pressure manometer is integrated at the beginning of the hose and records the pressure in the pipe every five seconds. The velocity of the pump is continuously adjustable via the frequency of the shaft. For the application in this thesis, in a frequency range between 0 Hz and 30 Hz was investigated.

As described in Matthäus et al. (2021) and Henke et al. (2020), different types of nozzles can be applied to the system. They are connected to the hose after a pinch valve which serves to stop the material flow briefly if needed. The experiments in this thesis are based on a round nozzle which reduces the opening tapered over a length of 7 mm to a diameter of 15 mm. Round nozzles pose the greatest challenge to buildability as the surface connected to the next layer is smaller than at strands with a rectangular cross-section. Furthermore, the material is sheared at the nozzle and the structural built-up is partly destroyed (Roussel, 2018). Thus, the requirements for the material are comparably high and calculations are on the save side also valid for other types of nozzles, e.g. with a rectangular cross-section.

3.5 Investigations on the lightweight aggregates

3.5.1 General considerations

The lightweight aggregates play a crucial role in pumpability and the resulting characteristics of the material after pumping. The lower the density of the lightweight aggregates, the higher is in general their porosity and thus their water absorption (Bauer and Poppy, 1974). Furthermore, the water absorption increases with increasing pressure and stress (Bauer and Poppy, 1974).

Besides water absorption tests which are done on the lightweight aggregates themselves, two types of tests are conducted on the concrete mixture to asses the condition of the lightweight aggregates before and after pumping (micro scale):

1. Sieving and wash-out of lightweight aggregates from the lightweight concrete after pumping (see Section 3.6.3), determination of the amount of lightweight aggregates per liter lightweight concrete and calculation of their density.

2. Optical assessment of the degree of destruction and filling with cement paste on sawn samples.

In order to determine the change in density during pumping, the tests are conducted with the material before and after pumping.

3.5.2 Water absorption tests

For more detailed investigations and validation of the data of the manufacturer, both, the water absorption of the individual grain size fractions and the water absorption of the entire grading

curve are determined. A glass pycnometer with a measuring mark at the top piece is used to carry out the experiments on water absorption. The total volume up to the measuring mark is determined by filling the pycnometer with water. For the experiments, a predefined amount of dry lightweight aggregates with known weight m_A is filled into the pycnometer followed by filling the pycnometer with water up to the measuring mark. A filter keeps the lightweight aggregates, which would float up, at the bottom so that the water level can be set exactly to the measuring mark (Figure 3.4). Through the difference in mass, the initial volume of the lightweight aggregates V_A is determined.

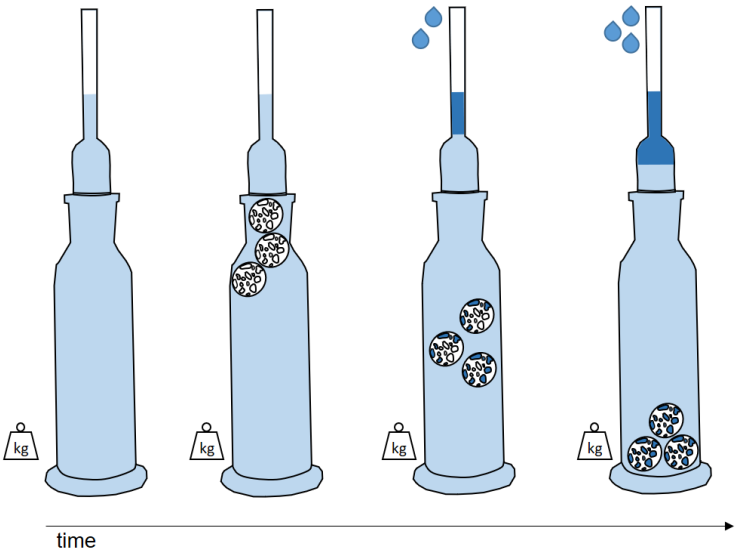

FIGURE 3.4: Setup to determine the water absorption of lightweight aggregates: recording the weight while keeping the predefined volume constant over time

Further measurements determine the water absorption: When the water level drops due to water absorption, the pycnometer is weighed as a control in its current state and then refilled with water up to the measuring mark and weighed again. In doing so, the weight is determined over time for a constant volume (Figure 3.4). The measurements are done every 5 minutes for the first 30 minutes. Furthermore, measurements are taken after 60 minutes, 1 day, 2 days, 7 days, 9 days and for some mixtures also additionally over a longer period of time. Adhering air bubbles are removed by gentle shaking. The water absorption is determined by the difference in weight between two measurements over a time period and accumulated over the whole time period under consideration. Relating these values to the initial weight of the lightweight aggregates m_A, the water absorption can be determined in wt.%. Relating it to the initial volume V_A provides the water absorption w_a in vol.%.

The water absorption is measured for the individual grain size fractions of the lightweight aggregates as well as for the grain size distribution in mixture M.PS 5min which is equal to S.PS 5min. Based on the water absorption w_a and the pore volume Φ of the lightweight aggregates, the pore filling Φ_{fill} is calculated: $\Phi_{fill} = \frac{w_a}{\Phi}$. The pore volume Φ results from the raw density ρ_0 of the glass granulates and their density ρ: $\Phi = \left(1 - \frac{\rho}{\rho_0}\right) \cdot 100\%$ and is equal to the theoretical maximum water absorption in vol.%. The raw density ρ_0 of soda lime glass which is the basis for expanded glass granulates is $2500\,\mathrm{kg/m^3}$ according to the manufacturer.

3.5.3 Wash-out of lightweight aggregates

During the pumping tests (see Section 3.6.3), 1 liter of lightweight aggregate concrete is washed-out over a sieve with a size of 0.5 mm. This separates the coarser lightweight aggregates from the cement paste and the fines. Comparing the material before and after the pumping process, it can be evaluated whether the quantity of coarser lightweight aggregates undergoes changes during the pumping process. Further, it enables to draw conclusions about the condition of the lightweight aggregates with regard to their weight. In order to create comparable conditions, e.g., to prevent the cement paste contained in the outer pores of the lightweight aggregates from being washed away to different extents, the material is washed out in each case at the same intensity and over an equal period of time (10 minutes). Directly after sieving, the lightweight aggregates are weighed. In addition, the dried lightweight aggregates are weighed again at least after 7 days, 14 days, 28 days, 36 days and 180 days. Besides, the volume of the lightweight aggregates is recorded and the mean bulk density is calculated.

The bulk density at different time periods after the experiment is compared to the lightweight aggregates which were not pumped and to the original bulk density of the 0.5-2 mm lightweight aggregates in the mix design of mixture M.PS 5min. Furthermore, the lightweight aggregates are dried slowly in an oven at 50° C after a long period of time (180 days) to assess whether the increase in weight is reversible.

3.5.4 Microscopy investigations

Visual evaluations are carried out both on hardened lightweight concrete specimens (see Section 3.6.3) and on the sieved lightweight aggregates (see Section 3.5.3). For the visual evaluation, the hardened concrete prisms (produced parallel to the pumping tests, see Section 3.6.3) are first sawn transversely so that the cross-section (40 cm x 40 cm)of the prism can be analyzed. Then the sawn material slices are sprayed with phenophthalein (0.01 wt.% in 90 vol.% ethanol) to color the cement paste. The cement matrix turns pink in contrast to the lightweight aggregates, which remain white, due to the pH value of the cement matrix. As an alternative, the cement paste is colored by pigments which makes the process more independent of the material age of the samples as the coloring with phenophthalein only works as long as the sample is not yet carbonated.

Using photos of the cross-section of the treated hardened concrete slices, the number of lightweight aggregates, including the respective diameter, is recorded with the aid of an image evaluation software. Figure 3.5 shows the semi-automated counting of the lightweight aggregates. For each numbered aggregate, the area is calculated. On basis of this data, the amount of aggregates of each grain size can be evaluated.

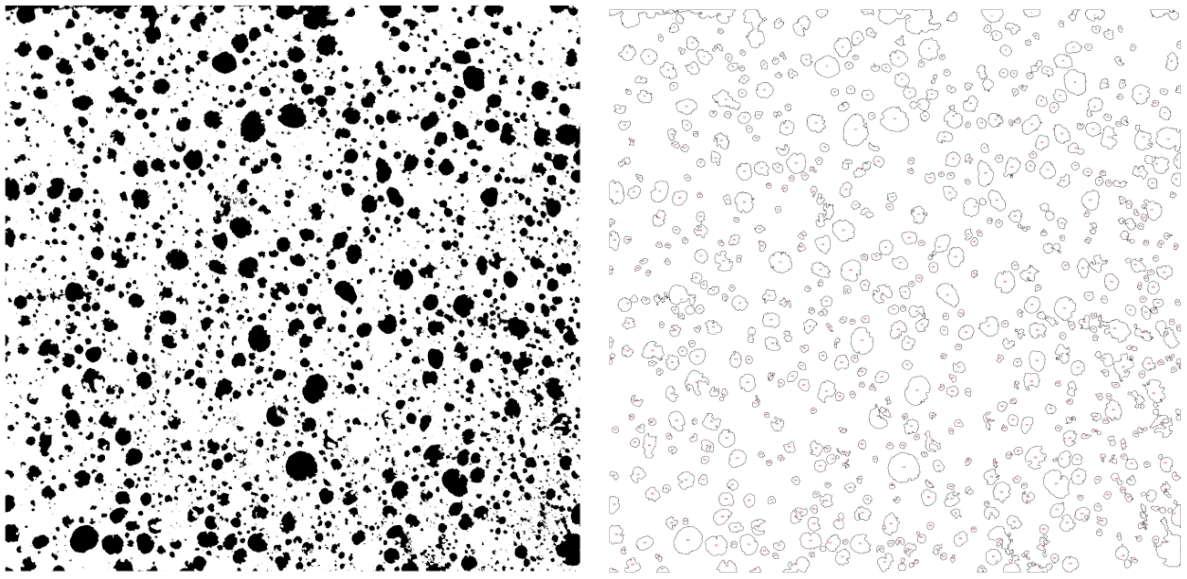

FIGURE 3.5: Calculation of the amount of lightweight aggregates: adjustment of threshold value (left) and results of the count (right).

Furthermore, this information is used to calculate how the percentage of lightweight aggregates

of the various diameter categories behaves in the cross-section compared with the original percentage distribution according to the mix design. It must be noted that this can only be used as a first estimate, as it is only a 2D slice and therefore the actual content in 3D might be overestimated with regard to the smaller grains and underestimated for the larger grains, see Figure 3.6.

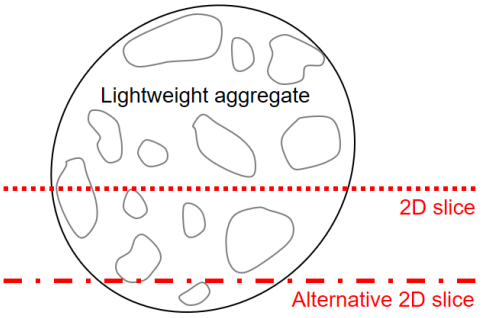

FIGURE 3.6: The position of the slice affects the detected diameter of the lightweight aggregate

After an adjustment of the threshold value, the lightweight aggregates are detected automatically and counted in the cross section by the image evaluation software (Figure 3.5). The detected areas are displayed by the program and are at random compared with the original to check if the areas are detected correctly. In order to determine the diameter, the areas are assumed to be circular. In this way, the number of spheres of the corresponding diameters and the share of the respective diameter category in the total result is estimated. This is in turn compared with the proportion in the original mix design.

Besides the amount of the aggregates, the conditions of individual lightweight aggregates are investigated under the microscope. With up to 6-fold magnification, the lightweight aggregates are examined with regard to damage and penetrated cement paste. This analysis is done both on the lightweight concrete slices and on the sieved lightweight aggregates. The individual aggregates are evaluated with regard to their surface and also cut into half in order to analyze the condition of the pores inside the lightweight aggregates.

3.6 Investigations for workability assessment

3.6.1 General approach

Prior tests (Matthäus et al., 2019, 2020) and literature (see Section 2.4.4) suggest that lightweight aggregate concrete changes its density during pumping. It is hypothesized this change is due to water and cement paste absorption and partial destruction of the lightweight aggregates (micro scale). In order to evaluate the suitability of lightweight aggregate concrete for the extrusion process (macro scale) and to understand the evolution of the material during the process (meso scale), several fundamental measurements are necessary. To this end, a series of experimental tests is conducted mainly on the reference mixture M.PS 5min which was successfully used for extrusion:

1. Specific investigations on the lightweight aggregates (Section 3.5);
2. Dynamic rheological measurements (Section 3.6.2);
3. Pumpability evaluation with measurement of pressure and flow rate (Section 3.6.3);
4. Rheological measurements in a pressure cell (Section 3.6.4);
5. Static rheological measurements and compression tests. (Section 3.7);

The understanding of changes of the characteristics of the lightweight aggregate concrete is crucial as the material characteristics at the nozzle determine the suitability for the remaining extrusion process. To this end, the rheology is investigated before and after the pumping process (Figure 3.7, left). In parallel, the effect of pressure application is investigated in a pressure measuring cell (Figure 3.7, right).

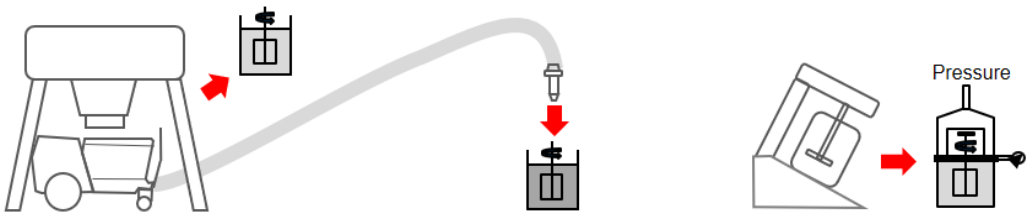

FIGURE 3.7: Determining rheology before and after pumping (left) as well as during pressure application after mixing in a laboratory mixer (right)

3.6.2 Dynamic rheological measurements

For the **dynamic measurements** (meso scale), the speed of rotation v_r and the torque M are determined on a rheometer. The rheological parameters yield stress τ_0 and shear rate $\dot{\gamma}$ are then calculated from these measured parameters using conversion factors taking into account the geometry of the measuring system (see below). The rheological parameters are approximated on basis of the calculated flow curve. For linear flow curves, the evaluation according to Bingham represents a sufficiently accurate regression model: $\tau = \tau_{0,B} + \mu_B \cdot \dot{\gamma}$ with dynamic yield stress $\tau_{0,B}$, plastic viscosity μ_B and shear rate $\dot{\gamma}$. However, for shear-thinning and shear-thickening materials, the Bingham model over- and underestimates the yield stress τ_0.

The Herschel-Bulkley model is an exponantial approximation of the experimental flow curve:

$$\tau = \tau_{0,HB} + k\dot{\gamma}^n \tag{3.1}$$

with flow coefficient k and flow index n. It can be used to approximate shear rate dependent materials. For $n > 1$ the material is shear thickening, for $n < 1$ shear thinning and for $n = 1$ it corresponds to the Bingham model with $k = \mu_B$.

For pumpability, the rheological parameters of the material while flowing are most relevant. As the material is continuously in movement, reversible structure is broken and the material is in a transient state. Therefore, dynamic measurements are conducted for data consistency at least three times with every material. To this end, a rotational rheometer (Viskomat NT) with a vane-in-cup measuring device is used. The vane paddle is four-bladed and has a height of 29 mm and a radius of 9 mm. The cup has a radius of 32.5 mm.

For all mixtures the mixing and absorption water has a temperature of approximately 8 °C. The resulting temperature of the lightweight aggregate concrete is measured directly after mixing and at beginning of the rheological tests as the temperature significantly influences the rheological parameters. If it deviates more than 5 °C from the desired temperature of 20 °C, the mixture is discarded and repeated with adapted water temperature.

As there is a significant change in rheological properties during the first 15 minutes after water addition followed by a more stable phase, the measurement starts 15 minutes after water addition with the descending steps. Furthermore, previously built-up structure must be destroyed before starting measurements. In order to achieve this, sufficient shear rate has to be applied in order to reach a “fully rejuvenated” state (Wallevik and Wallevik, 2017). In order to avoid large breaking

of the structure during the rheological measurements and the corresponding influence of the results, the material is homogenized for 1 minute with the mixer before filling the material into the cup for the rheological measurements.

The test begins by moving the vane measuring device attached to the rheometer downwards into the cup filled with material until the coverage of the vane device at the top is as large as the distance of the device to the bottom of the cup. The measurement starts when the cup begins to rotate. In the beginning, a pre-shear of 80 rpm is applied to break the structure which builds-up while mounting the cup in the rheometer (structural break-down, see Figure 3.8). As the Viskomat NT is not able to increase the rotational speed from 0 rpm to 80 rpm in a second, the speed is increased to 40 rpm and then further.

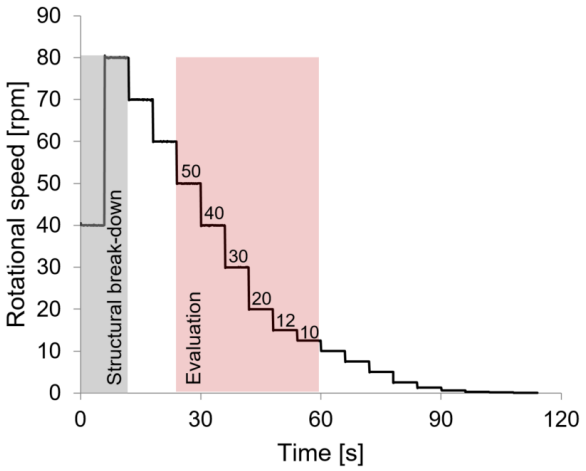

FIGURE 3.8: Dynamic measuring profile with descending rotational speed steps over time including shear for structural break-down and area for the yield stress evaluation

The torque values are measured in eighteen descending rotational speed steps from 80 rpm to 0.08 rpm with 6 seconds each and one second slowing-down between the steps, see Figure 3.8. At each step the time for slowing down and speeding up is considered. Preliminary tests showed that with this profile an equilibrium (i.e. an approximately constant value of the shear stress) in the steps between 50 rpm and 10 rpm could be achieved in all measured lightweight concretes. The timing for the measurements is presented in Table 3.5. It starts after the mixing which is described in Table 3.4. The (cumulative) test time starts at the addition of the mixing water.

In order to determine the dynamic yield stress $\tau_{0,D}$ of the mixture, an evaluation according to the Herschel-Bulkley approach is conducted. To this end, the equilibrium torque value of the speed steps 50 rpm, 40 rpm, 30 rpm, 20 rpm, 15 rpm, 12.5 rpm and 10 rpm are used. The other steps are neglected for the evaluation as they might be influenced by structural break-down or

TABLE 3.5
Timing of dynamic measurements after addition of mixing water

This table describes the temporal sequence of the tests after the mixing procedure. The timeline refers to the addition of the mixing water.

	Timeline [min : s]	Duration [min : s]
Mixing process	0:00	see Table 3.4
Temperature measurement	2:30	0:30
Filling of the conus for slump test	3:00	1:30
Slump test	4:30	1:30
Cleaning of test equipment and preparation	6:00	5:00
Homogenization (mixing)	11:00	1:00
Filling of the cup of the rheometer	12:00	1:00
Mounting of the cup in the rheometer and activation	13:00	1:33
Temperature measurement in parallel	14:00	0:30
Pre-shear	14:33	0:27
Beginning of descending steps	15:00	1:52
End of dynamic measurements	16:52	-

structural build-up for some mixtures which biases the equilibrium values. Furthermore, the first and the last second of every speed step is neglected for the average value as it might be influenced by the change of the rotational speed. The average value M_j thus corresponds to 4 seconds for each speed step. The (inner) shear stress $\tau(\dot{\gamma}_j)$ is calculated by dividing the torque M_j by the surface area of the sheared cylinder:

$$\tau(\dot{\gamma}_j) = \frac{M_j}{2\pi \cdot h_v \cdot r_v^2} \tag{3.2}$$

with the height h_v and radius r_v of the vane measuring device (Krieger, 1968).

The shear rate is calculated according to the second Krieger approach assuming plug flow

$$\dot{\gamma}_j = \frac{2 \cdot \Omega_j}{m\left(1 - (\frac{r_{cup}}{r_v})^{-2/m}\right)} \tag{3.3}$$

with radius of the cup r_{cup} of the vane-in-cup system and $m = \frac{dln(\tau_b)}{dln(\Omega)}$ (Krieger, 1968). Thus, m is calculated over the linear gradient of the natural logarithm function of the inner shear stress over the natural logarithm function of the rotational speed for the speed steps considered (Krieger, 1968; Koehler and Fowler, 2004). The rotational speed $v_{r,j}$ is converted into radian measure for each speed step by $\Omega_j = v_{r,j} \cdot \frac{2\pi}{60}$. After conversion of the measured values into shear rate $\dot{\gamma}$ according to equation (3.3) and shear stress τ according to equation (3.2), the Herschel-Bulkley model is fitted to the values following a minimum mean square error approach by iteratively

adjusting the parameters $\tau_{0,HB}$, k and n in equation (3.1) . Each test is repeated at least three times and average values are built for the yield stress τ_0.

3.6.3 Rheology and density in pumping tests

Pumping tests (macro and meso scale) are conducted with the objective to analyze the changes of the material properties during the real process. The test setup and timing is summarized in Table A.3 in the appendix. Lightweight aggregate concrete is prepared and mixed as described in Table 3.4. As large amounts of material are needed in order to record values at varying pumping speed and time, 40 l to 60 l are prepared in a compulsory mixer.

The lightweight aggregate concrete is pumped in the actual 3D printer setting (see Section 3.4) with a progressive cavity mortar pump with a frequency controlled motor speed. Before every examination of the pumpability, the pump and hose are wetted with water and run through with a synthetic primer in order to ensure a uniform lubrication of the wall. The first material which might have been influenced by the primer is discarded. The mortar pump is always activated at a frequency of 7.3 Hz and during the procedure the pumping speed is step-wise increased to 15.6 Hz and 26.2 Hz. The range of frequency is chosen in accordance with the frequencies applied in extrusion. The required pumping speed depends on the velocity of the manipulator (related to the movement of the nozzle) depending on the geometry of the object, its contour length and the vertical building rate.

For the macro scale, the flow rate Q, which corresponds to the mass per minute leaving the hose, is measured three times for each frequency (7.3 Hz, 15.6 Hz and 26.2 Hz). The mean values of the flow rates for each pumping speed are used for further evaluation and comparison. Furthermore, the density of the fresh lightweight aggregate concrete is determined before pumping and for each pumping speed according to EN 1015-6. The change in temperature of the fresh lightweight aggregate concrete before to after pumping is recorded. Furthermore, material pumped at different velocities and material without pumping is used to produce mould prisms.

Pumpability is not a physically well defined and measurable parameter, but entails multiple rheological components (Abebe, 2017; Secrieru, 2018). In the thesis at hand, the pumpability is only evaluated in comparison to mixtures with a different pre-saturation time with the same process and conveying. The pumpability in this setting is evaluated in a pressure/flow rate diagram (P-Q-diagram). The slope of the curve determines the pumpability: Materials with a flatter curve are pumped more easily as less pressure arises for an equal flow rate.

The main focus lies on the changes of material characteristics during pumping (meso scale). First of all, the temperature development and the change in density are taken into account. The temperature significantly influences the reaction of the concrete and the temperature after pumping is thus influencing buildability and layer bonding (see Section 2.3.2). The change in density is crucial in lightweight aggregate concrete extrusion since it affects not only the buildability but also the thermal conductivity of the material. Assuming that the change in density $\Delta\rho$ can be traced back to the water absorption of the lightweight aggregates, the effective w/b-ratio in the cement paste $(w/b)_{eff}$ can be estimated from the quotient of remaining water to binder, see equation (3.4).

$$(w/b)_{eff} = \frac{w_t - w_a}{C + LSP + Sf} \tag{3.4}$$

The absorbed water w_a includes water absorbed during the pre-saturation phase and during pumping. Looking only at the change induced during pumping, the change in water-to-binder-ratio $\Delta w/b_p$ can be estimated via equation (3.5).

$$\Delta w/b_p = \frac{\frac{w_t}{b} - \frac{w_t - \Delta\rho}{b}}{\frac{w_t}{b}} \tag{3.5}$$

The associated change in pore filling Φ_{fill} of the lightweight aggregates can be determined via equation (3.6).

$$\Phi_{fill} = \frac{\Delta\rho}{\Phi} \tag{3.6}$$

With regard to pumpability, the change in w/b-ratio in the cement paste due to water absorption of the lightweight aggregates might also be accompanied by a reduction of the lubrication layer and thus deteriorate pumpability and increase the probability of blockages (macro scale).

The pump tests are also connected to further tests, which depend on evaluation before and after pumping. In this context, the rheology of the lightweight aggregate concrete and the condition of the lightweight aggregates is evaluated. For the evaluation of rheology see Section 3.6.2 (dynamic measurements) and Section 3.7.1 (static measurements). The mean rheological properties before and after pumping are compared on a meso scale. The methodology applied for the lightweight aggregates (micro scale) was described in Section 3.5.

3.6.4 Effect of pressure application on rheology

Using a pressure cell with a vane-in-cup measuring system, the change in rheology can be determined at varying pressure. The pressure cell ST24/PR/2W-A1 by Anton Paar (see Figure 3.9) is used in combination with the rheometer MCR 702 by Anton Paar. The pressure cell consists of a cup with a radius of 18 mm, a top cover with bearing for the vane device on the inside and on the outside a magnetic connection to the axis attached to the top of the rheometer. The four-bladed vane device has a radius of 5 mm and a length of 39.5 mm. The maximum pressure allowed is 150 bar and the torque ranges from 100 μNm to 150 mNm according to the manufacturer.

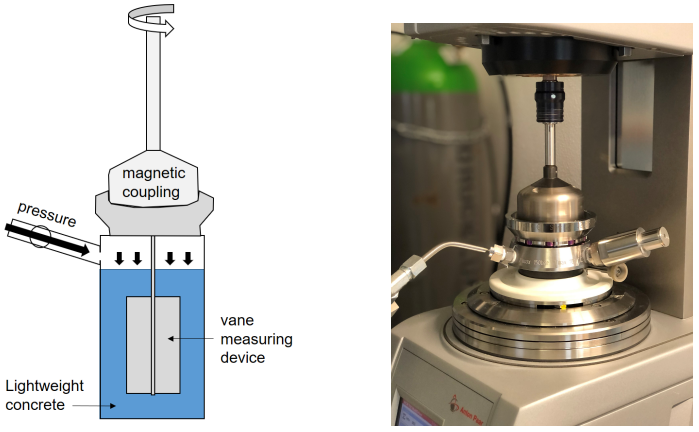

FIGURE 3.9: Operating principle (left) and picture (right) of the pressure cell in Anton Paar rheometer

Two test regimes are developed to evaluate the influence of pressure on the rheology of lightweight aggregate concrete. In order to avoid side effects, the shear rate is kept constant throughout the pressure increase experiments. For the first test regime, the pressure increases by 2 bar every 5 minutes in order for the material to reach a steady state at every pressure level. The timing is summarized in Table A.4 in the appendix. The development of the torque over time is directly compared to other mixtures in order to determine how, e.g., different grain size fractions affect the material properties at increasing pressure. In order to exclude temporal effects, a test of the same duration without pressure increase is also performed.

The measurements are supplemented by a determination of the rheology in dynamic rotational measurements on material which was exposed to the pressure followed directly by the same measurements on the material without pressurization (see Table A.4 in the appendix). Thereby, yield stress of the material can directly be compared for an equivalent material age. The evaluation is done according to Section 3.6.2, taking into account the different geometry of the vane-in-cup system.

It should be noted that after the pressure is removed, some of the absorbed water can be released again. This might lead to a change in the rheological characteristics of the material. However, this is also the case in the real situation during extrusion as soon as the material exits the nozzle.

For the second test regime, the so-called "static pressure tests", the pressure is increased for a few seconds to different levels. Two minutes after measurement start, the pressure is increased for 30 seconds and the peak torque is measured followed by a removal of the pressure. This procedure is conducted for pressure levels of 3 bar, 5 bar, 7 bar, 9 bar, and 11 bar, at least twice each. The timeline is summarized in Table A.5 in the appendix.

The shear stress per pressure level $\tau_j(P)$ is calculated dividing the peak torque values for each pressure level M(P) by the surface area of the corresponding sheared material cylinder:

$$\tau_j(P) = \frac{M(P)}{2\pi \cdot h_v \cdot r_v^2}.$$

Thus, the evolution of the shear stress over pressure can be evaluated. The timing until the start of the measurements is the same as before. At 16 minutes after water addition, the rheometer is activated and at 16:52 the pre-shear starts. The test procedure is based on the measurements of the static yield stress (Section 3.7), except that it is not internal structural build-up at rest that is tested, but externally induced structuration due to pressure. The peak values are complemented by the peak for the first pressure increase in the first test method (see Table A.4).

3.7 Investigations for buildability assessment

3.7.1 Static measurements with the rheometer

The buildability is mainly influenced by the initial static yield stress and the evolution of the static yield stress over time as they determine the green strength in the layers (see Section 2.3.2). The yield stress is therefore evaluated on a meso scale in rheological measurements over a time span of 30 minutes. To this end, a lightweight aggregate concrete is produced as described in Section 3.1. Note that the yield stress is not a material constant, but dependent on the measuring device and can only be approximated using model functions (Mezger, 2016).

The investigations on the static yield stress are conducted in the pressure cell of the rotational rheometer by Anton Paar (MCR 702) with a vane-in-cup measuring device (without applying pressure). The vane paddle is four-bladed and has a height of 39.5 mm and a radius of 5 mm. The

cup has a radius of 18 mm. Furthermore, to perform the rheological measurements in parallel with the pumping tests (before and after pumping), only the rheometer Viskomat NT with a four-bladed vane-in-cup measuring device was available. The vane paddle has a height of 29 mm and a radius of 9 mm. The cup has a radius of 32.5 mm. Measurements are conducted for all materials before and after pumping with this rheometer and are only compared amongst each other. Note that if mixtures are too stiff, shearing-off around the vane-geometry, especially over longer time periods, occurs providing inconclusive results in the consequence. The tests and evaluation is kept the same for both rheometers.

In order to measure the structuration of the material, static measurements are conducted applying successive phases of shearing and resting on the material (see Figure 3.10) in order to analyze the evolution of the static yield stress over time. In the low or no-shear phases the material can build-up structure over a specific time (Roussel et al., 2012; Mezger, 2016). After certain time intervals, the static yield stress of the material is evaluated subjecting the material to a low shear of 0.15 rpm for 6 seconds, see Figure 3.10 (light grey lines). The shear was chosen just about large enough to evaluate the material resistance. Thus, periods of rest (30 s, 60 s, 120 s, etc.) and 6 s long periods of low shear take turns. Before the measurements start, a pre-shear of 85 seconds at 80 rpm is applied to break existing structure which will not be included in the evaluation. The detailed timing is listed in Table A.2 in the appendix. The timeline refers to the addition of the mixing water during the preparation of the lightweight aggregate concrete.

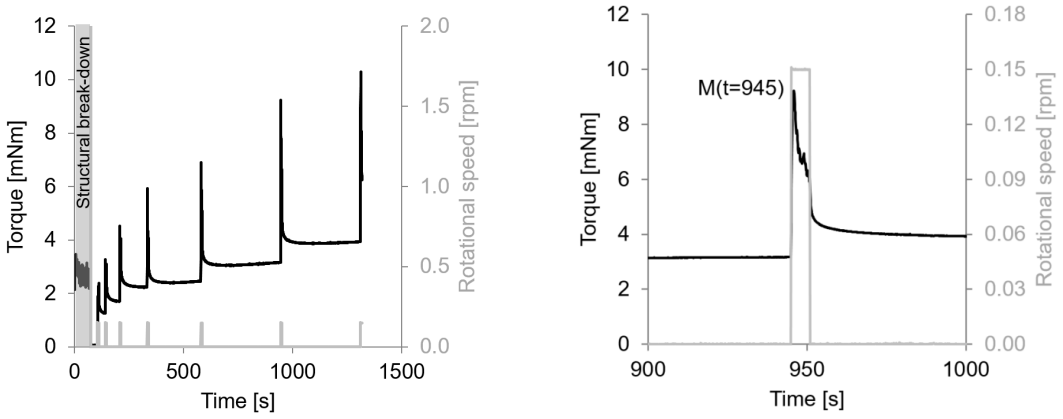

FIGURE 3.10: Static measuring profile–total profile (left) and focus on peak (right)

The peak torque values are recorded in the shear period. Care must be taken that the measured torque is already declining before the end of the 6 s shear period (see Figure 3.10, right). Otherwise, the maximum torque value is likely not yet reached and higher rotational speed is required. The maximum torque values $M(t_i)$ and their time of appearance are recorded whereby the start

of the resting time is set for time zero. The shear stress $\tau_S(t_i)$ at every time interval t_i is then calculated including the maximum torque value $M(t_i)$ and the geometry of the vane measuring device with height h_v and radius r_v. Thus,

$$\tau_S(t_i) = \frac{M(t_i)}{2\pi h_v r_v^2}.$$

The evolution over time can be depicted in a τ-t-diagram. The slope of the curve in the τ-t-diagram determines the structuration rate over time (see Figure 3.11). The structural build-up is supposed to be a combination of hydration processes and colloidal interactions (Roussel et al., 2012). The static yield stress $\tau_{0,S}$ corresponds to the shear stress at resting time 0 s.

In order to determine the evolution over time, different regression models are applied. The calculations are done both for a linear regression over time and a bi-linear regression. For the linear approach the equation $\tau = \tau_{0,S} + A_{thix} \cdot t$ is applied with static yield stress $\tau_{0,S}$ and structuration rate A_{thix}. For the bi-linear regression, an equivalent linear equation is set up both for the first 5 minutes (300 s) with re-flocculation rate R_{thix} (Kruger et al., 2019b) and for the time thereafter with structuration rate A_{thix}, see Figure 3.11 and equations (2.7) and (2.8).

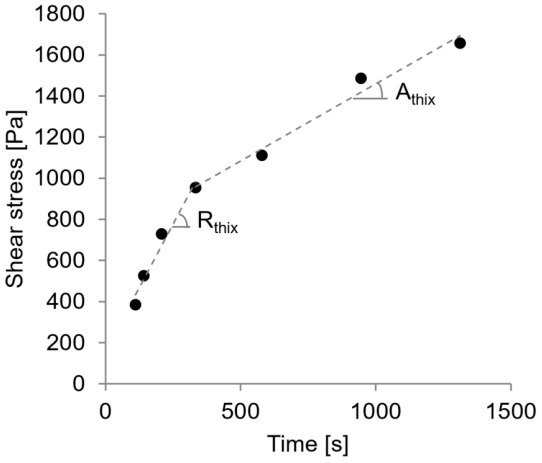

FIGURE 3.11: Structural build-up (increase in shear stress) over time with structuration rates R_{thix} and A_{thix}

3.7.2 Large-scale static yield stress tests

Material that is optimized for 3D printing can reach a static yield stress exceeding the capabilities of standard rheometers. Thus, a hand vane measuring device as well as an ICAR rheometer are used to supplement the data from the rheometer measuring the yield stress of the material after pumping over a time span of 2 hours. The timing of the test procedure is summarized

in Table A.7 in the appendix. The tests are done in parallel to the extrusion of lightweight aggregate concrete elements (Matthäus et al., 2021) and in parallel to the pumping tests, see Section 3.6.3.

The ICAR rheometer is a large-scale vane-in-cup rheometer. The four-bladed vane device has a height of 127 mm and a radius of 63.5 mm. The cup has a radius of 143 mm. For the tests with the ICAR rheometer, the pumped material is filled into the cup of the ICAR rheometer and the measuring device is positioned in the material and fixed on top of the cup. After a pre-shear for 10 s, the material is left at rest for 2 minutes and subsequently a small shear of 1.8 rpm is applied for 6 seconds in order to record the resistance of the material. After resting times of 8, 12, 20, 30, 45 and 60 minutes the resistance of the material to shear is recorded again applying a shear of 1.8 rpm. This allows to detect the evolution of structuration over time, see Section 3.7.1.

The hand vane measuring device follows the same principle, but is not controlled by an engine, but by hand turning it and measuring the resistance with a torque meter installed on top of the vane device, see Figure 3.12. The four-bladed vane device has a height of 50 mm and a radius of 16.5 mm. Again, static rheological measurements are conducted in a vane-in-cup system. To this end, buckets are filled with fresh lightweight concrete and 6 vane devices are positioned in the material. After resting times of 30, 60, 80, 90, 120 and 150 minutes shear is applied manually on the vane devices and the torque is recorded. For the hand vane device, measurements are taken at higher material age as higher levels of shear stress can be captured, and thus the material can be assessed over a longer period of time. Besides, measurements on fresh material are more susceptible to errors, e.g., due to wobbling when applying the stress manually.

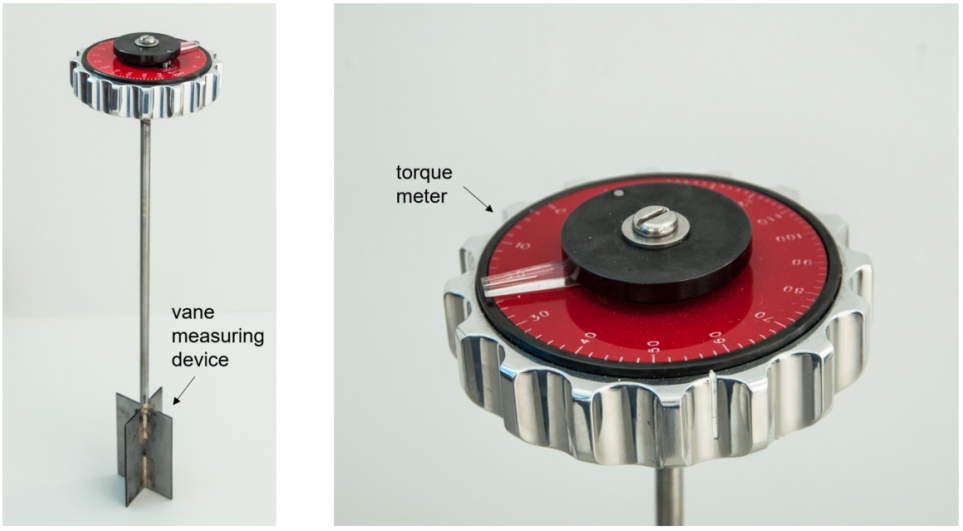

FIGURE 3.12: Hand vane measuring device

To increase data validity, for each time step 4 measurements with the ICAR-rheometer and 6 measurements with the hand vane on mixture M.PS 5min are combined in an average value. If a measurements can not be taken exactly at the same time, a linear interpolation between the two adjacent values of the same test series is performed.

The evaluation of the data of the ICAR rheometer is equivalent to that of the classical rheometer, see Section 3.7.1. The shear stress of the hand vane measuring device τ_h is calculated via equation (3.7) with the torque M_h measured by the hand vane and the volume of the vane geometry (radius r_v and height h_v) as well as a conversion constant.

$$\tau_h = \frac{M_h}{35.29 \cdot \pi \cdot 2r_v^2 \cdot h_v \cdot (1 + \frac{2r_v}{3 \cdot h_v})} \tag{3.7}$$

3.7.3 Compression tests

To establish a basis for buckling calculations, uniaxial compression tests are conducted on a meso scale to determine green strength and stiffness of the fresh material in accordance with ASTM D2166 (2017), Kränkel et al. (2010), Wolfs et al. (2018) and Suiker et al. (2020). For the measurements, tests samples are prepared for 5 different curing times: 10, 25, 40, 70 and 100 min after water addition (corresponding to 0, 15, 45, 60 and 90 minutes with respect to the beginning of the measurements). The fresh lightweight aggregate concrete is filled into the formworks and is compacted twice at a frequency of 30 Hz for 10 seconds.

Three supplementary tests are conducted on pressurized material: the material is pressurized before the production of test specimens. To this end, the material is filled into a cylindric formwork and put under mechanical pressure. The pressure corresponds to a high pressure during pumping (here 10 bar equal to 5 kN in the mechanical setup) to be able to evaluate the possible impact of pressure. The material is then carefully filled into the formwork without creating major air voids. These specimen are not compacted on a vibrating table in order not to disturb the effects induced by the pressure application.

Both, the normal samples and the pressurized samples are left to rest until two minutes before measurement start and only then demoulded and placed in the test setup. The timing for the compressive tests is summarized in Table A.8.

For the compression tests, cylinders with a diameter of 100 mm and a height of 200 mm are used. When placing the test specimen in the test setup a teflon sheet is placed between the concrete and the upper and lower plate respectively. The cylindrical specimen are loaded in

a displacement-controlled way with a rate of 30 mm/min. The force and the displacement is recorded during the measurement. The force is divided by the surface area of the specimen in order to determine the stress and the displacement is divided by the height of the specimen in order to determine the strain. The maximum green strength for every material age is identified which enables to compare the evolution of green strength over time. Furthermore, the Young's modulus is determined by the slope of the stress-strain-curve in the elastic region for every material age tested.

Static rheology measurements (see Section 3.7.1) accompany the compression tests. On the one hand, this serves to check that the fresh concrete production is reproducible, ensuring that deviations in the compression tests are not due to deviations in the mixtures. On the other hand, the rheological data can be used to supplement the investigations on the structural build-up of the material.

3.7.4 Buildability calculation and testing during full-scale extrusion

The buildability in terms of critical plastic failure time is calculated based on static rheological measurements, large-scale yield stress tests, and compression tests, see Section 3.7.1, Section 3.7.2, and Section 3.7.3. The failure occurs when stresses applied by the subsequent layers are higher than the strength of the lowest layers (Section 2.3.2).

The models described and developed in Section 2.3.2 are used to calculate plastic failure. In particular, a linear approach is used with equation (2.3), a bi-linear approach with equation (2.10) and a exponential approach with equation (2.6) to account for the development of shear stress in the lowest layers over time. In addition, the approach of Perrot et al. (2016) (equation (2.4)) is applied which is fitted to the real failure time and depends on the execution of experiments. The exponential approaches can not be solved analytically for the failure time. Thus, they are solved graphically determining the intersection of the strength in the second layer and the applied shear stress.

Based on the failure time, the amount of layers at failure a_f as well as the predicted failure height H_f is calculated, see Section 2.3.2. Furthermore, the minimum time per layer $\dot{l}$ (equation (2.11)) is determined which is an indicator for the maximum possible construction speed without failure.

For validation purposes on macro scale, a simple and uniform geometry is extruded with the setup described in Section 3.4. A critical building speed of 31 s/layer is applied. The failure time is compared to the calculated failure times.

Furthermore, the buckling is calculated based on the results determined by the compression tests in Section 3.7.3 using the calculation model by Suiker et al. (2020) presented in Section 2.3.2 (equations (2.14), (2.15) and (2.16)). The predicted buckling height $H_{f,b}$ is compared to the predicted height for a plastic collapse $H_{f,p}$. If $H_{f,b} < H_{f,p}$, the object is suspected to fail due to stability failure (elastic buckling). If both values are analytically smaller than 0 or higher than the desired geometry H_t, no failure is suspected to occur at all at the given process and material parameters.

3.8 Investigations on hardened concrete properties

3.8.1 Compressive and flexural strength

The strength of the hardened material on prisms produced before and after pumping are examined on a meso scale as described in Section 3.6.3. Three prisms are produced for each pumping speed (frequencies of 7.3 Hz, 15.6 Hz and 26.3 Hz) and for the material before pumping. The prisms are compacted for 45 s at 20 Hz. Without compaction, air voids would lead to high variance in measurements. In addition, prisms are sawn out of hardened extruded elements to assess the strength in the additively manufactured object. They are sawn-out of extruded elements horizontally and vertically (see Figure 3.13) to evaluate the effect of the production in layers without external compaction.

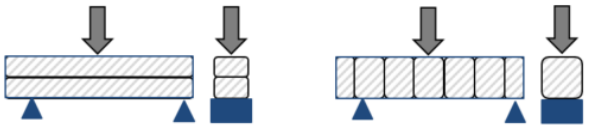

FIGURE 3.13: Test specimen for flexural and compressive strength taking the anisotropy of the material into account: Prisms sawn out horizontally (left) and vertically (right)

For all prisms, the flexural and compressive strengths are determined in accordance with EN 196-1:2016-11. Note that storage conditions differ slightly from the standard as the prisms are not stored in water, since extruded elements are not stored in a water bath on construction site and are subject to a certain amount of surface drying due to the absence of formwork. Instead,

the prisms are stored at laboratory conditions with $20 \pm 1\,°C$ and $65 \pm 5\,\%$ relative humidity for reproducibility.

3.8.2 Layer bonding

In order to determine the effect of layer bonding, the same geometry is produced with varying time gaps (2 min, 5 min and 10 min) between the deposition of the layers. The material is deposited in layers with rectangular cross-section. During deposition, the layer height is fixed to 10 mm by the robot and the material is slightly pressed into the antecedent layer. Each 3D-printed structure is sawn into 3 vertical and 3 horizontal prisms (see Figure 3.14). Again, prisms are stored at laboratory conditions with $20 \pm 1\,°C$ and $65 \pm 5\,\%$ relative humidity. After 7 days their flexural and compressive strengths are tested in accordance with EN 196-1:2016-11.

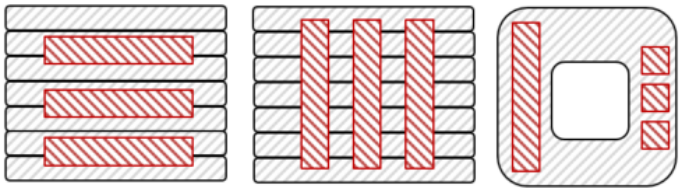

FIGURE 3.14: Test specimen for layer bonding properties – sawn out horizontally (left) and vertically (middle) in section and in top view (right)

3.8.3 Thermal conductivity measurements

The thermal conductivity of the lightweight aggregate concrete is determined using the Hot Disc method (transient plane heat source method) described in ISO 22007-2:2015-12. This is a dynamic measurement method which can be applied for materials with a thermal conductivity between 0.01 and 500 W/mK. A Hot Disk TPS 1500 by C3 Prozess- und Anaylsetechnik GmbH is used for the experiments.

For the tests, the sensor needs to sit between two specimens of the same material. For this purpose, the prisms produced during the pumping and extrusion tests are cut into two halfs. To prevent air gaps in the area of the sensor, it is checked that the halves can be placed on top of each other without an air gap. If necessary, the surfaces are ground. Subsequently, the sensor of the Hot Disk TPS 1500 measuring instrument is placed between the two specimens (see Figure 3.15, left) and fixed by applying a light load. A sensor with a radius of 6.4 mm (Kapton 5501) is used for the test and heat is applied at 50 mW to the specimens over a measurement

time of 80 s. The outflow of heat is recorded by the meter and the thermal conductivity λ of the material is calculated on this base:

$$\lambda = \frac{P_0}{\pi^{\frac{3}{2}} \cdot r_S \cdot \Delta T_s(\tau)} \cdot D(\tau)$$

with P_0 being the initial power, r_S the radius of the sensor, $D(\tau)$ a dimensionless specific time function and $\Delta T_s(\tau)$ the temperature increase on the surface of the specimen as described in ISO 22007-2:2015-12.

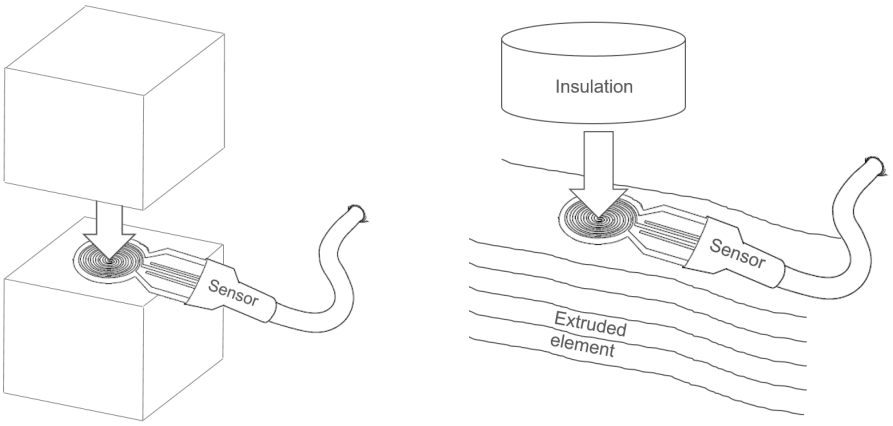

FIGURE 3.15: Setup of thermal conductivity measurement - standard (left) and single-sided on an extruded lightweight concrete element (right)

In parallel, the ambient temperature is detected via a temperature sensor in order to cover the influence of the environment. In addition, the age and moisture content of the test specimens must be taken into account. The specimens are therefore stored until testing at laboratory conditions with 20±1°C and 65±5 % relative humidity. Additionally, the thermal conductivity is measured on oven-dry specimen. Finally, to prepare a benchmark for practical applications, the measurement is also conducted single-sided on an extruded lightweight aggregate concrete element, using an insulating material with low thermal conductivity on top of the sensor (see Figure 3.15, right).

4 Experimental investigations on material characteristics in lightweight aggregate concrete extrusion

4.1 Results and discussion on changing material properties

4.1.1 Change of material properties during pumping

The lightweight aggregate concrete mixtures M.PS 5min and S.PS 5min and their variations (Section 3.3) are investigated during pumping. The longer pre-saturated mixtures are conducted once each with a three-fold repetition of the individual measurements, e.g., flow rate determination. For M.PS 5min more data is available as pressure and flow rate were also recorded in parallel to extrusion of lightweight concrete elements.

Figure 4.1 shows the density of test series M.PS 5min, S.PS 5min, and the variations M.PS 9d, S.PS 2d and S.PS 7d, which are pre-saturated for more than 1 day, before and after pumping as well as the percentage difference in density. Before pumping, the density of the mixture M.PS 5min is with 1160 $\frac{kg}{m^3}$ on average lower than after pumping with on average 1370 $\frac{kg}{m^3}$. This change in density is in line with literature, especially Hermann (1974) who also finds a change in density during pumping of lightweight aggregate concrete. The percentage change of the density lies in the order of 19 % for M.PS 5min and 16 % for S.PS 5min (see Figure 4.1). M.PS 5min contains a stabilizer and thixotropy enhancing agent while S.PS 5min does not.

In contrast to the described lightweight concrete mixtures, which were pre-saturated for 5 minutes, mixtures with longer pre-saturation time (2 to 9 days) show only a change of approx. 2-5 % during pumping, see Figure 4.1. The prolonged pre-saturation of the lightweight aggregates leads

to an increase in the density of the fresh concrete before pumping as the pores are filled to a greater extent with water, which has a higher density than air.

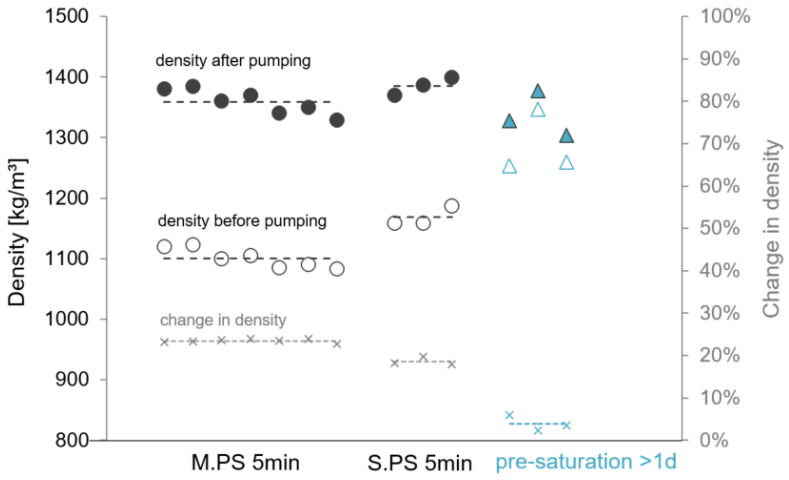

FIGURE 4.1: Mean fresh concrete density before and after pumping for different lightweight concrete mixtures and resulting change in density

Overall, for all of the lightweight aggregate concrete mixtures, a change in fresh concrete density during pumping can be observed. In Figure 4.2, the flow rates of test series M.PS 5min, M.PS 9d, S.PS 5min, S.PS 2d and S.PS 7d are depicted. The extent of the change depends on the flow rate and the pressure applied during pumping, see Figure 4.2. They in turn depend on the material composition, the pre-saturation of the lightweight aggregates and the pumping speed, which will be discussed in the following. The correlation coefficient between flow rate and change in density is -0.9 and between pressure and change in density 0.8—both statistically significant.

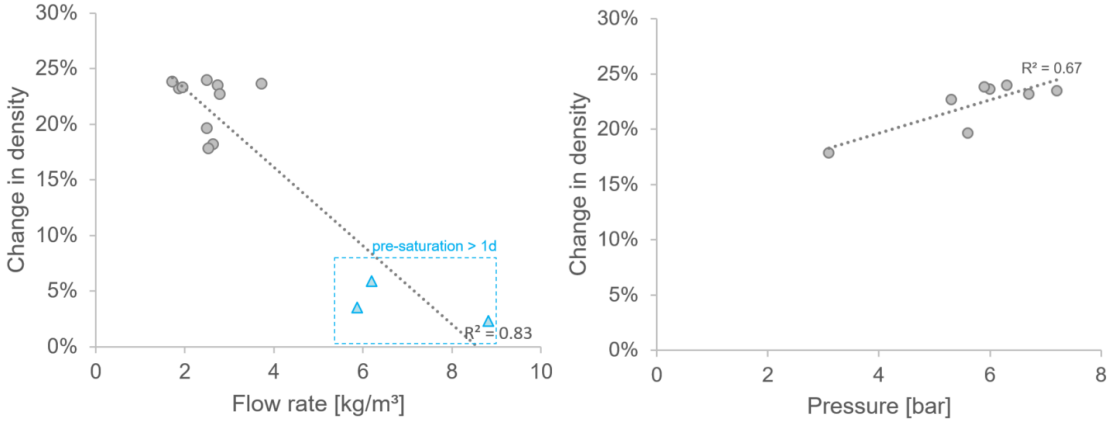

FIGURE 4.2: Change in density during pumping of lightweight aggregate concrete over flow rate (left) and pressure (right) for mixtures with standard pre-saturation of 5 minutes

As depicted in Figure 4.2, the change in density generally increases with higher pressure. The increase in pressure apparently leads to a compaction of the lightweight aggregate concrete, which might be caused by compression of the air in the pores of the lightweight aggregates combined with absorption of water or cement paste. Another aspect could be a change in the packing density, e.g. due to partly destruction of the lightweight aggregates as well as shifts in the amount of fine grains in the cement paste due to filling of the lightweight aggregates under pressure. A third option would be that the air void content in the matrix changes. The air void content for the examined mixtures in this work lies at approx. 14.5 vol.%. Thus, the change in density is supposed to happen due to water or cement paste absorption of the lightweight aggregates as well as partial destruction and will be analyzed on a micro scale.

According to literature, the absorption of water increases with increasing pressure (Hermann, 1974; Rossig, 1974). Calculating the approximate water absorption during pumping on basis of the differences in density before and after pumping, reveals an increase in the amount of absorbed water with increasing pressure. Also, a correlation between the change of pore filling during pumping (calculated according to equation (3.6)) and the pump induced change in w/b-ratio ($\Delta w/b_p$ calculated according to equation (3.5)) with the change in density with correlation coefficients of 0.99 each was found. Figure 4.3 shows the values for mixtures with both, standard pre-saturation of five minutes and longer pre-saturation of 2-9 days.

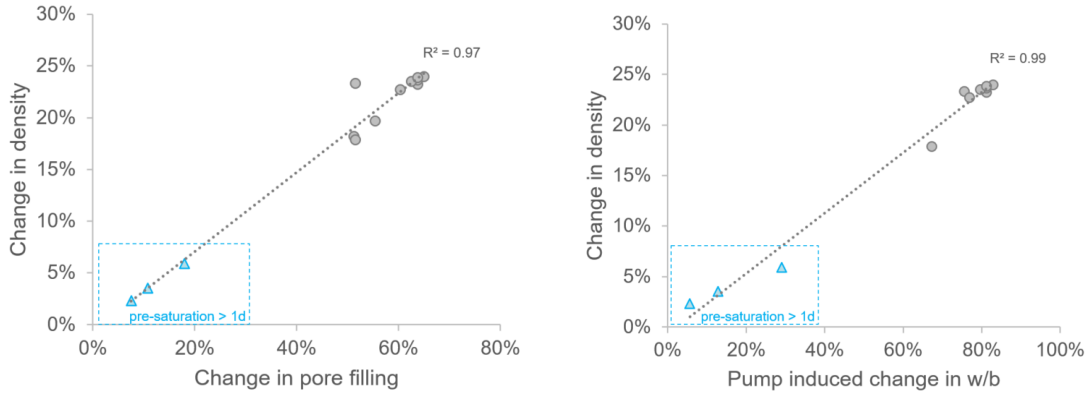

FIGURE 4.3: Change in density over pore filling and water-binder-ratio during pumping

As with increasing pressure the water absorption increases, less water remains for the lubrication effect. The pump induced change in w/b-ratio of M.PS 5min is approx. 80 %. In contrast, for mixture M.PS 9d, where the aggregates were pre-saturated over 9 days, it changes only by 13 % during pumping. The pump induced change in w/b-ratio of the mixture S.PS 5min is approx. 65 %. The pre-saturated mixtures, however, change only by 30 % for S.PS 2d and 6 %

for S.PS 7d in w/b-ratio during pumping. However, the mixtures with a pre-saturation time longer than 5 minutes absorb significantly more water already before pumping. Including this water in the calculation of the effective w/b-ratio in the cement paste, the differences are not as large. Table 4.1 gives an overview of the calculated total water absorption according to equation (2.18) based on the density after pumping and the individual components of the mixture as well as of the effective w/b-ratio, which is calculated according to equation (3.4) assuming that the absorbed water is not accessible to the cement.

Note that the water absorption and pore filling is higher and the effective w/b-ratio is lower for the mixtures M.PS 5min and S.PS 5min as for the equivalent longer pre-saturated mixtures. This is consistent with the clearly perceptible stiffening of the normal mixtures compared to the mixtures with longer pre-saturation.

TABLE 4.1
Effective w/b-ratio and pore-filling in lightweight concrete after pumping

This table gives an overview of the absorbed water according to equation (2.18) and the effective w/b-ratio in the cement paste according to equation (3.4). Furthermore, the filling of the pores of the lightweight aggregates is approximated comparing the absorbed water to the pore volume according to equation (3.6).

Mixture	M.PS 5min	M.PS 9d	S.PS 5min	S.PS 2d	S.PS 7d
Water absorption [wt.%]	41	31	49	37	40
Pore filling [vol.%]	32	24	38	29	31
Effective w/b-ratio [-]	0.3	0.42	0.25	0.38	0.57

The change in density results in changes of the hardened concrete properties, i.e. the compressive and flexural strength as well as the thermal conductivity of the material, and is thus important for the possible applications of the material, see Section 4.5. Furthermore, the change in density of the fresh concrete influences the buildability as discussed in Section 4.4.

The dynamic yield stress increases considerably during pumping (test setup as described in Section 3.6). This change in dynamic yield stress correlates with the change in effective water-to-binder ratio in the cement matrix which goes along with the increase in density (see Figure 4.4, correlation coefficient of 0.9). The correlation can be explained via the micro scale: when the lightweight aggregates absorb water and thus leading to an increase in density, the water available in the cement paste decreases at the same time and as a consequence the yield stress of the lightweight aggregate concrete. A comparable effect can be observed for the static yield stress: After pumping the static yield stress is considerably higher than before pumping. The increase in static yield stress during pumping, has a positive effect on the buildability and will be discussed in Section 4.4.

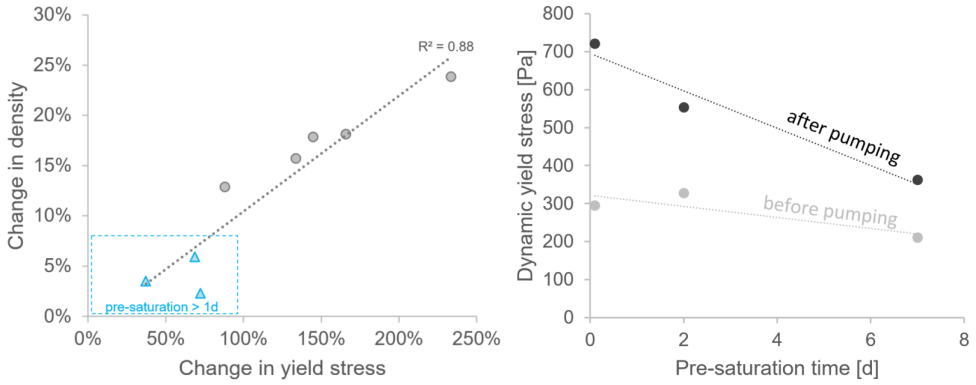

FIGURE 4.4: Change in density during pumping over change in yield stress during pumping for test series M.PS 5min, S.PS 5min and variations (left) and dynamic yield stress over pre-saturation time for test series S.PS 5min before and after pumping (right)

Looking at mixtures with different pre-saturation times, it was found that the change in dynamic yield stress decreases with increasing pre-saturation time (see Figure 4.4): For the test series S.PS 5min, the yield stress before pumping is almost independent of the pre-saturation time (277±50 Pa). However, after pumping, the yield stress of S.PS 5min (720 Pa) is clearly higher than of S.PS 2d (550 Pa) and S.PS 7d (360 Pa). Thus, for S.PS 5min it changes by 145 % from approx. 295 Pa to 720 Pa while for the longer pre-saturated mixtures the change ranges from 36 % to 70 %.

4.1.2 Change of water absorption under pressure

As elaborated in Section 4.1.1, the increase in density depends, besides others, on the pressure. This chapter focuses on the water absorption by lightweight aggregates on a micro scale, which is important to explain the physical background of the change in density. The water absorption of the individual grain fractions at ambient pressure is investigated and compared to the data provided by the manufacturer (Section 3.2). They are in line with the measurements conducted. Due to the lack of equipment to determine water absorption under pressure, the values on water absorption under pressure are provided by the manufacturer.

Figure 4.5 shows the water absorption of the individual grain size fractions at ambient pressure (left) and at 4.5 bar (right). Initially, the smaller grain size fractions absorb proportionally (to mass percentage) more water while after a few hours larger grain size fractions absorb more. Under pressure, the largest lightweight aggregates (of size 1-2 mm) clearly absorb the most water.

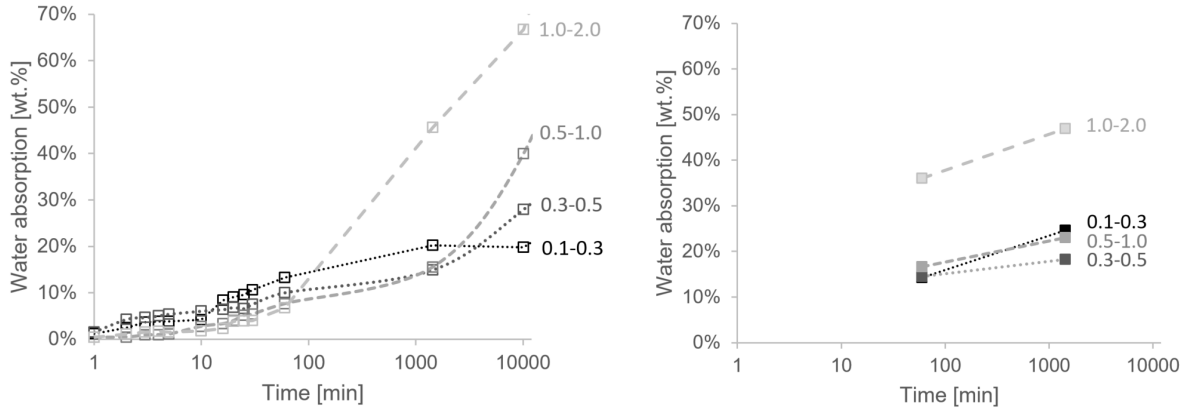

FIGURE 4.5: Water absorption in percent by mass of individual lightweight aggregate grain size fractions at ambient pressure (left) and exposed to pressure of 4.5 bar (right, provided by the manufacturer). Time is represented logarithmically.

Applying a pressure of 5 bar over 20 minutes on the lightweight aggregates the effects are even stronger and the water absorption is considerably higher than without pressure: The pressure of 5 bar over 20 minutes leads to a water absorption of approx. 61 wt.% for 1-2 mm, 34 wt.% for 0.5-1 mm, 20 wt.% for 0.25-0.5 mm and 15 wt.% for 0.1-0.3 mm (Figure 4.6). This is in line with Bauer and Poppy (1974) who state that after the same time aggregates exposed to pressure have a higher water absorption than aggregates at atmospheric pressure.

If water absorption is considered as a function of pressure (see Figure 4.6, left), it becomes clear that the smallest grain size of 0.1-0.3 mm is hardly dependent on pressure, while the dependence increases with increasing grain size. As the pore filling (ratio of water absorption to pore volume) of the grain size fractions is similar under pressure (Figure 4.6, right), but the size and amount of pores increases considerably with increasing grain size, the total water absorption increases for increasing grain size. At ambient pressure, however, the air in the voids provides a resistance to the intrusion of water. For larger pores, the capillary suction is lower.

The filling of pores starts with the smallest pore sizes progressing to larger pore sizes until it reaches the free water saturation. The maximum water content of a fine-pored building material corresponds to the complete filling of all cavities accessible to water. This maximum water content is usually not reached in the short term, i.e. within several days. Furthermore, expanded glass granulate is uniformly foamed leading to closed pores in the interior of the aggregate. Therefore, the pore filling is comparably low with lower than 30 vol.% even under pressure, see Figure 4.6 (right).

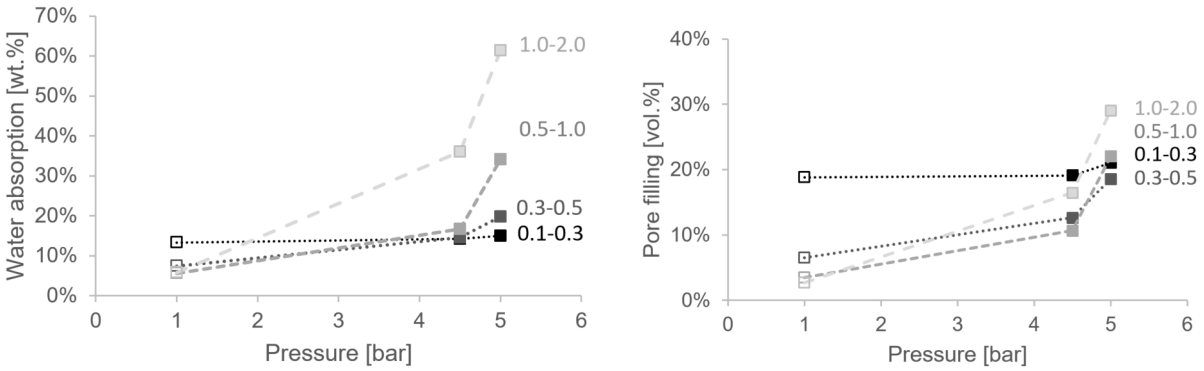

FIGURE 4.6: Water absorption (left) and pore filling (right) of lightweight aggregate grain size fractions in dependence of the pressure applied. Values under pressure provided by the manufacturer

Table 4.2 shows the values for water absorption at a pressure of 5 bar and the associated degree of pore filling. In addition, the total pore volume is given as the volume ratio between solid and air inside the aggregates, which corresponds to the maximum possible filling in vol.%. Thus, the pore volume limits the maximum water absorption. Finally, the maximum possible water absorption in percent by mass is listed which cannot be exceeded even at high pressure and long time spans and serves as a upper limit for the considerations. For an easier comparison to the water absorption shown in Figure 4.6 and Figure 4.7, the maximum water absorption is converted via the density from vol.% into wt.%. It can be clearly seen that the pore volume in vol.% is comparable for the different grain size fractions while the maximum water absorption in wt.% increases considerably with increasing grain size. However, as explained before and due to the fact that some pores are closed pores inside the lightweight aggregates, the maximum pore filling is not reached at the pressure and time spans considered.

TABLE 4.2
Water absorption of lightweight aggregates, amount of pores and pore filling

This table gives an approximation on the pore volume of individual grain size fractions, the water absorption and the pore filling.

Grain size fraction [mm]	Water absorption at 5 bar [vol.%]	Pore filling [vol.%]	Pore volume eq. max. water absorption [vol.%]	Max. water absorption [wt.%]
0.1-0.3	13.5	21	64	71
0.25-0.5	13.4	19	72	103
0.5-1.0	17.6	22	80	160
1.0-2.0	24.4	29	84	210

Moving from single grain sizes to the material mix, Figure 4.7 shows the water absorption of the grading curve used for the mixture M.PS 5min on top of single grain size fractions. Since the M.PS 5min grading curve is composed only of the four individual grain size fractions, it absorbs a

comparable amount at ambient pressure and it can be assumed that it also absorbs a comparable amount of water under pressure. The water absorption of mixture M.PS 5min corresponds to the maximum water absorption of the individual fractions. As the water absorption under pressure is similar to the water absorption after long periods of time, it can be assumed that the grain size fraction 1-2 mm is decisive for the water absorption of mixture M.PS 5min under pressure. Furthermore, the percentage share by volume of the grain size fraction 1-2 mm in the total quantity of lightweight aggregates is the highest (see Section 3.3) and thus represents a large proportion of the absorbable water. Overall, it is hypothesized that the 1-2 mm grain fraction has the major effect on the water absorption of the total grading curve.

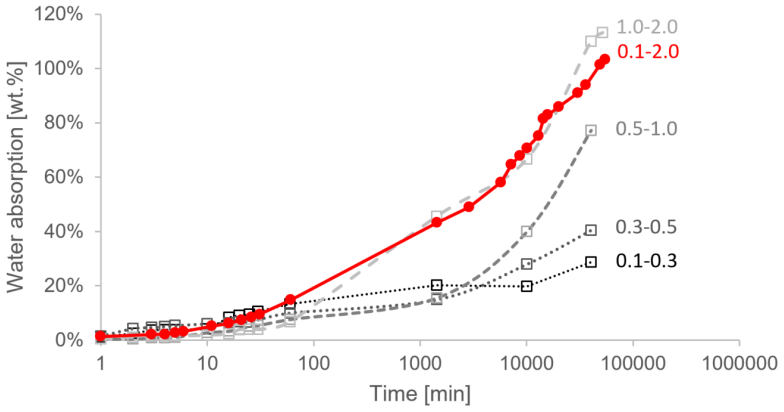

FIGURE 4.7: Water absorption of individual lightweight aggregate grain size fractions compared to grain size distribution in mixture M.PS 5min

4.1.3 Change of rheological properties under pressure

In order to investigate the effects of pressure separately from further parameters during pumping, rheological tests at varying pressure levels are developed, see Section 3.6 and conducted on a rheometer with a pressure cell. The tests are first carried out on the reference mixture M.PS 5min showing a clear change in torque in the moment of first pressure application, see exemplarily Figure 4.8. The torque increases up to 16 mNm which is 8 times higher than without pressure and then immediately drops to almost 0 mNm for all three repetitions. Without pressure, i.e. after the structural break-down, the torque stays almost the same over 30 minutes at a constant rotational speed of 40 rpm. Thus, it can be assumed that the changes observed in the pressurized lightweight concrete mixture are not due to aging of the material.

The increase in pressure coincides with the increased water absorption of the lightweight aggregates under pressure (see Section 4.1.2), which results in less water being available to the

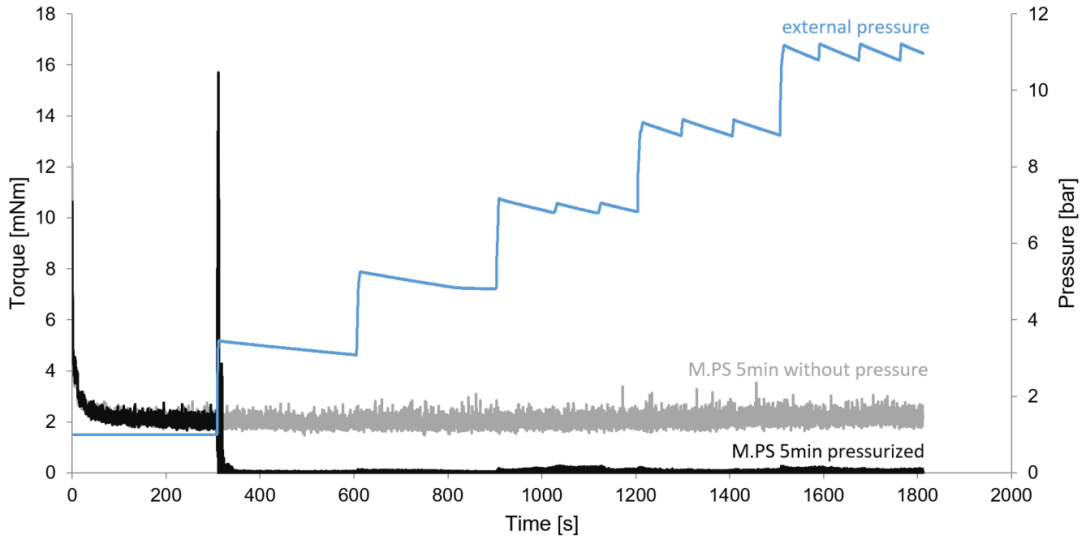

FIGURE 4.8: Change in torque during pressure increase for test series M.PS 5min

cement matrix. This in turn leads to a stiffer consistency of the material which is also clearly noticeable when the sample is removed after the test in comparison to an unloaded sample. The peak is an indicator for this stiffening. However, only the first pressure increase can be evaluated and not the evolution over different pressure values. The constant torque values close to zero suggest that the material becomes so stiff that a gap is sheared once and the material then stops moving towards the center. Thus, from this moment onwards measurements are only taken in the sheared gap, whereupon no further rheological evaluations can be made.

In order to be able to further quantify and analyze the changes during pressure application, the cement paste is combined with one grain size fraction only at a time (at constant volume ratio of 1:2 between lightweight aggregates (LA) and paste). At constant shear rate, the pressure is again increased every 5 minutes by 2 bar. Every experiment is conducted at least three times and mean values are formed. Figure 4.9 shows the resulting mean torque over time for the different grain size fractions. With every pressure increase the torque increases step-wise for the grain size fractions 0.1-0.3 mm (LA0.3 V1:2), 0.25-0.5 mm (LA0.5 V1:2) and 0.5-1.0 mm (LA1.0 V1:2) and the increase is stronger for larger grain size fractions (except for the grain size fraction 1-2 mm (LA2.0 V1:2), which will be discussed in the following). This is in line with the higher water absorption of the coarser aggregates under pressure (see Section 4.1.2).

In addition, it is also interesting to see that the torque in the mixtures with the smallest aggregates LA0.3 V1:2 hardly changes with the further increase in pressure. This can be attributed to the fact that open pores are quickly filled with the high surface area and no change in pore

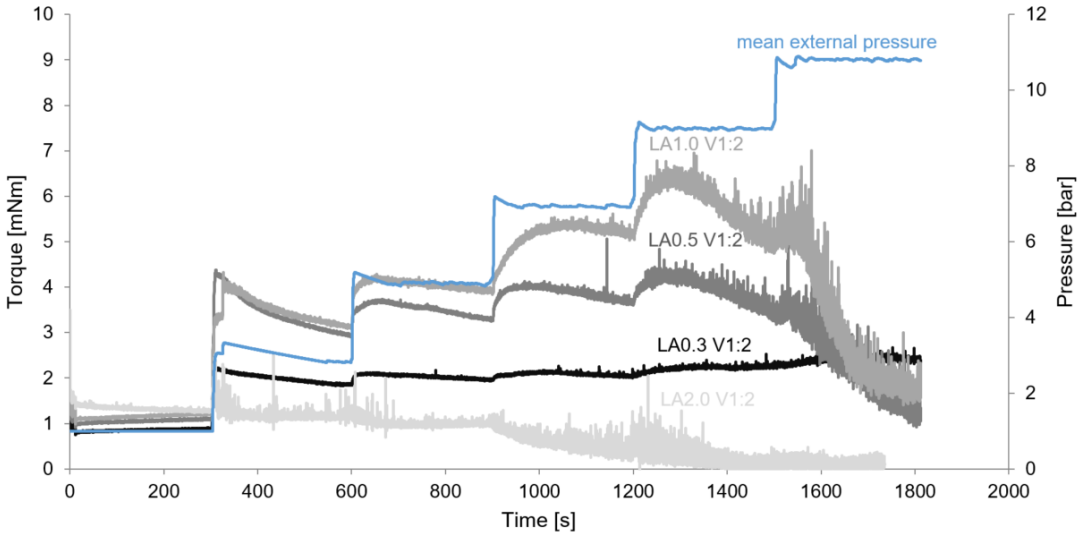

FIGURE 4.9: Change in torque during pressure increase for all grain size fractions

filling occurs with increasing pressure (see Figure 4.6, right). Furthermore, it should be noted that starting at a pressure of approx. 8 bar, the torque decreases for LA0.5 V1:2 and LA1.0 V1:2 (Figure 4.9). This can be traced back to the shearing-off effect described for mixture M.PS 5min.

For LA2.0 V1:2 at equivalent volume fraction, the shearing-off effect is observed already shortly after pressure application, see Figure 4.9. Thus, the torque cannot really be measured accurately, but rather artifacts during shearing-off are recorded. As the mean torque is not decreasing as quickly as for the shearing-off in the mixture M.PS 5min, further investigations are conducted. Reducing the amount of lightweight aggregates to a volume ratio of 1:4 to the cement paste (LA2.0 V1:4) and adjusting the pre-saturation water to a content which is calculated to be absorbed under a pressure of 4-5 bar (see Section 4.1.2), a step-wise increase of the torque with increasing pressure occurs, see Figure 4.10. The torque hardly increases with the first pressure application, but increases at higher pressure levels even at constant pressure. The increase during constant pressure stages indicates that the water cannot penetrate the pores immediately in some cases, but continues to penetrate over longer periods of time and a state of equilibrium has not yet been reached.

The water absorption experiments reveal that the lightweight aggregates of the grain size fraction 1-2 mm initially absorb significantly less water than the smaller grain size fractions and only show greater water absorption after some time. Furthermore, they absorb significantly more water under pressure when exposed for a longer period of time, see Section 4.1.2. This explains that the torque continues to increase at constant pressure. It is probably due to the accessibility

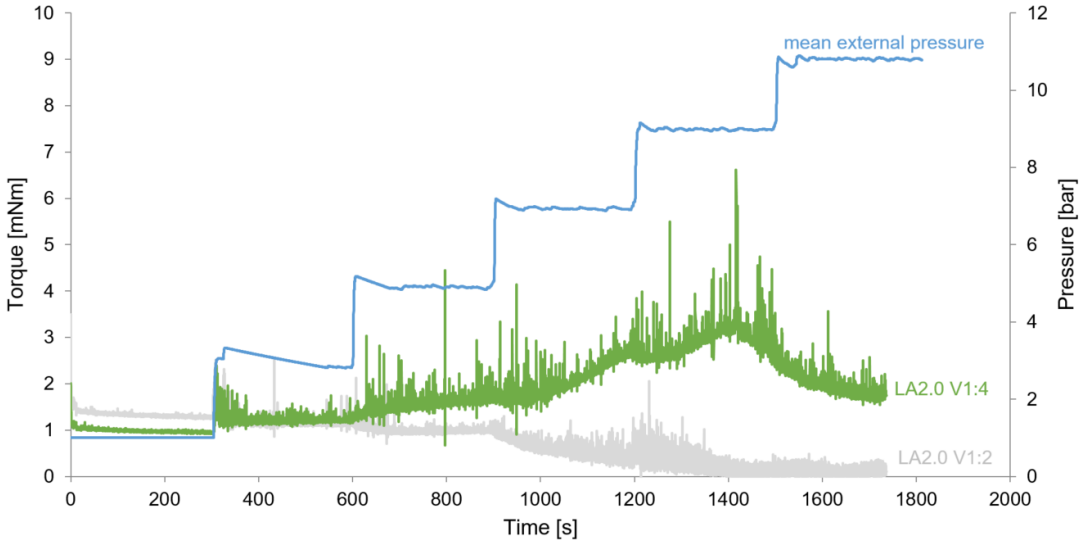

FIGURE 4.10: Change in torque during pressure increase for grain size fractions 1.0-2.0 mm with a volume ratio between lightweight aggregates and cement paste of 1:2 and 1:4

of the pores and the relatively smaller surface area of the grain size fraction 1-2 mm compared to the smaller grain size fractions. If no shearing-off would occur, with prolonged exposure, the torque of the mixture LA2.0 V1:2 would likely exceed that of the other mixtures. This supports the hypothesis that the grain size fraction 1-2 mm has the greatest influence on the behavior of the reference mixture M.PS 5min under pressure.

Directly after the test with the pressure increase (p), the material is analyzed in a dynamic rheological measurement. In addition, material that has not been subjected to pressure ($\bar{p}$), but remained in a bowl after mixing until the test, is characterized in dynamic rheological measurements directly afterwards in order to make changes due to pressure visible at the same material age. As can be seen in Figure 4.11, the pressure application (p) induces a clear difference to the torque curve. The torque is significantly higher for the pressurized material (p) than for the not pressurized ($\bar{p}$) at every shear rate.

Taking all grain size fractions into account, the change in the torque increases with increasing grain size. Calculating the dynamic yield stress, the same trend occurs, see Table 4.3.

The difference between the dynamic yield stress of material, which was not exposed to pressure, and pressurized material enlarges with increasing grain size. An increase in dynamic yield stress due to the pressure was found in all mixtures, however to varying degree (see Figure 4.12, left).

Furthermore, the change in dynamic yield stress increases with increasing grain size. For the largest grain size fraction (LA2.0 V1:2), the dynamic yield stress increases by 86 % due to the

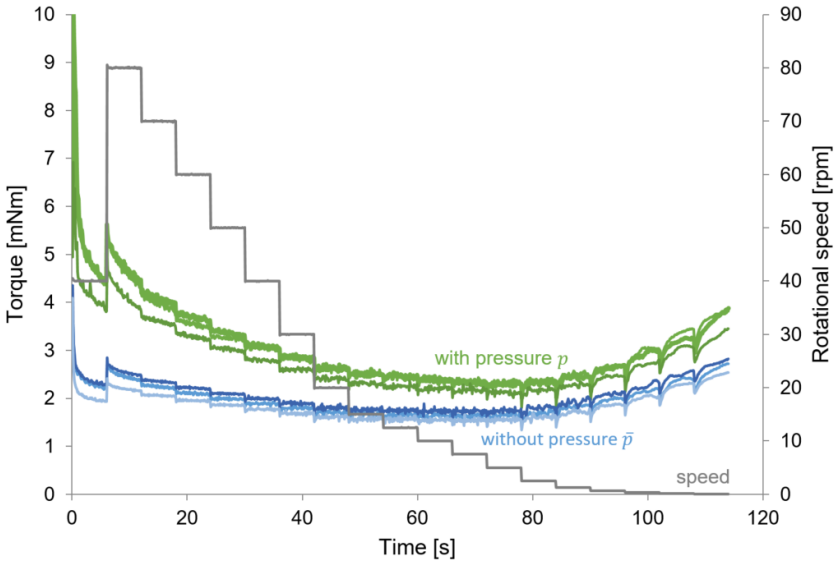

FIGURE 4.11: Dynamic rotational measurements on lightweight aggregate concrete with a grain size fraction of 0.1-0.3 mm (LA0.3 V1:2) with (p) and without pressure ($\bar{p}$) exposure for mixtures. Tests were conducted three times.

TABLE 4.3
Results of rheological measurements in pressure cell

This table provides an overview of the mean rheological properties of mixtures with (p) and without ($\bar{p}$) exposure to pressure. The changes in the concrete properties are evaluated by the difference (diff.) between both.

Mixture	Dynamic yield stress			
	$\bar{p}$ [Pa]	p [Pa]	diff. [Pa]	diff. [%]
LA0.3 V1:2	130	178	48	37
LA0.5 V1:2	154	234	80	52
LA1.0 V1:2	158	241	83	53
LA2.0 V1:2	143	266	123	86

pressure while for the smallest grain size fraction (LA0.3 V1:2), the dynamic yield stress increases only by 37 %. In Figure 4.12 the percentage increase in dynamic yield stress is depicted over the mean aggregate grain size of the investigated mixtures. For the individual grain size fractions, an almost linear increase with increasing grain size occurs (black spheres). The ratio of the volume of lightweight aggregates and cement paste is the same for all mixtures. Thus, the larger grain size fractions have a stronger effect on the changing rheological properties under pressure. This again fits with the observations made for water absorption (see Section 4.1.2).

In order to determine the static yield stress, the maximum torque at first pressure application is evaluated for different pressure values for mixture M.PS 5min. Each test is conducted three times. This newly developed test setup is comparable to a static rheological measurement, see

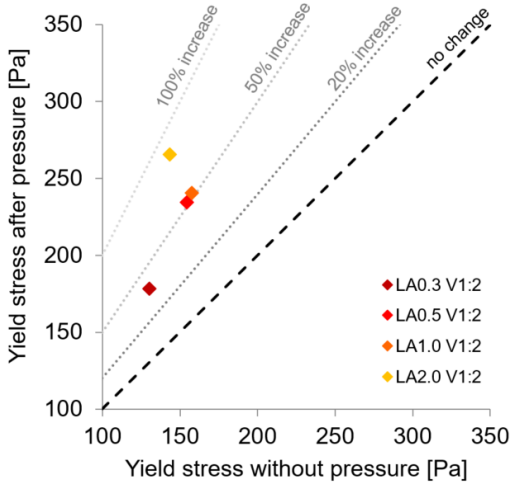

FIGURE 4.12: Increase in yield stress over grain size via comparison of yield stresses without ($\bar{p}$) and with pressure application (p)

Section 3.6.4. The torque is converted into shear stress. The results for static yield stress at varying pressure levels are summarized in Figure 4.13.

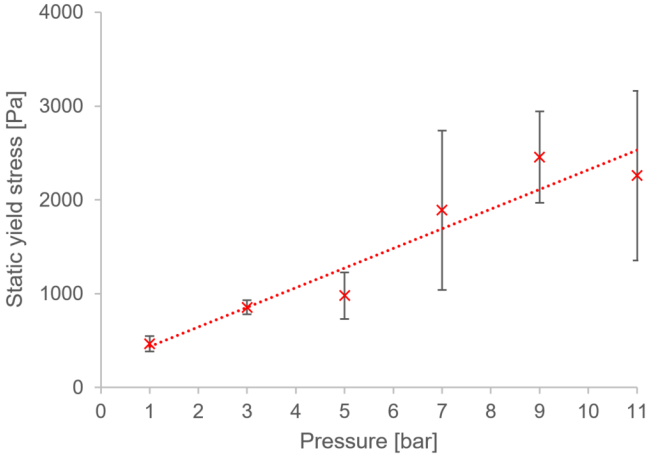

FIGURE 4.13: Shear stress in dependence of the pressure level for test series M.PS 5min

It was found that static yield stress increases linearly with pressure with a slope of $\dot{P} = 212\,[\mathrm{Pa/bar}]$ and a mean square error of $R^2 = 0.91$. The variance for the three repetitions increases in the range of high pressures due to the manual control of the pressure. Still, using this new approach, static yield stress at varying pressure levels can be determined also for materials which are stiffening during pressure application. This creates the possibility to consider the change in rheological properties due to pumping pressure when calculating buildability, see Section 4.4.

4.2 Implications on the lightweight aggregates

The lightweight aggregates and their change during the process are decisive for the changes in the concrete properties and performance. Therefore, the condition of the lightweight aggregates after the pumping process compared to the condition before the pumping process is investigated in more detail (micro scale). Before and after pumping at a frequency of 15.6 Hz, the lightweight aggregates are washed-out of 1 liter fresh lightweight concrete as explained in Section 3.6 using a sieve with 0.5 mm mesh width. The volume and the weight of the lightweight aggregates are determined and compared for the material before and after pumping. In order to compare the material adequately, the bulk density is determined as a ratio of weight over volume measured.

Over time, the lightweight aggregates release the absorbed water and start to dry. This leads to a drop in weight at constant volume. Thus, the bulk density decreases over time, see Figure 4.14. At every mixture, the lightweight aggregates have a higher bulk density after pumping than before pumping. The difference is more pronounced for the reference mixtures M.PS 5min and S.PS 5min than for the mixtures with longer pre-saturation times, see Figure 4.14.

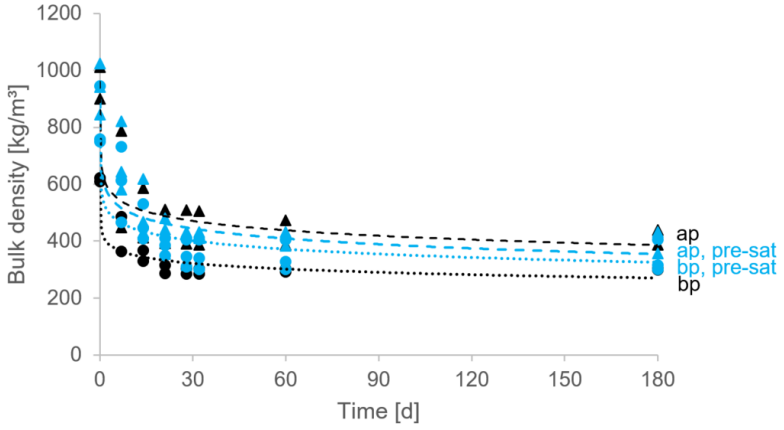

FIGURE 4.14: Effect of pre-saturation and pumping on the bulk density of lightweight aggregates for reference mixtures M.PS 5min and S.PS 5min (black symbols) and longer pre-saturated mixtures (pre-sat, blue symbols) before (bp, spheres) and after pumping (ap, triangles), exponential logarithmic fit

The evolution of the mean bulk density during drying can also be estimated with a logarithmic regression. The logarithmic equation overestimates the drying process in the first days, especially for the material which was pumped. The overestimation could be due to the fact that the water absorption is changed by the pumping process and that even cement particles might be partly pressed into the lightweight aggregates which slows the drying process down. This also fits in with the fact that the bulk density of the material before (bp) and after pumping (ap) settles to

different values after a long drying period, see Figure 4.14. The bulk density stays higher for the material after pumping than before pumping. For the longer pre-saturated mixtures, the effect is considerably smaller, which makes sense with regard to the pumpability and the fact that they are already highly saturated before pumping due to the long exposure to surrounding water. They are pumped more easily and at lower pressure (results will be discussed in Section 4.3).

The bulk density of the lightweight aggregates is also determined in oven-dry state. The results for fresh and oven-dry state are summarized for all considered mixtures in Figure 4.15.

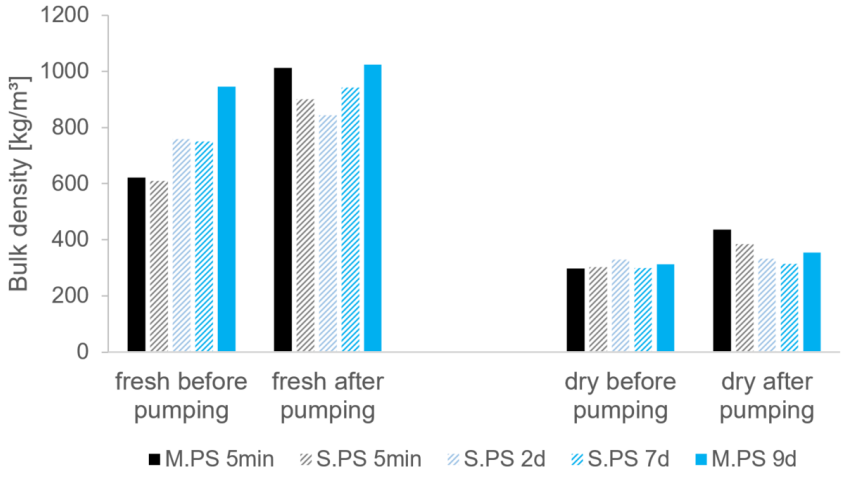

FIGURE 4.15: Bulk density of the lightweight aggregates in fresh and dry state before and after pumping

There is a clear difference in the bulk density in the fresh state (shortly after wash-out) and in the oven-dry state. In addition, it can clearly be seen that samples after pumping have a higher bulk density compared to samples before pumping. The increase from before pumping to after pumping is particularly noticeable in the normally pre-saturated samples M.PS 5min and S.PS 5min. For longer pre-saturated samples, the bulk density in the fresh state after pumping is already increased, which is due to the high preceding water absorption. Since the bulk density decreases significantly with drying, it can be assumed that the change in bulk density is primarily due to water absorption for all samples. However, the bulk density does not return to the same values for all samples as a result of the drying process, suggesting that some of the bulk density change is irreversible.

Figure 4.16 presents the absolute difference between the densities of the lightweight aggregates before and after pumping at fresh and oven-dry state. The difference is considerably higher for the reference samples M.PS 5min and S.PS 5min. At oven-dry state the longer pre-saturated samples have an almost equal density in the samples which were pumped and not pumped, e.g.,

difference of 1 % (3 $\frac{kg}{m^3}$) for S.PS 2d and 5 % (14 $\frac{kg}{m^3}$) for S.PS 7d. For M.PS 9d it is slightly higher with 13 % (40 $\frac{kg}{m^3}$). For the shorter pre-saturated samples, the difference in density decreases in the oven-dry state compared to the fresh state, but is still not to be neglected. For S.PS 5min the difference is at $\Delta\rho_{S.PS5min} = 83\,\frac{kg}{m^3}$, i.e., 27 % and for M.PS 5min the difference is at $\Delta\rho_{M.PS5min} = 139\,\frac{kg}{m^3}$, i.e., 47 %.

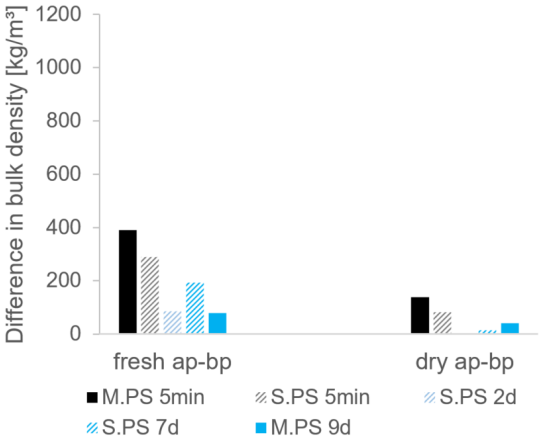

FIGURE 4.16: Effect of pre-saturation on the difference in bulk density of the lightweight aggregates before (bp) and after pumping (ap)

The differences in the bulk density of the lightweight aggregates after drying emerges from one or a mixture of the following two reasons: absorption or ingress of cement particles or cement paste into the lightweight aggregates as well as destruction of the skin of the lightweight aggregates under pressure or by the rotating elements of the pump. Since, in particular for sample S.PS 2d, virtually no change can be detected even though these samples are not completely saturated with water due to the 2 days of pre-saturation, it can be assumed that the difference is not primarily due to damage to the outer skin by the mechanical parts of the pump. However, damage to the outer skin due to increased friction between the lightweight aggregates at elevated pressure or between the lightweight aggregates and the stiffening cement paste (due to water absorption under pressure, see observations in Section 4.1.3) cannot be excluded. Furthermore, penetration of cement paste in mixtures subject to high pressures is probable.

To confirm this hypothesis, lightweight aggregates are inspected visually under the microscope after cutting them in half. To make the cement particles easier to recognize, colored pigments were added to the cement paste in the mixes so that the cement matrix can be distinguished from the lightweight aggregates. Figure 4.17 shows the difference between pumped and not pumped lightweight aggregates under the microscope. For the briefly pre-saturated mixture M.PS 5min, cement matrix can be detected even in the inner parts of the lightweight aggregates

after pumping, see brown elements in Figure 4.17 (right). The same phenomenon occurs for S.PS 5min.

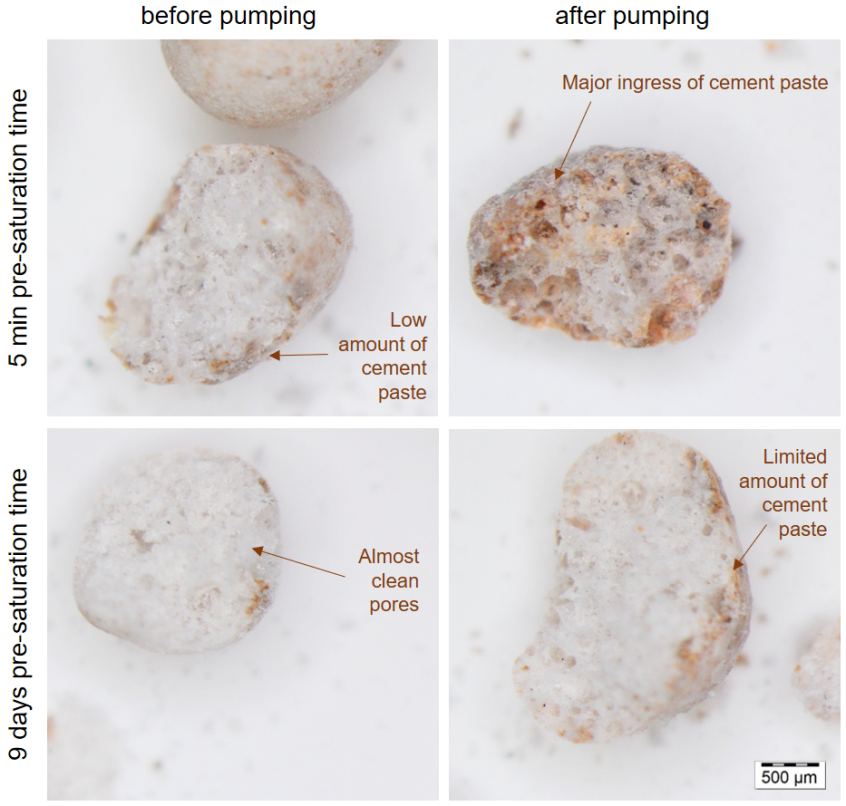

FIGURE 4.17: Ingress of cement paste into lightweight aggregates for mixtures M.PS 5min with 5 min or 9 days pre-saturation time respectively, each before and after pumping

For the longer pre-saturated samples M.PS 9d as well as for the samples before pumping of all mixtures, almost no cement particles can be detected in the inner part of the lightweight aggregates, but only in the outer area, see Figure 4.17 (upper left) and Figure 4.17 (bottom). The same phenomenon occurs for S.PS 2d and S.PS 7d. This means that with mixtures, which are pre-saturated for more than 1 day, there is significantly less or no ingress of cement paste into the pores of the lightweight aggregates under pressure.

Comparing the lightweight aggregates before and after pumping with different pre-saturation times in Figure 4.18, less differences in the appearance of the aggregates with increased pre-saturation time can be found. The surface of the lightweight aggregates of the reference mix S.PS 5min after pumping appears distinctly more porous. In some cases even pores lie open. This indicates that—in addition to ingress of cement paste—there is damage to the surface of the lightweight aggregates depending on the pressure or possible water absorption during pumping. This is in line with the investigations of Browne and Bamforth (1977) who show that

in "unsaturated" mixtures (see Section 2.3.1), high friction occurs between the aggregates. As the lubrication effect decreases due to the water absorption, mixtures M.PS 5min and S.PS 5min become "unsaturated" while in longer pre-saturated mixtures the direct contact of aggregates can be avoided.

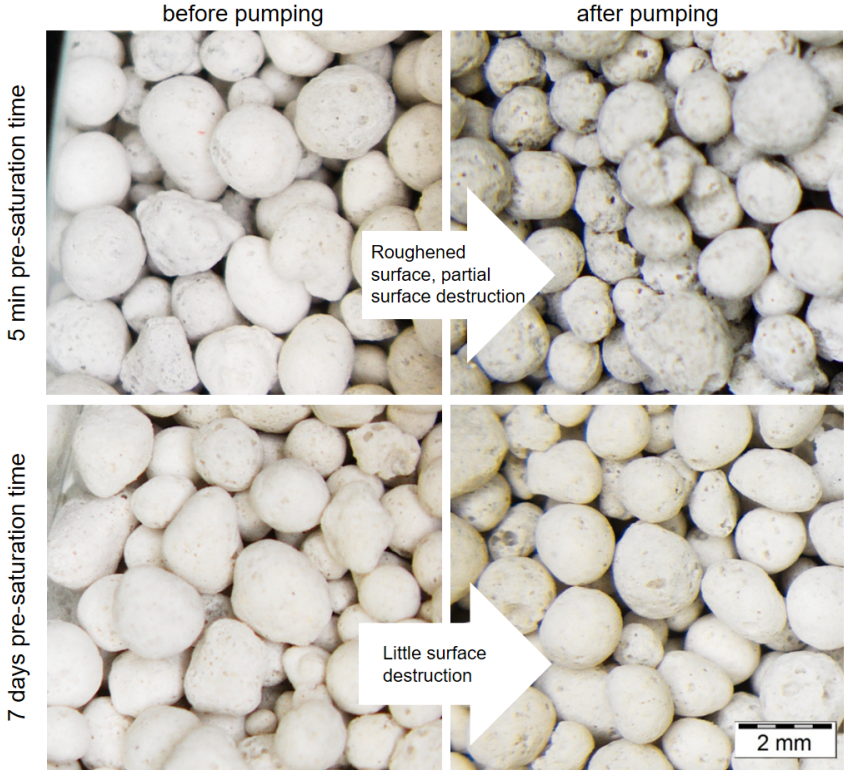

FIGURE 4.18: Comparison between washed-out aggregates: S.PS 5min (top) and S.PS 7d (bottom) each after pumping on the left and before pumping on the right

As shown, the lightweight aggregates underlie partly irreversible changes, which are investigated before and after pumping with regard to water absorption and density, see Table 4.4.

TABLE 4.4
Water absorption and density of lightweight aggregates before and after pumping

The water absorption of lightweight aggregates after (ap) and before pumping (bp) is determined with a pycnometer (see Section 3.5.2). Volume and density of 32 g lightweight aggregates are determined under water.

Mixture	Volume [ml]	Density $[\frac{kg}{m^3}]$	Water absorption after 1 d [vol.%]	Water absorption after 1 d [wt.%]
M.PS 5min bp	59	546	18	33
M.PS 5min ap	35	923	25	27
M.PS 9d bp	60	531	18	34
M.PS 9d ap	46	691	21	31

The results confirm the previous findings: For lightweight aggregates, that were not pumped (bp), density and water absorption are comparable independent of pre-saturation time. For pumped lightweight aggregates, density and water absorption decrease with increasing pre-saturation time. Furthermore, comparing the material after and before pumping, the pumping process affects density and water absorption. M.PS 5min after pumping has a considerably higher density than M.PS 5min before pumping. For M.PS 9d after pumping, there is also an increase compared to M.PS 9d before pumping, but not as much. The same is true for water absorption: Water absorption in vol.-% of M.PS 5min after pumping is approx. 37% higher than that of M.PS 5min before pumping. For M.PS 9d, the water absorption deviates still by 16 % between after and before pumping. This suggests that the surface destruction enables an easier water absorption after pumping.

In addition to the analysis of lightweight aggregates themselves, an analysis of lightweight aggregates in the cement matrix is also carried out, as described in Section 3.5.4, in order to exclude possible effects due to the wash-out of the lightweight aggregates. Also in the hardened concrete, the effects of cement paste penetration as well as the destruction of the surface can be observed. The cement is colored pink by phenophthalein to allow better visualization. Looking at the lightweight aggregates with a microscope (6-fold magnification), the penetration of paste into the pores can be seen in Figure 4.19.

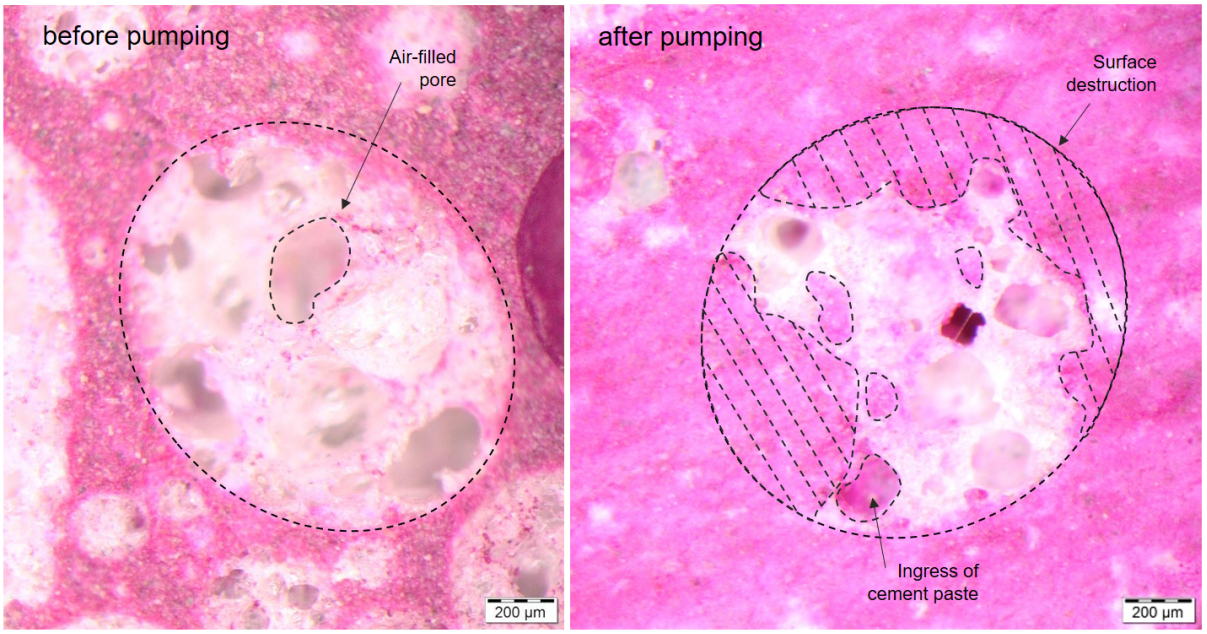

FIGURE 4.19: Close-up (6-fold magnification) on lightweight aggregates after pumping showing destruction and cement paste ingress into the aggregates

Furthermore, some aggregates loose their round shape during pumping which might be due to a destruction of the lightweight aggregates combined with cement paste intrusion, see Figure 4.19 (right). Figure 4.20 schematically depicts the changes happening in the lightweight aggregates during pumping: At increasing pump frequency the pressure increases (see Section 4.3), leading to an increased water absorption and an ingress of cement paste into the pores, especially in combination with surface destruction.

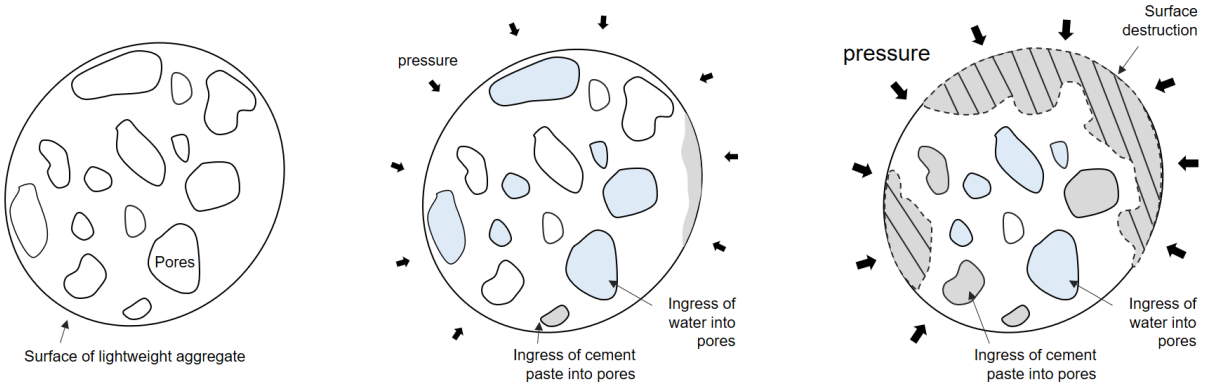

FIGURE 4.20: Schematically change in lightweight aggregates during pumping due to increasing pressure

The number of lightweight aggregates is counted for a given cross-section of the hardened lightweight concrete. To account for the variation caused by the 2D analysis of individual cut surfaces, deviations in the number of aggregates after pumping compared to the number before pumping smaller than 10 % are not taken into account (grey area in Figure 4.21). When comparing the number after pumping to the number before pumping, it can be seen that there is a significant reduction in all grain size fractions at S.PS 5min, see Figure 4.21. The change is particularly pronounced for the largest lightweight aggregates with a diameter of 1.0-2.0 mm. Furthermore, the change is higher for a larger pumping speed (26.2 Hz vs. 7.3 Hz).

For the pre-saturated mixtures, the change is visibly lower and partly even positive. The positive change might be due to the consideration of only individual cut surfaces (see Figure 3.6) and the detection of destroyed lightweight aggregates as smaller lightweight aggregates. For S.PS 7d the changes in number of aggregates can mainly be neglected: The deviations of the grain size fraction 0.1-0.25 mm equalize with the deviations for 0.25-0.3 mm (Figure 4.21) and are due to the procedurally separate analysis as the grain size fractions 0.1-0.3 mm and 0.25-0.5 mm overlap and an additional category had to be introduced for the counting.

In the case of pre-saturation over two days (S.PS 2d), however, the reduction of the largest aggregate size could be an indication that part of the lightweight aggregates is destroyed here

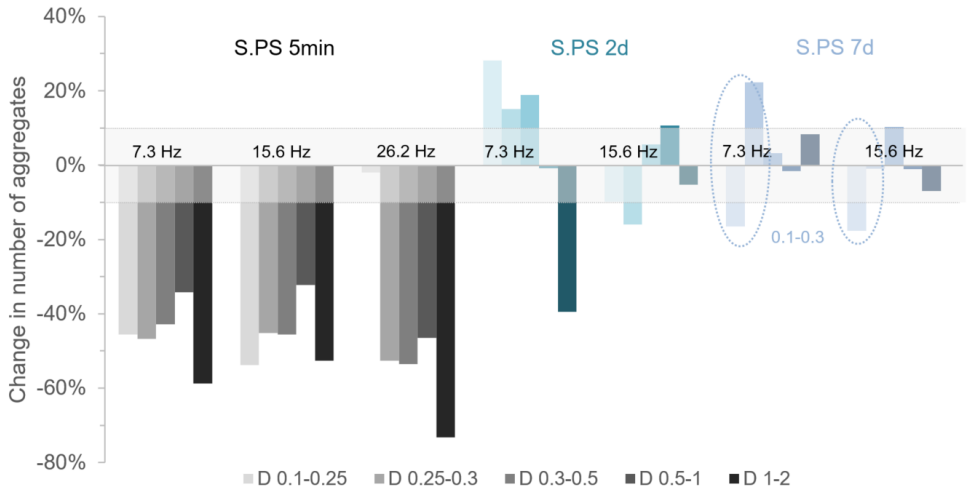

FIGURE 4.21: Percentage change in the amount of lightweight aggregates after pumping related to the amount before pumping for the grain size fractions 0.1-0.3 mm,0.3-0.5 mm, 0.5-1.0 mm and 1.0-2.0 mm

as well. The slight increase in the smallest grain size fraction 0.1-0.25 mm is supposed to be related to the destruction of the aggregates of the grain size fraction 1-2 mm which might be detected as smaller aggregates by the software. The same trend is observed for M.PS 5min. The phenomenon can also be detected visually, see Figure 4.22. With increasing pump frequency, the amount of visible large aggregates is reduced for S.PS 5min and M.PS 5min while the effect is clearly less pronounced or even negligible for the longer pre-saturated mixtures.

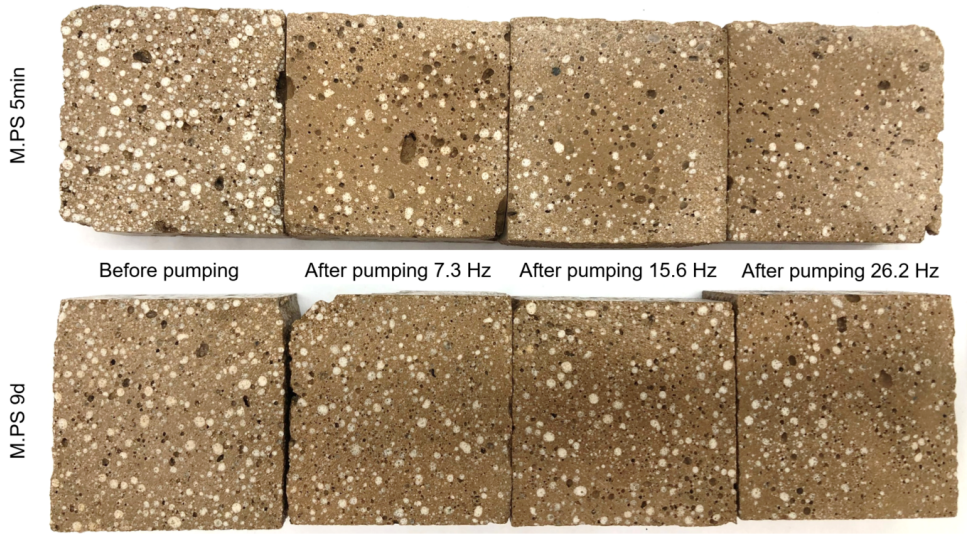

FIGURE 4.22: Photos of the hardened lightweight aggregate concrete samples taken before pumping (bp) and after pumping (ap) at different pump frequencies with the change in the amount of lightweight aggregates visible.

4.3 Implications on pumpability

The pressure correlates with the applied pump frequency, see Figure 4.23. This is true even for long duration of pumping (data up to 2.5 hours extrusion is considered). With a statistically significant correlation coefficient of 0.96, an increase in pump frequency results in an increase in pressure. Thus, if the material is to be conveyed faster, higher pressures act on the material. At the same time, an increase in temperature is determined see Figure 4.24.

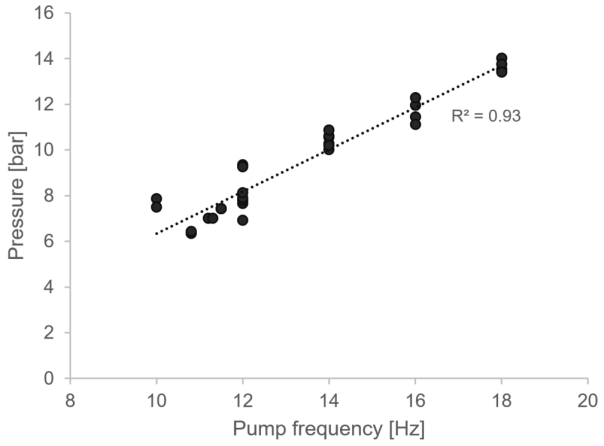

FIGURE 4.23: Pressure over pump frequency during pumping of M.PS 5min

Investigating data on temperature and pressure during pumping processes of various extrusion experiments (see Figure 4.25), positive correlation coefficient of 0.76 between temperature and pressure can be observed. Furthermore, temperature and pump frequency are statistically significantly correlating at 0.73. This is due to the friction in the process. Some of the mechanical energy is converted into heat, which can increase with increasing water absorption. Due to the absorption of water by the lightweight aggregates, less water remains available to build a lubrication layer. A lack of sufficient lubrication material to ensure full hydrodynamic stress transfer leads to increasing friction between pumped material and the wall, resulting in an increase in pressure and in heat. Furthermore, the lightweight concrete has a low thermal conductivity and thus, the dissipation of heat occurs slower than in normal weight concrete (Wesche, 1993).

The rheological properties as well as the hydration rate of concrete are strongly affected by temperature. High temperature accelerates the hydration rate and setting time in accordance with the Arrhenius law (Petit et al., 2005). Besides the internal friction in the hose, the pumping

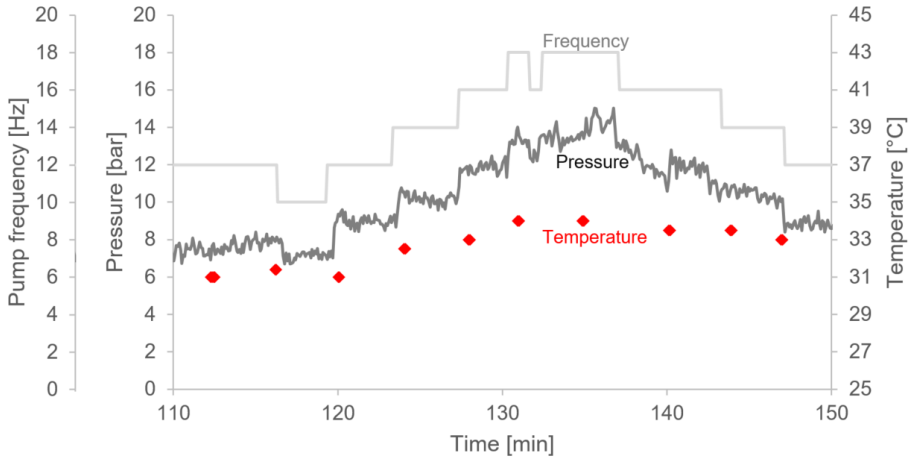

FIGURE 4.24: Time section from a long-running extrusion test showing the change of temperature during pumping with various frequencies and correlated pressure in the process

system itself might introduce heat to the material. During long pumping times (> 3h), the rotor-stator system of the pump heats up due to the friction in the rotating elements and transfers heat to the material inside. This is one explanation for the deviations in temperature in Figure 4.25.

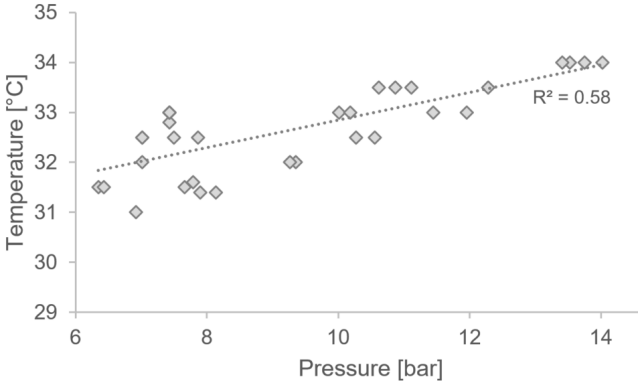

FIGURE 4.25: Temperature over pressure during pumping of M.PS 5min

Also in practical applications, heat affects the process. If the system is not externally cooled, temperatures might exceed 35° C for which the sulfate carrier of the applied cement was adjusted to. Exceeding this value let to a sudden change of workability of the concrete. An increased cracking of the deposited concrete as well as blockages in the pump were observed as a result. This might be due to a premature start of the hydration process or building of CSH instead of ettringite and should be investigated by further research, e.g., analyzing the formed phases. Similar effects are documented by literature: Biscoping and Beck (2014) state that fresh concrete temperature exceeding 30° C increases the reactivity of the cement clinker at decreasing solubility of the sulfate, which regulates solidification. Furthermore, they report that this generally leads

to a faster setting and solidification, poorer workability, higher early strengths, and cracking on the concrete surface.

A high water content helps, by reducing pressure in the hose, to reduce the temperature increase. In general, the water content and thus, the water-to-binder ratio $\frac{w}{b}$ has the most pronounced effect on the pumping behavior of concrete (Feys et al., 2016a). Nevertheless, too high $\frac{w}{b}$ ratios typically lead to segregation and the strength of the material decreases at an excessive water content. Also for the lightweight aggregate concrete considered, the increase of the water content was accompanied by a better pumpability, see also (Matthäus et al., 2019). This is due to an improvement of the ability to form a lubrication layer and an overall decrease in viscosity (Feys et al., 2016a; Secrieru, 2018). The same effect of improved pumpability is observed when pre-wetting the lightweight aggregates even though the consistency is not affected as much as it is by an increasing water content. Thus, the pre-saturation of lightweight aggregates over e.g., 9 days, reduces the increase in temperature in comparison to a mixture with only 5 minutes pre-saturation (Figure A.3 in the appendix).

In order to evaluate the effects of pumping on the material properties, the flow rate and the pumping pressure are analyed at different pumping speeds. The speed is controlled by the frequency of the drive shaft with pump frequencies of 7.3 Hz, 15.6 Hz and 26.2 Hz as explained in Section 3.6. Note that the pressure required to pump the material at different pump frequencies drops visibly with a longer pre-saturation (Figure 4.26).

It takes about half the pressure to pump the mixture pre-saturated over 9 days compared to the reference M.PS 5min. The flatter the curve in a pressure-flow rate diagram and the lower the pressure, the easier the material can be pumped as low pumping pressure is needed to ensure a given flow rate. Thus the pre-saturation clearly enhances pumpability, see Figure 4.26. This can be attributed to the fact that less water is absorbed by the longer pre-saturated lightweight aggregates and thus more water is available to the cement paste in relation to the shorter pre-saturated samples. Further, Figure 4.26 includes the change in density which has an influence on the flow rate in m^3/s presenting an upper and lower bound. The variations are higher for M.PS 5min as it shows a higher change in density than M.PS 9d.

Looking at the flow rate of mixtures during pumping at different pump frequencies (see Figure 4.27), the longer pre-saturated mixtures have a significantly higher flow rate than the reference mixtures M.PS 5min and S.PS 5min with 5 minutes pre-saturation. The flow rate generally increases with increasing pre-saturation time (see S.PS 2d and S.PS 7d in Figure 4.27). The

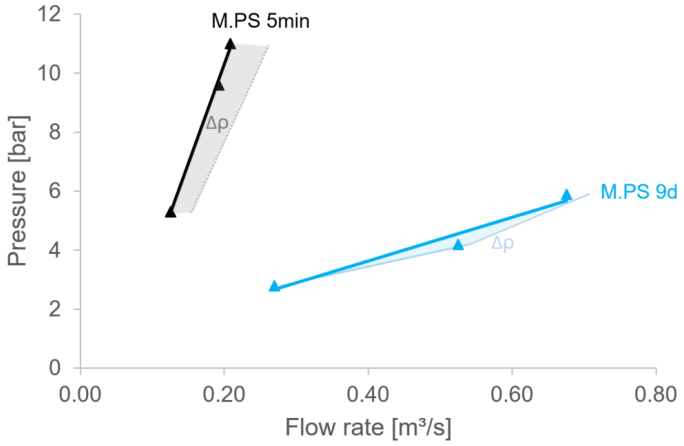

FIGURE 4.26: Effect of pre-saturation time on pressure and flow rate including variations in density (areas representing lower and upper bound)

thixotropy enhancing agent that makes the difference between M.PS 5min and S.PS 5min does not seem to have a decisive effect on the flow rate.

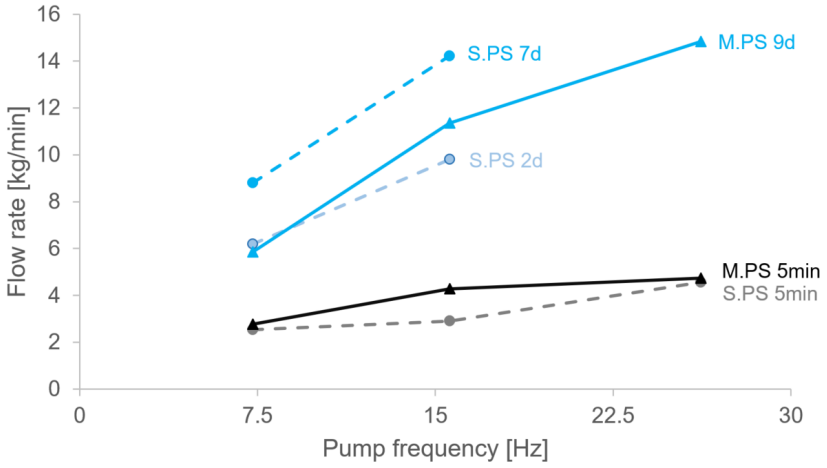

FIGURE 4.27: Effect of pre-saturation on flow rate

4.4 Implications on buildability

4.4.1 Results on static yield stress and structural build-up

The essential part of the extrusion process is the layer-by-layer deposition of the concrete strands. In order for this to take place without major deformation or failure, the buildability of the material must be assessed. For this purpose, the development of the yield stress over time is decisive.

Based on the static rheological measurements described in Section 3.7, Figure 4.28 shows the development of the static yield stress of the test series M.PS 5min and S.PS 5min as a function of time at rest. The structuration of the lightweight aggregate concrete develops quicker during the first 3 minutes, followed by a slower structuration rate thereafter. This is in line with literature, that re-flocculation occurs in short-term followed by structural build-up including early hydration products (Roussel et al., 2012; Kruger et al., 2019b).

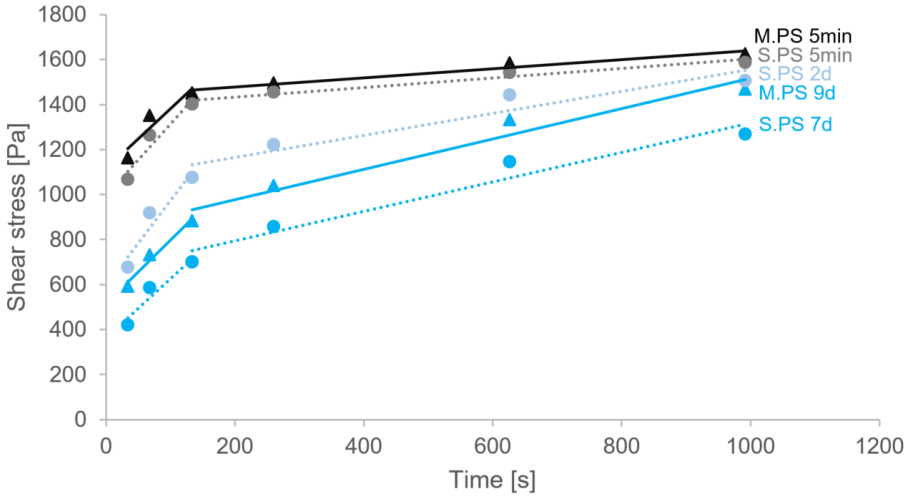

FIGURE 4.28: Structural build-up over time for test series M.PS 5min and S.PS 5min

The initial static yield stress of the normally pre-saturated mixtures M.PS 5min and S.PS 5min is visibly higher than that of the longer pre-saturated mixtures (Figure 4.28). The structuration rate in the first 3 minutes is similar for all mixtures with approx. 3.0 Pa/s. However, the structuration rate thereafter is higher for the longer pre-saturated mixtures with on average 0.6 Pa/s than for the M.PS 5min and S.PS 5min with a mean of 0.2 Pa/s.

Even though the shear stress after 1000 s (ca. 17 min) is almost the same for the normal mixtures and the longer pre-saturated mixtures, the yield stress in the first minutes is considerably lower for the longer pre-satured mixtures. Thus, the buildability for longer pre-saturated mixtures is considerably worse: For a given printing speed, the failure occurs earlier and at a lower height in the longer pre-saturated mixtures than in M.PS 5min or S.PS 5min, see Table 4.5. Therefore, the time to deposit further layers is considerably higher for longer pre-saturated mixtures than for the normally pre-saturated mixtures, see calculated values in Table 4.5.

Measurements with the rheometer reveal that the structuration rates for M.PS 5min and S.PS 5min in the second period of the bi-linear evolution (up to 1000 s after start of the test) are quite low with 0.2 Pa/s (see Figure 4.28). Accordingly, the development of the static yield stress

TABLE 4.5
Comparison of the calculated buildability for test series M.PS 5min and S.PS 5min

Assuming a bi-linear evolution of the static yield stress, the plastic failure for a given layer time of 10 s is calculated. Besides, the required layer time to extrude an object of 0.25 m height without failure is determined.

	Printing speed 10 s/layer			Object of 0.25 m
Mixture	Height at failure [m]	Amount of layers at failure [-]	Time of failure t_f [min]	Required layer time [s/layer]
M.PS 5min	0.23	26	4.3	30
M.PS 9d	0.16	17	2.9	43
S.PS 5min	0.22	25	4.1	46
S.PS 2d	0.20	22	3.7	46
S.PS 7d	0.12	13	2.2	61

is slower than the evolution of the applied loads by the deposition of subsequent layers and extrapolation would predict early failure. To enable a valid prediction for extrusion of larger building components, the structuration rate must be further examined for longer time spans. The mixture M.PS 5min performed best (Table 4.5) and will thus be further investigated.

The results for the mean long-time development of the shear stress for M.PS 5min are depicted in Figure 4.29 (for methods, see Section 3.7.2). The development of the shear stress after pumping over longer time periods is increasing with increasing first derivative of the curve (Figure 4.29, left). This is in line with the investigations of Perrot et al. (2016) who approximate the development with an exponential function. However, the shear stress of M.PS 5min before pumping still follows a linear evolution, see Figure 4.29, right.

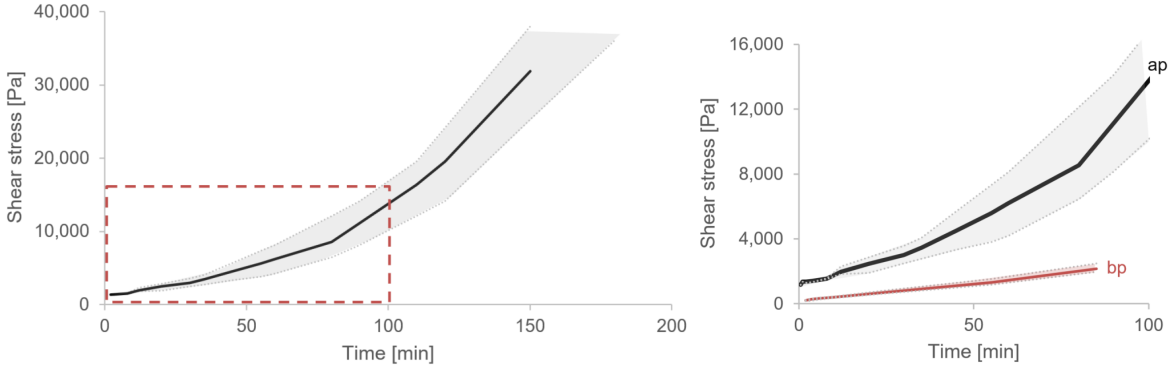

FIGURE 4.29: Evolution of shear stress values and their mean over time for test series M.PS 5min: overall evolution over 180 minutes after pumping (left) and close-up on difference before (bp) and after pumping (ap) in the first 80 minutes (right) with grey areas representing the variations in the repetitions

4.4.2 Calculation of failure times and limitations of available models

The plastic failure is calculated on basis of the measured yield stress values. As described in Section 3.7.4 there are different models to account for the static yield stress development. It was found that plastic failure varies widely for lightweight aggregate concrete before and after pumping, see Figure 4.30. The static yield stress is calculated assuming a linear, a bi-linear and an exponential evolution. For all investigations the mean of at least 5 static yield stress measurements are taken as a basis for the calculations.

As shown by Perrot et al. (2016) and Lecompte and Perrot (2017), the linear regression deviates for longer time spans while the exponential evolution is capable of modeling the development over a longer period of time, but is less precise in the initial time period. Thus, for the linear and bi-linear models a time period of 30 and 60 minutes with regard to the start of the measurements is evaluated while for the exponential model the values are considered until 120 minutes. The plastic failure for a given layer time of 30 s in experimental extrusion tests is 54 layers.

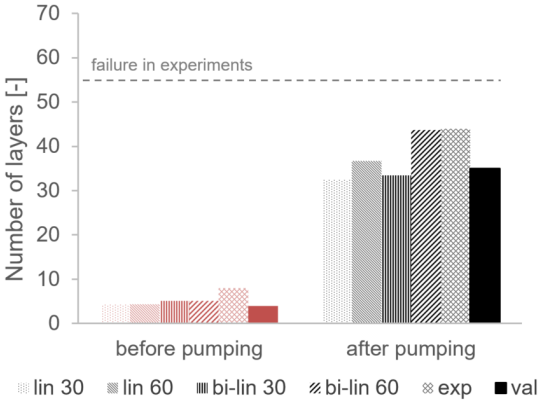

FIGURE 4.30: Number of layers until failure for test series M.PS 5min before and after pumping for a layer time of 30 seconds

When comparing the results on basis of the material before pumping (bp) and after pumping (ap), it is clear that predictions based on the material before pumping deviate considerably from the predictions made on basis of the material ap. The values on basis of M.PS 5min before pumping, predict a failure which is far from the failure observed in extrusion. With the material before pumping, on average only 5 layers would have been possible without failure if the next layer is deposited after 30 seconds. As the evolution of the static yield stress is more or less linear over time for M.PS 5min before pumping, there is almost no deviation between the linear models running over 30 and 60 minutes. The same is true for the bi-linear models. The exponential

model, however, overestimates the printable layers in the first minutes when comparing them to the measured values.

On basis of M.PS 5min after pumping, the critical amount of layers for failure is underestimated by 10 layers on average (42 layers instead of 54 layers, where it failed during the extrusion test), Figure 4.30. Linear and bi-linear models underestimate layer numbers more pronounced than for the exponential models, especially if the regression is based on measurements of the first 30 minutes, even though the failure occurred during the first 30 minutes (precisely at 28 minutes). The linear model (according to, e.g., Roussel (2018)) is widely applied. However, it is often not specified in literature over what time range the regression is run. As can be seen here, this is relevant for the prediction results and should always be considered.

The exponential model which is fitted to the measured values gives a similar estimation as the bi-linear approach over 60 minutes. Besides the exponential model applied here, literature suggests an adapted exponential model approach, see Perrot et al. (2016) and Section 2.3.2. In order to determine the plastic failure according to their approach, it is necessary to determine the fitting value t_c in real buildability tests in order to calibrate the model. For $\tau_{0,S} + A_{thix} \cdot t_c \cdot (e^{t/t_c} - 1) = 1218 + 1.04 \cdot 2623 \cdot (e^{t/2623} - 1)$ the calculated failure fits the real failure well. However, the values do not represent physically defined parameters and can only be determined with great effort, i.e. by producing the real failure. In addition, the curve is then only optimized for one point and does not necessarily represent a correct prediction for all extrusion heights.

Note that only the changes during the pumping process enable buildability of the investigated lightweight concrete mixtures and allow for a reasonable printing speed. Figure 4.31 underlines this point depicting the required time per layer in order to extrude an object of 2 m height with M.PS 5min after pumping. In comparison, a considerably higher time per layer (roughly x3) would be needed in order the same object of 2 m height without plastic failure for M.PS 5min before pumping.

The prediction based on material after pumping, which was pumped at a given pumping rate, cannot be applied generally since the material properties change depending on the pressure level during pumping. Thus, there may be even greater deviations between the model predictions and the failure that actually occurs.

Wolfs et al. (2018) differentiate in plastic collapse due to compression failure and due to pressure-dependent shear failure. Calculating the failure height due to compression failure (see equation (2.12)), the prediction on basis of the unpressurized compressive test is highly overestimating

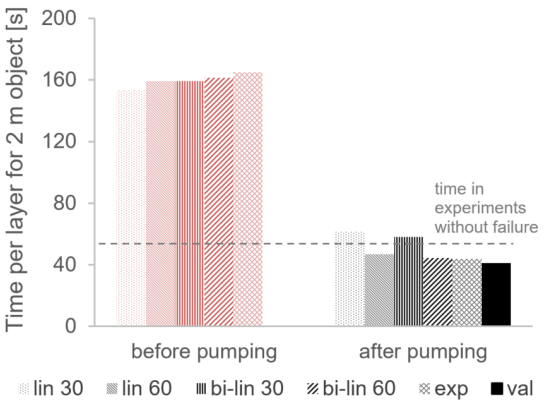

FIGURE 4.31: Required time per layer in order to built an object of 2 m height with material M.PS 5min

the printable layers (277 layers). The same is true for the evaluation of the green strength with pressurization–the predicted amount of layers is 140. It might be surprising that the failure in the pressurized case is predicted earlier. This is due to the fact that the density of the pressurized material is significantly higher. The high values for compression failure suggest, that the failure is more probable to occur due to pressure-dependent shear failure for the lightweight concrete under consideration.

Comparing all shear failure models, the required times per layer without plastic failure for different extrusion heights are revealing: up to a height of 1 m, the required time increases considerably while the required increase afterwords is rather low for most models, see Figure 4.32. Real objects of 1.8 m, 1.0 m, 0.8 m, 0.4 m and 0.2 m height were 3D-printed without failure at a printing speed of 66 s, 54 s, 53 s, 31 s and 18 s per layer respectively. At this layer time no failure occurred. However, it might have been possible to reduce the time per layer even further. Due to the high effort required for the production of extruded elements in the laboratory, the critical value for failure at more than 1 m was not tested intensively in experimental tests, rather a value was selected that was on the safe side according to the measured values. However, if the values predicted by the models exceed these values, the model definitely underestimates the possible time per layer.

For building heights exceeding 1 m, the linear and bi-linear approaches, which are based on the yield stress values of the first 30 minutes after deposition, underestimate the time per layer. This is related to the fact that the structural build-up of the material increases after 30 minutes and that the extrusion of an element of 1 m would already take more than one hour at a layer time of 40 s/layer. A stronger development in strength is expected to happen thereafter due to the start of hydration processes. Furthermore, measurements do not include the temperature

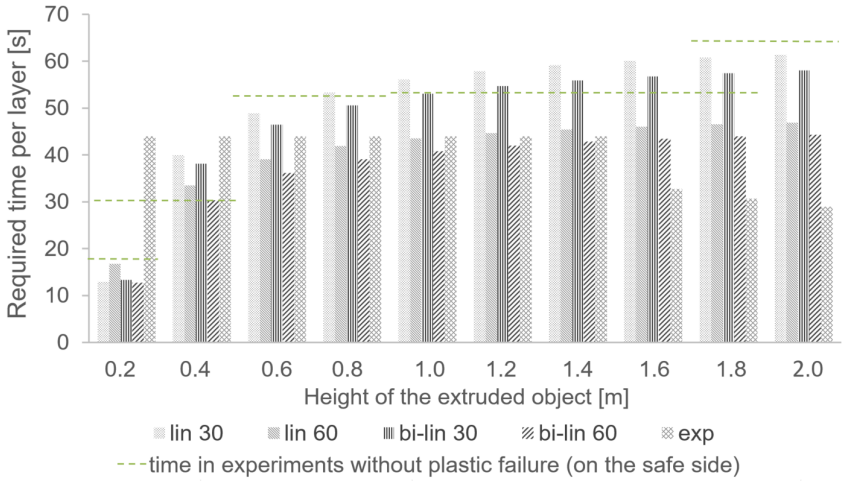

FIGURE 4.32: Required time per layer in order to built an object of different height with M.PS 5min

increase when pumping for a long time. This increase in temperature, however, might also have an effect on the building of early hydration products, see Section 4.3. The exponential model underestimates the possible time per layer at least up to a height of 0.6 m. This is due to the fact that with an exponential function, the development is very slow at the beginning, which does not correspond to the real development of the concrete, as already noted by (Perrot et al., 2016).

4.4.3 Predictive model including effects of pumping pressure

The pressure during pumping has a decisive influence on the material properties of lightweight concrete as outlined in the previous sections. Therefore, pressure needs to be integrated into models on buildability. The aim is not to simply fit yield stress in order to meet the real failure, but to include physically observed effects into the buildability model. The validation is started in a first case study, but further validation studies are required in future research.

To collect the required data, the shear stress change in dependence of the pressure is analyzed in a pressure cell. As the material is stiffening significantly due to the pressure and a shearing-off is often observed during rheological measurements (see Section 4.1.3), the static yield stress over time is firstly determined on the fresh lightweight concrete without pressure over a time of 90 minutes (results see Figure 4.33). Within the first 5 minutes ($t_r = 300\,\mathrm{s}$), a stronger increase in shear stress, which can be traced back to re-flocculation (Kruger et al., 2019a), occurs than between 5 minutes and 55 minutes (3300 s), where normal structuration takes place. Starting at approx. $t_h = 60$ minutes, the structuration rate increases again, which can be traced back to

increased hydration. Thereupon, structuration is expected to happen exponentially as described by, e.g., Mettler et al. (2016); Perrot et al. (2016).

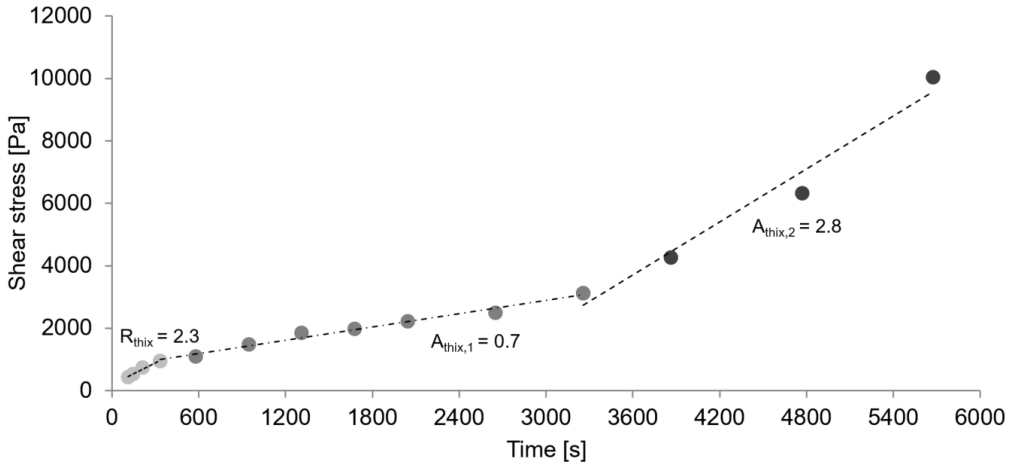

FIGURE 4.33: Shear stress over time at ambient pressure determined with the pressure measuring cell for test series M.PS 5min

In order to calculate failure over the whole printing period, the evolution over time is approximated tri-linearly. Similar as in the bi-linear approach (see equation (2.10)), the time of failure can be estimated via equations (4.1), (4.2), and (4.3) with $t_r = 300\,s$ and $t_h = 3600\,s$:

$$t_{p,1} = \frac{t_{0,S}}{\rho g \dot{s}/\alpha_{geom} - R_{thix}} \text{ for } [t \leq t_r], \tag{4.1}$$

$$t_{p,2} = \frac{t_{0,S} + R_{thix} \cdot t_r - A_{thix,1} \cdot t_r}{\rho g \dot{s}/\alpha_{geom} - A_{thix,1}} \text{ for } [t_r < t \leq t_h], \tag{4.2}$$

$$t_{p,3} = \frac{t_{0,S} + R_{thix} \cdot t_r + A_{thix,1} \cdot (t_h - t_r) - A_{thix,2} \cdot t_h}{\rho g \dot{s}/\alpha_{geom} - A_{thix,2}} \text{ for } [t > t_h]. \tag{4.3}$$

$A_{thix,1}$ is considerably lower than R_{thix} and $A_{thix,2}$ (see Figure 4.33), Accordingly, the material age between t_r and t_h might be limiting for the building rate. As a consequence, when determining a minimum time per layer $\dot{l}$ for a given height H_t based on equation (4.3) via equation (4.4)

$$\dot{l} = \frac{\rho g H_t/\alpha_{geom} - t_{0,S} - R_{thix} \cdot t_r - A_{thix,1} \cdot (t_h - t_r) + A_{thix,2} \cdot t_h}{A_{thix,2}}, \tag{4.4}$$

a preceding failure in lower layers cannot be determined.

Thus, the minimum time per layer must be the maximum of equation (4.4) and equation (4.5).

$$\dot{l}_{min} = \frac{\rho g \cdot t_h \cdot h_i / \alpha_{geom}}{t_{0,S} + R_{thix} \cdot t_r + A_{thix,1} \cdot (t_h - t_r)} \tag{4.5}$$

In addition to the static rheological measurements (see Table A.6 in the appendix), newly developed static pressure tests (see Section 4.1.3 and Table A.5) are conducted. The two tests are combined in order to estimate the development of the static yield stress over time for differently pressurized materials. To include the physical phenomenon of change of material properties under pressure, the values determined in the pressure cell as described in Section 4.1.3 (see especially Figure 4.13) are used. The increase in dependence of the pressure can be approximated by a linear equation with a slope of $\dot{P} = 210$. The increase between the pressure levels is added as a constant to the static yield stress development measured on the material without pressurization over time. As a consequence, the initial yield stress increases with increasing pressure while the evolution in shear stress is parallel to the unpressurized material, see Figure 4.34. Note that the unpressurized material is exposed to ambient pressure of 1 bar.

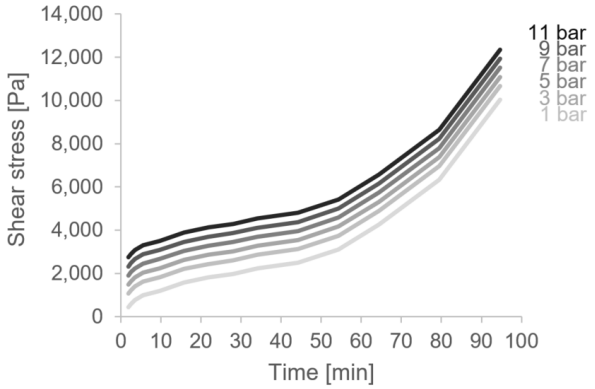

FIGURE 4.34: Shear stress over time for varying pressure for test series M.PS 5min

Taking the increase in shear stress (as depicted in Figure 4.34) and the increase in density under pressure (see Figure 4.2) into account, the failure times—assuming a linear evolution of shear stress—can be calculated in dependence of the pressure applied. Figure 4.35 shows the number of layers at which an object is predicted to fail at a layer time of 31 s in dependence of the pressure. The higher the pressure applied on the material, the higher its density and the higher its shear stress. In general, the consideration of pressure can be combined with every model for the development of shear stress over time, i.e. linear, bi-linear, exponential or other.

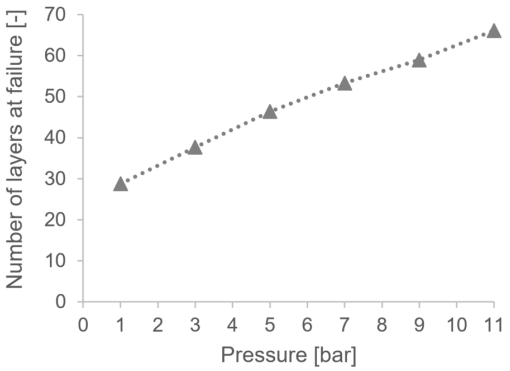

FIGURE 4.35: Calculated number of layers at failure for layer time of 31 s with material M.PS 5min at varying pressure

A model based on a tri-linear approach is developed (see Figure 4.33). As the observed plastic failure in the experiments occurred within 30 minutes (lower than $t_h = 60\,min$ and larger than $t_r = 5\,min$), the plastic failure can be calculated—similar to the linear approach in equation (2.2)—equating the stress applied by the subsequent layers and the strength of the material as in equation (4.6).

$$\tau_0(P) + R_{thix} \cdot t_r - A_{thix,1} \cdot t_r + A_{thix,1} \cdot t = \frac{(\rho(P) \cdot g \cdot \dot{s}}{\alpha_{geom}} \tag{4.6}$$

As $H_{f,p} = t \cdot \dot{s}$, the plastic failure height $H_{f,p}(P)$, which depends on the pressure, is

$$H_{f,p}(P) = \frac{\tau_0(P) + R_{thix} \cdot t_r - A_{thix,1} \cdot t_r}{\rho(P) \cdot g/\alpha_{geom} - A_{thix,1}/\dot{s}}. \tag{4.7}$$

Thus, the number of layers can be calculated via equation (4.8).

$$a_f(P) = \frac{H_{f,p}(P)}{h_i} = \frac{\tau_0(P) + R_{thix} \cdot t_r - A_{thix,1} \cdot t_r}{h_i \cdot (\rho(P) \cdot g/\alpha_{geom} - A_{thix,1}/\dot{s})} \tag{4.8}$$

The calculation of buildability includes both, the density $\rho(P)$ and the yield stress $\tau_0(P)$, but they have opposite effects. The increase in density due to pressure reduces buildability while the increase in yield stress due to pressure increases it. As the predicted failure occurs at a significantly higher number of layers with increasing pressure, the effect of the yield stress increase prevails. The buildability enhances with pressure application. However, at further increase of pressure, the negative effect of increasing density on possible building heights might get predominant, see schematically in Figure 4.36.

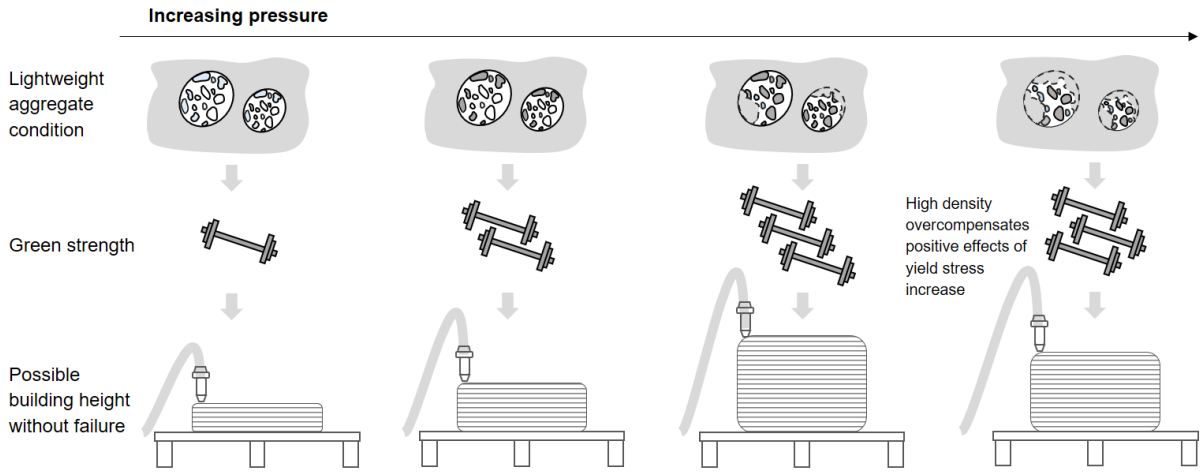

FIGURE 4.36: Schematic correlations between pressure, condition of lightweight aggregates, green strength and possible building height without failure

To compare the model with the actual failure during extrusion (see Section 3.7.4), it is necessary to use the pressure that was present during the fabrication of this specimen, which is approx. 7 bar. At a pressure of 7 bar, the object is predicted to fail at 54 layers. This matches exactly the real failure at 54 layers. Thus, the approach provides a considerably better estimation than the linear, bi-linear and exponential predictions on basis of material after pumping or the predictions on basis of material before pumping without consideration of the pressure (see Section 4.4.2). Furthermore, predictions based on the new model are achievable with considerably lower effort and material consumption.

Applying the same newly developed approach (considering the results on change in density during pumping), the required vertical building rate, which is required in order to reach a distinct extrusion height without failure, can be calculated on basis of the values before pumping via $\dot{s} = H/t_p$. The vertical building rate could be higher for heights exceeding 1 m, but is limited by the low structuration rate in phase 2 of the tri-linear shear stress development. Thus, for $t > t_h$ it is limited to

$$\dot{s}_{max} = \frac{t_{0,S} + R_{thix} \cdot t_r + A_{thix,1} \cdot (t_h - t_r)}{\rho g t_h / \alpha_{geom}}. \tag{4.9}$$

Accordingly, the minimum vertical building rate increases in pressure, see Figure 4.37. Starting from a desired height, which shall be extruded, the required vertical building rate can be read off in Figure 4.37 for material M.PS 5min. This allows to assess in advance the boundary conditions and the limits for application in practice.

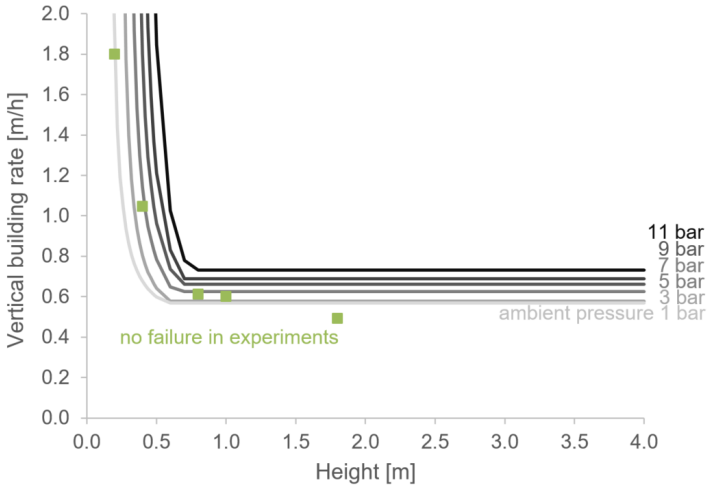

FIGURE 4.37: Achievable vertical building rate over height for extrusion avoiding plastic failure according to a tri-linear yield stress model for material M.PS 5min. Furthermore, results of extrusion experiments without failure with pressures between 6-8 bar shown in green for validation purposes

With regard to material development, the results show that high structuration and an early start of hydration (low t_h, e.g., via addition of accelerators) are favorable for high vertical building rates. This is in line with literature, see Section 2.3.2.

Such diagram can be developed in advance for each material based on two types of measurements in the pressure measuring cell: 1. classical static rheological measurement without pressure, 2. newly developed measurement with increase of pressure and evaluation of the peaks.

As soon as a suitable material is pumped for the first time, it can be determined directly on basis of the pressure recorded in the pump to which vertical building rate the process must be limited to achieve the desired height. This avoids the need of process-parallel testing on the extruded material and process-parallel or post-process analyzing. Thus, the limitation that statements on possible failure can only be made for the current material age or for subsequent extrusion processes—as has mainly been the case up to now—can be substantially reduced. Figure 4.38 shows that the model includes the time before deposition and is thus able to extrapolate the required green strength of the material in dependence of the pressure applied during pumping. Furthermore, the model can be extended by another upper bound to avoid blockages, see schematically in Figure 4.38.

For validation, values for 3D-printed objects with material M.PS 5min, which did not collapse during the layerwise construction phase, are shown in Figure 4.37. During extrusion of the objects, pressures of 6-8 bar are recorded. The model fits these values as it does not predict failure at the respective heights for a pressure of 7 bar. For lower pressures of 1-3 bar, however,

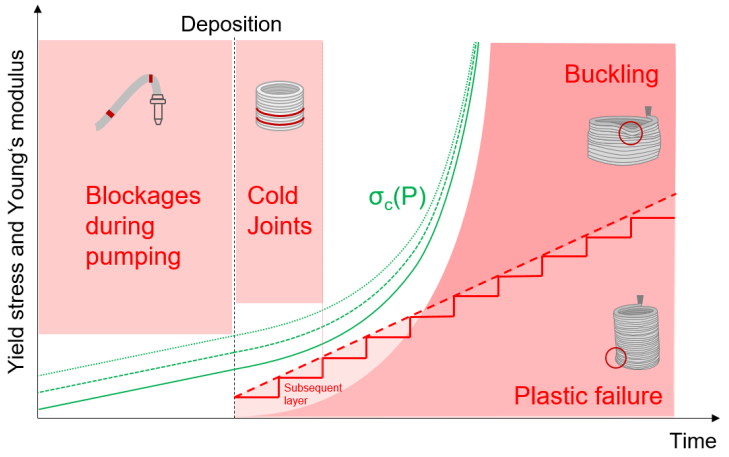

FIGURE 4.38: Requirements on yield stress and Young's modulus for extrusion (red areas) as well as optimal range of yield stress and Young's modulus for each layer (green line) including evaluations before deposition and effect of pumping pressure (P)

most of the objects would have failed according to the model at the set printing parameters. Lightweight aggregate concrete thus performs better under pressure in terms of buildability. Conducting several failure tests, the model can be further validated in future research.

4.4.4 Buckling failure

Elastic buckling depends considerably on the geometry of the extruded object. As the focus in this thesis lies on the material and the development of the lightweight concrete during pumping, investigations regarding buckling are limited to a simple geometry. The failure time for buckling is calculated on basis of the green strength evaluations. Compression tests are carried out on pressurized and not pressurized material in order to assess the extent to which changes under pressure affect the mechanical properties of the fresh lightweight concrete and, consequently, the buildability. Static rheology measurements accompany the compression tests, see Section 3.7.3.

Figure 4.39 presents the mean static yield stress for M.PS 5min. Without pressure ($\bar{p}$), it is approx. 173 Pa and the structural build up over time, assuming a linear evolution, is approx. 22.5 Pa/min or 0.38 Pa/s respectively. Following a least-squares approach, the best linear fit is accepted with $R^2 = 0.996$. The standard deviations between the mixtures are approximately 8-16 % over 90 minutes which means that the deviations in the material should not have a strong effect on the results of compressive and shear strength.

The uniaxial compression tests are, above all, important to evaluate the Young's modulus of the mixtures. This is crucial for the analysis of the buildability phase, especially in terms of failure

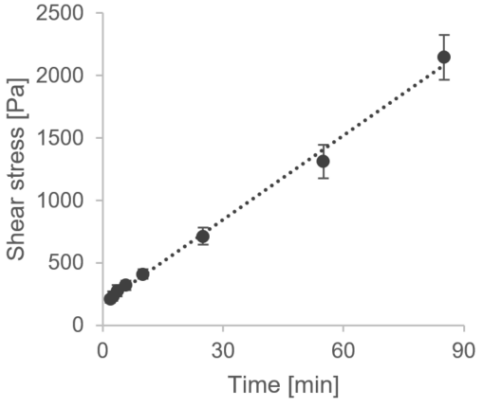

FIGURE 4.39: Static shear stress over time for test series M.PS 5min

due to elastic buckling, see Section 4.4. Figure 4.40 depicts the development of the Young's modulus and the green strength over time for M.PS 5min. The Young's modulus is determined in the linear-elastic area of the compression tests, see Figure 4.41. The values are compared over material age (time). The best linear fit has a R^2 of 0.99. The evolution of the Young's modulus is approx. $E = E_0 + \xi_E \cdot t = 0.016 + 0.0017 \cdot t$ for M.PS 5min at normal sample preparation and $E = 0.058 + 0.0018 \cdot t$ for M.PS 5min after pressurization. Consequently, the initial Young's modulus E_0 increases due to the exposure to pressure while the evolution over time ξ_E stays approximately the same.

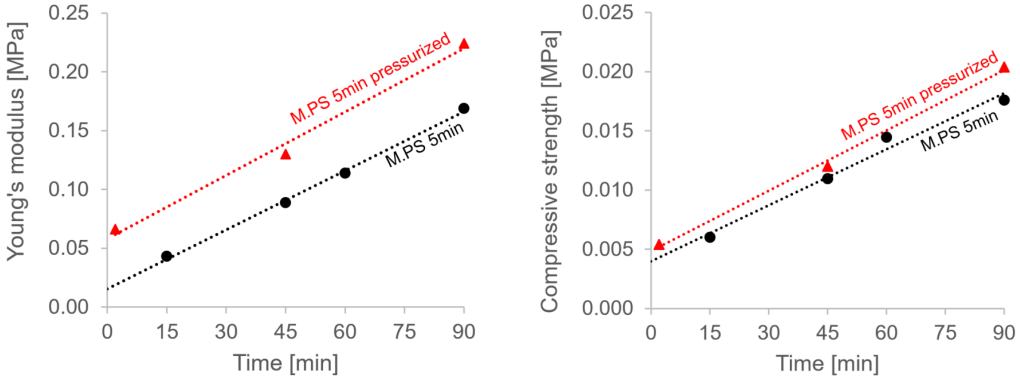

FIGURE 4.40: Green strength and Young's modulus over time for test series M.PS 5min

The uniaxial compression tests can also be evaluated in terms of strength. Figure 4.41 shows that the maximum green strength increases, ceteris paribus, with increasing material age. Furthermore, the peak is reached at lower strain for increasing material age.

Note that green strengh is an almost linear function of material age (see Figure 4.40, right). The exposure to pressure leads to a further increase in strength: 90 minutes after water addition

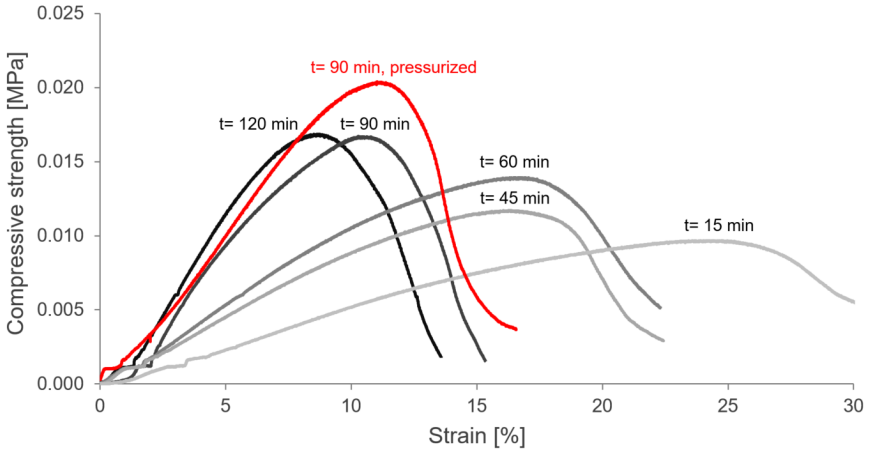

FIGURE 4.41: Green strength over strain determined in compression tests at increasing material age (in minutes) as well as on pressurized material for test series M.PS 5min

(min a.w.), the material which is pressurized at 30 min a.w. and inserted into the formwork at 42 min a.w. has a significantly higher peak than the not pressurized material 90 min a.w. even though the not pressurized material is inserted into the formwork at approx. 5 min a.w. (see red line in Figure 4.41). However, the differences for the green strength are not as large over time (Figure 4.40, right) and may be neglected. The evolution of the green strength can be summarized as $\sigma_c = 4.9{+}0.14{\cdot}t$ for M.PS 5min at normal sample preparation and $\sigma_c = 4.8{+}0.17{\cdot}t$ for M.PS 5min after pressurization.

Table 4.6 summarizes the material properties for both the pressurized (p) and not pressurized material ($\bar{\text{p}}$) as a basis for the calculations of buckling failure.

TABLE 4.6
Fresh material properties of pressurized and not pressurized lightweight concrete

In order to evaluate the influence of pressure during the pumping process on buckling, the fresh material properties are determined on both the not pressurized ($\bar{\text{p}}$) and the pressurized lightweight concrete (p).

Parameter	Symbol	Unit	Not pressurized material	Pressurized material
Density	ρ	$[\frac{kg}{m^3}]$	1070	1300
Initial Young's modulus	E_0	[Pa]	16,000	58,000
Curing rate	ξ_E	$[s^{-1}]$	0.0018	0.0005
Green strength	σ_c	[Pa]	$\sigma_c = 3980 + 160 \cdot t$	$\sigma_c = 4830 + 170 \cdot t$
Initial yield stress	τ_0	[Pa]	3980	4830
Curing rate in compression	$\xi_{\sigma,c}$	$[s^{-1}]$	0.0007	0.0006

Exemplary, buckling of a straight, free standing wall element with a width of $\delta = 25$ mm (i.e. a single strand of material), a length of $L = 1000$ mm, and a layer height of $h_i = 9$ mm is analyzed.

The vertical building rate is $\dot{s} = 0.2\,\text{mm/s}$ which corresponds to a time per layer $\dot{l}_i = 45\,\text{s/layer}$. The aim is to evaluate whether the total height of $H_t = 1\,\text{m}$ can be reached without failure.

The calculations are conducted as described in Section 3.7.4: The predicted height for a plastic collapse $H_{f,p}$ can be calculated via equation (2.12) and is analytically $H_{f,p} = -3.42\,[m]$. As the calculated failure is smaller than 0, there is no plastic failure expected at the given process and material parameters. The initial bending stiffness is $D_0 = 0.083\,[Nm]$ according to equation (2.15). The predicted buckling height $H_{f,b}$ is estimated via equation (2.16) resulting in $H_{f,b} = 0.14\,[m]$. As the predicted failure height $H_{f,b}$ is lower than H_t and no failure due to plastic collapse is predicted, the wall is likely to fail due to elastic buckling. Thus, buckling of a single strand with 25 mm width occurs at a height of approx. 0.14 m for the lightweight concrete mixture M.PS 5min based on the pressurized material properties (p) at a layer time of 45 seconds. This corresponds to approx. 16 layers.

The stability failure can occur in any layer. The slimmer a geometry, the higher the risk for buckling. The connection of the individual strands with each other as well as the geometry of a 3D-printed object as a whole have a major effect on the probability of stability failure: If each strand stands on its own, the resulting slender geometry tends to fail much earlier than if several layers work together or the entire component width can be applied. For two strands deposited next to each other ($\delta = 50\,\text{mm}$), the buckling for M.PS 5min (p) occurs at 27 layers. Thus, 13 layers later than for a width of 25 mm. Combining several layers to a object width of 500 mm, the elastic buckling would only occur at 165 layers (approx. 1.5 m height) for the process parameters described above.

Furthermore, a lower density at otherwise equal parameters, leads to later elastic buckling. For a density of 2600 $\frac{kg}{m^3}$, the failure would occur already 3 layers earlier (at layer 13 instead of 16 as for M.PS 5min (p) for $\delta = 25\,\text{mm}$). Thus, as little change as possible in density is favorable to avoid elastic buckling. Also, the initial Young's modulus and the curing rate of the material are important and might change during pumping. The higher they are, the later elastic buckling occurs. The yield stress, however, has no influence on the timing of the elastic buckling, but only on the issue whether elastic buckling or plastic collapse will occur first. The same calculations as above are done for M.PS 5min before exposing the material to a pressure ($\bar{\text{p}}$). The elastic buckling for an otherwise identical setup is predicted to happen at a height of approx. 0.11 m which is approx. 13 layers for M.PS 5min ($\bar{\text{p}}$). Higher density and higher Young's modulus have opposite effects, with the increase in elasticity predominating in this case. Thus, as for the plastic failure, elastic buckling occurs later for the lightweight concrete when exposed to pressure.

Summarizing, changes in material properties during pumping are positive for the buildability including the stability and avoidance of buckling.

4.5 Implications on hardened concrete properties

Strength

The compressive and flexural strength are determined on prisms which are produced in parallel to pumping and extrusion tests. The prisms are tested after 7 days during which they are stored at laboratory conditions of $20 \pm 1\,°C$ and 65 ± 5 % relative humidity. For every state (before pumping and after pumping at different velocities) at least 5 samples are evaluated and mean values are compared, see Figure 4.42. Following a least squares approach, a linear trend is established for the evolution of density, compressive and flexural strength over pump frequency with $R^2 > 0.91$ and correlation coefficients of 0.95 and higher. The flexural and compressive strength do also correlate with the density with correlation coefficients of 0.97 and 0.87 respectively. The investigations of the hardened state confirm the observations made in fresh state that the density increases with increasing pumping speed and as a consequence the strength of the material increases as well.

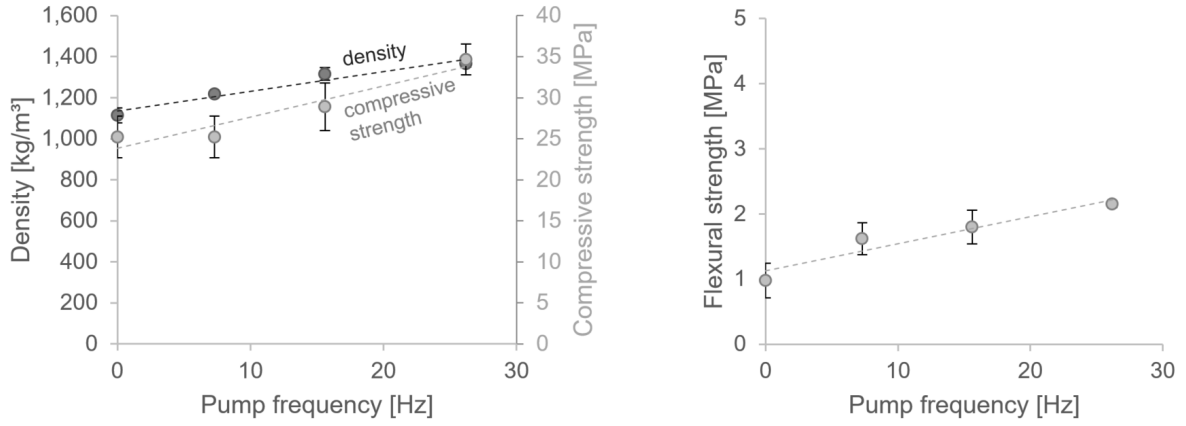

FIGURE 4.42: Compressive strength and density (left) as well as flexural strength (right) of M.PS 5min prisms after 7 d as a function of pump frequency

Furthermore, tests on cylinders are conducted. Figure 4.43 summarizes the mean values of compressive strength and Young's modulus in hardened state. The strength and stiffness is determined after 28 days during which they are stored at laboratory conditions of $20 \pm 1\,°C$ and 65 ± 5 % relative humidity. For each sample (before pumping or pumped with a frequency of 7.3 Hz, 15.6 Hz or 26.2 Hz) three cylinders are tested and mean values are calculated.

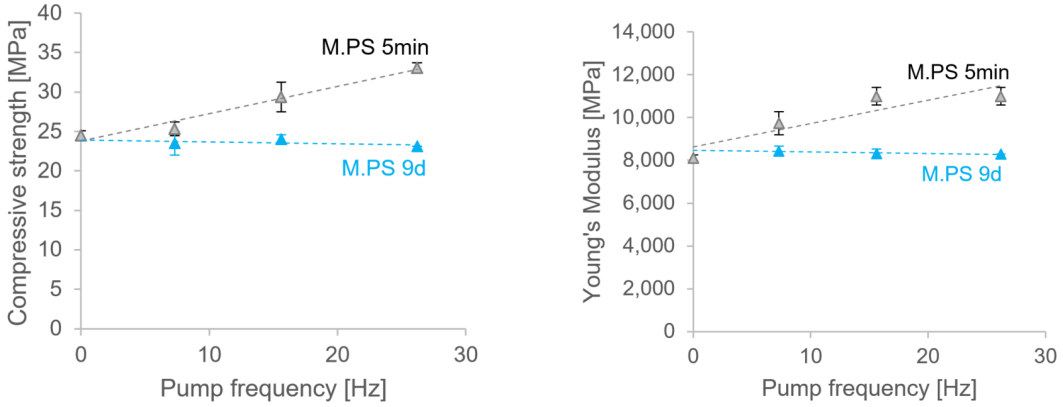

FIGURE 4.43: Compressive strength and Young's modulus of M.PS 5min and M.PS 9d at hardened state (28 d) as a function of pump frequency

The same trend as for the prisms is observed for M.PS 5min. The values of M.PS 5min before pumping serve as lower bound, which is improved through the pumping process due to destruction and paste absorption of the lightweight aggregates as described in Section 4.2. The pumping at 7.3 Hz results in an increase of compressive strength by 4 %, 15.6 Hz by 20 % and 26.2 Hz in an increase by 35 %. The increase in Young's modulus is approx. 20 % for a pump frequency of 7.3 Hz in comparison to the stiffness before pumping and approx. 35 % for 15.6 Hz and 26.2 Hz. For the longer pre-saturated mixture M.PS 9d, however, the compressive strength and the Young's modulus are almost constant before pumping and after pumping at different pump frequencies.

Layer bonding

As described in Section 2.3.4, layer bonding has a significant influence on the direction-dependent flexural strength of prisms. The physical-chemical connection between the layers suffers with increasing waiting time between deposition of layers. Furthermore, superficial drying influences the porosity of the material at the layer bonding (Keita et al., 2019). In order to reduce the anisotropy due to the layer-wise production and reach relative homogeneous material characteristics over the entire structure, it would be beneficial to deposit the material at once. This is obviously not possible with regard to buildability (Section 2.3.5). Thus, investigations on the decline of the layer bonding with increasing waiting time between the deposition of subsequent layers are conducted. The compressive strength is almost direction-independent with 25 MPa after 7 days. The flexural strength at varying time gaps and directions are listed in Table 4.7.

TABLE 4.7
Direction-dependent flexural strength at varying time gaps

This table summarizes the mean values of flexural strength of extruded lightweight concrete in dependence of their direction (sawn-out horizontally or vertically) and the time gap. The time gap refers to the waiting time between the deposition of subsequent layers. For each sample three prisms are tested and mean values are calculated. The strength is determined after storing for 7 days at laboratory conditions with $20 \pm 1\,°C$ and 65 ± 5 % relative humidity.

	Flexural strength mould [MPa]	Flexural strength extruded [MPa]		
Time gap		2 min	5 min	10 min
Horizontally	2.2 ± 0.5	3.4 ± 0.1	3.4 ± 0.1	3.4 ± 0.1
Vertically	2.2 ± 0.5	2.9 ± 0.5	1.6 ± 0.1	1.7 ± 0.5

Horizontally sawn-out prisms (see Figure 3.13) achieve the highest flexural strength. The difference to the mould prisms might be due to the vibration applied to the mould prims which might have a reversing effect on the changes during pumping which does not occur in the layerwise deposition during extrusion. The difference to the vertically sawn-out prisms can be traced back to the larger effect of the layer bonding on the vertical prisms (Section 2.3.3). While the horizontally sawn-out prisms do not show a significant deviation with increasing time gap, a drop in flexural strength can be seen at the vertically sawn-out prisms. This is due to the deterioration of the layer bonding which affects the vertical prisms more severely. It leads to predetermined breaking points in the prisms. Thus, without further reinforcement, layering can be avoided with the applied lightweight aggregate concrete by keeping the waiting time between the layers below 2 minutes.

Thermal conductivity

The thermal conductivity of the lightweight aggregate concrete influences the insulation capacity of the structure. The thermal conductivity of the material varies with the pump frequency it was exposed to. For M.PS 5min, the thermal conductivity of the material before pumping is the lowest and it increases with increasing pumping speed. On the contrary, for M.PS 9d, the thermal conductivity decreases slightly with pumping speed, see Figure 4.44. This might be due to partial release of the absorbed water.

When the material is oven-dry, the differences in thermal conductivity depend only on the exposure to pumping pressure and implied changes in density, see Figure 4.45 (left). The pump frequency seems not to have an influence on the thermal conductivity of the oven-dry mixtures. The fact that the linear increase that occurs in the non-dried samples is no longer visible in the

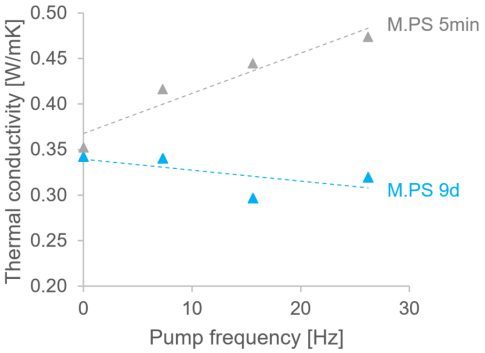

FIGURE 4.44: Thermal conductivity of M.PS 5min and M.PS 9d over varying pump frequencies with a pump frequency of 0 corresponding to samples before pumping

oven-dry samples suggests that the differences in this case are mainly due to the (reversible) water absorption of the lightweight aggregates.

With increasing density, the thermal conductivity increases (Figure 4.45), which is a well known phenomenon. As described in Section 4.1, the density increases with increasing pumping speed and so does the thermal conductivity of the material (see Figure 4.45, right). When drying the material, the pumped material adjusts to a similar thermal conductivity of 0.29 W/mK independent of the pumping speed. However, it stays significantly higher than the thermal conductivity of the not pumped material with 0.23 W/mK.

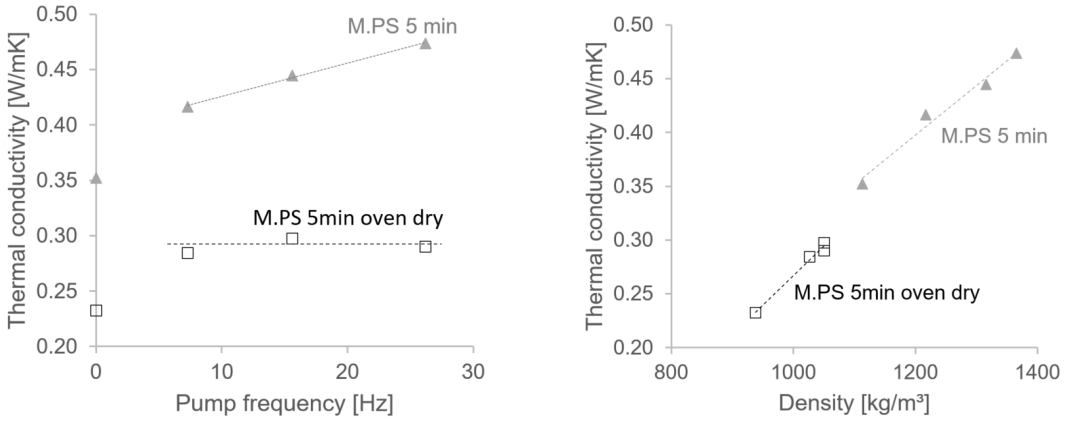

FIGURE 4.45: Thermal conductivity for oven-dry and fresh lightweight aggregate concrete M.PS 5min with a pump frequency of 0 corresponding to samples before pumping (left) and over density of the samples (right)

Summarizing, both, strength and thermal conductivity increase with increasing density. However, the goal is to achieve a low thermal conductivity of the material in order to have a good insulation effect while high strength is favorable for load-bearing. Thus, the requirements on strength and thermal conductivity are contradicting. The increase in density is favorable for

buildability and strength, but disadvantageous for insulation properties. Furthermore, both parameters dependent on geometry. Thus, the overall concept of geometry and material properties has to be optimized with regard to individual requirements of construction components.

This can be realized via a cellular structure with the cavities filled with air or with granular insulation material. The insulation capacity is affected by the overall porosity of an element. Besides the solid material properties themselves, reducing the air to solid ratio via the geometry affects the overall insulation capacity considerably (Ramakrishnan et al., 2021). The overall possibility of such a concept was shown for material M.PS 5min in the associated research project and has been further investigated in an interdisciplinary team (Briels et al., 2022) and shall be extended in further research to include the aspect of structural optimization as well.

5 | Summary

The three main goals of this thesis were to analyze whether lightweight concrete is apt for extrusion, to investigate the causes and magnitude of changes in material properties during extrusion and to assess the influence of these changes on buildability. In general, lightweight aggregate concrete is apt for extrusion. Especially with regard to buildability and thermal conductivity, lightweight aggregate concrete has advantages over normal weight concrete. Due to its low density, it facilitates light structures, e.g., for additions and extensions to existing buildings.

This thesis analyzed the effect of pumping and the thereby exerted pressure on the material properties and started building a first analytical approach to estimate the feasible building speeds and construction heights for lightweight aggregate concrete extrusion, incorporating also cross-effects of the pumping and manufacturing process on the material.

The experimental research is based on investigations on three scales:

1. on a micro scale the condition and amount of lightweight aggregates,
2. on a meso scale the fresh and hardened concrete properties, and
3. on a macro scale the pumpability and buildability of lightweight aggregate concrete.

Among the fresh concrete properties (meso scale), dynamic rheological measurements were conducted with regard to workability and pumpability. Furthermore, static rheological measurements as well as compression tests were carried out to determine static yield stress and Young's modulus, respectively, as a base for buildability calculations. The hardened concrete properties of interest are the compressive strength, the flexural strength and the thermal conductivity of the material.

On the micro scale it was found, that the water absorption and pore filling increase with pressure and time, leading to a lower effective water-to-binder ratio in the surrounding cement matrix

and a higher density of the lightweight aggregate concrete, see Figure 5.1. Furthermore, with low pre-saturation times for the lightweight aggregates (e.g., 5 minutes) and high pressure, surface destruction and ingress of cement paste into the lightweight aggregates were observed under the microscope. An estimate for the destruction of the lightweight aggregates was achieved by washing-out of the lightweight aggregates from a defined amount of concrete and comparing the target and actual volume of aggregates as well as by counting of the lightweight aggregates in hardened concrete samples.

Caused by the increased water absorption and by the slight surface destruction accompanied by ingress of cement paste into the lightweight aggregates, the density of the lightweight aggregate concrete changed approx. 15-25 % for mixtures with lightweight aggregates pre-saturated only for 5 minutes. A part of the changes is reversible over long time periods as the water absorbed by the lightweight aggregates can be released over time (Figure 5.1). Thus, the changes are affecting the fresh properties, but less the hardened concrete properties. However, there are also irreversible changes, especially due to ingress of cement paste into lightweight aggregates, leading to a difference in material properties also in hardened and oven-dry state, see Figure 5.1.

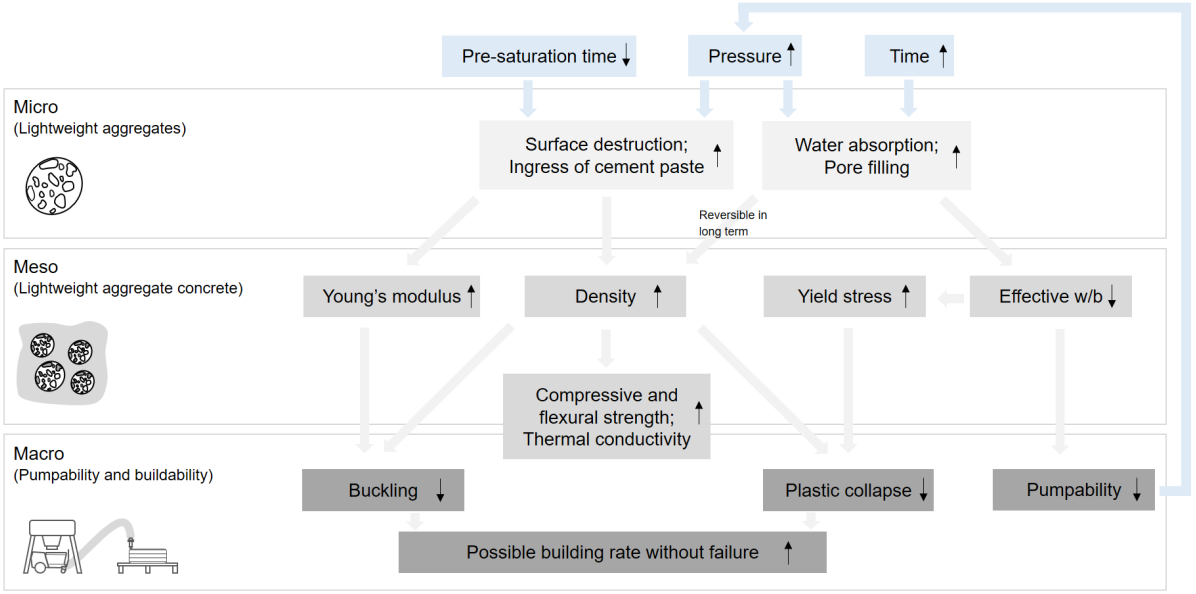

FIGURE 5.1: Correlations of results assigned to the individual scales (micro, meso and macro) of this thesis

An increase in compressive and flexural strength as well as in Young's modulus was detected with increasing pump frequency due to the changes induced by pumping pressure. The thermal conductivity increases as well with increasing pump frequency (Figure 5.1). This is however not

beneficial for the insulation capacity of the material. Therefore, a compromise between strength and thermal conductivity must be found.

With regard to the fresh material properties, the rheological investigations on lightweight aggregate concrete with and without pressure revealed an increase in yield stress due to pressure application. Especially in mixtures with lightweight aggregates of 1-2 mm grain size, a sudden increase of material resistance with increasing pressure was detected. Since the positive effect of the yield stress increase has a stronger influence on the buildability than the negative effect of the density increase, the buildability is improved by the changes during the pumping process. Thus, possible building rates without failure are higher with the material after (moderate) pumping, than with the material before pumping. It was shown that this is true both, with regard to buckling failure and to plastic collapse (Figure 5.1).

Furthermore, the changes starting at the micro level also affect the pumpability. Due to the water absorption of the lightweight aggregates and the accompanying reduced effective water-to-binder ratio in the cement paste (meso level), the required pressure for a constant flow rate and the risk of blockages increase. Increasing pump frequency leads to increasing pressure and temperature. The increasing pressure again leads to higher water absorption and ingress of cement paste, see Figure 5.1.

It was shown that pre-saturating the aggregates with water over a few days enables to reduce the water absorption during pumping, the surface destruction, and the ingress of cement paste into the aggregates. Thus, the change in density is also reduced for pre-saturated samples (only approx. 2-5% when pre-saturated over 2-9 days while it was approx. 20% for mixtures pre-saturated only for 5 minutes). It was found that increased pre-saturation time facilitates pumpability. On the other side, it is not beneficial for buildability as explained before.

Current models underestimate the buildability of lightweight aggregate concrete by ignoring the effects achieved during pumping. Thus, predictions on basis of the fresh material properties forecast the failure to happen long before the failure happens in experiments. The models lead to a major underestimation of not-pumped lightweight aggregate concrete and to a slight underestimation of lightweight aggregate concrete when based on pumped material. Even though predictions based on pumped material properties are much closer to reality, these involve a great deal of effort, since a large amount of material must be produced and pumped at least once. Furthermore, the rheology must be investigated process-parallel and the evaluation must then

be carried out either process-parallel or post-process. All in all a strenuous undertaking. On top, little or no information can be used for the running extrusion process.

Within this thesis a new model and associated test regime was developed integrating the influence of (pumping) pressure into the buildability calculations. Evidence is provided on a case study that it is possible to calculate the failure on basis of the not-pumped material in combination with a small pressure test. The predictions are possible for different pressure levels. This approach significantly reduces the required effort and allows an assessment of the suitability of the material for extrusion as well as the required process parameters to be made before starting the extrusion or pumping process. Thus, the approach can contribute to the further development of various materials for extrusion.

In view of future research, some challenges and promising approaches were identified. The main input parameters for buildability calculations are the yield stress and its evolution over time. Conventional test methods for rheological properties reach their limits in terms of measuring range not only for normal weight concrete but also for lightweight concrete, especially over longer periods and at higher pressures. Thus, an important area for further research is the continued development of investigation methods for the analysis of rheological properties in stiff materials over long time periods. Both, for classical rheological investigations and for investigations under pressure, it is important for the quality of predictions that higher yield stresses can be recorded.

With regard to rheology, reducing the conflicting requirements for pumpability and buildability would enhance the achievable building rate and material properties. Especially, reducing the conveying length is promising for lightweight aggregate concrete extrusion as pumpability is the critical factor. Conducting further research with regard to gradation and short conveying distances can increase the potential in a way, that it enables a rethinking of components, especially of wall structures, in terms of multi-functional, resource-efficient building. Efficient structural and thermal designs can be realized on basis of an optimized virtual model. Placing material only where it is needed for the desired functionality leads to a reduction of resource consumption (Salet and Wolfs, 2016; Wangler et al., 2016; Agustí-Juan et al., 2017; Agustí-Juan and Habert, 2017; de Schutter et al., 2018). Combining the low thermal conductivity of lightweight aggregate concrete with a well-designed layout of the concrete strands including further porosity in the overall wall structure (see e.g., (Li Wang et al., 2020; Dielemans et al., 2021; Ramakrishnan et al., 2021; Briels et al., 2022)), enables to combine low resource consumption with good insulation properties. Furthermore, by integrating channels for building services already during the process, subtractive processes can be reduced leading to less waste production—equally as the

omission of formwork. In future research this should be combined with reduction of the clinker content in the concrete for extrusion so that the savings in resources are not offset again by high clinker content which is responsible for the major part of CO_2 emissions in the concrete production. In this regard, the calculation of a life cycle assessment would also be interesting to compare the process to conventional building processes in a global setting. In terms of functional integration, future research should further evaluate the potential for additive manufacturing created by heat-insulating, heat-storing, moisture-regulating, and sound-insulating properties of lightweight concrete.

With respect to up-scaling, it was shown that the material developed in this thesis and the associated research project is suitable for the construction of single-story buildings by producing demonstrators (see Figure 5.2 and Matthäus et al. (2021)). For multistory buildings with lightweight aggregate concrete, solutions for reinforcement as well as further investigations on material development should be carried out and with regard to the control on the building site, e.g., real-time measurements, in-line analysis of rheology, feedback loops and automated process control are of major interest and should be addressed in an interdisciplinary team.

FIGURE 5.2: Extruded lightweight aggregate concrete elements

Appendix

Table A.1 gives an overview on the composition of mixtures M.PS 5min and S.PS 5min.

TABLE A.1
Mix design for mixtures M.PS 5min and S.PS 5min

This table gives an overview on the mix design of the mixtures M.PS 5min and S.PS 5min for a concrete volume of 1 dm^3.

	Mixture	M.PS 5min [g/dm^3]	S.PS 5min [g/dm^3]
Cement paste	Limestone cement	558	558
	Silica fume	62	62
	First water addition	209	209
	Second water addition	105	105
Aggregates	LA 0.1-0.3 mm	111	111
	LA 0.25-0.5 mm	78	78
	LA 0.5-1.0 mm	58	58
	LA 1.0-2.0 mm	74	74
Admixtures	PCE 0.45 wt.%	2.8	2.8
	Thixotropy enhancing agent 0.5 g/l water	0.1	-
	Air void stabilizer 1.0 wt.%	6.2	-

Table A.2 summarizes the timing for the static measurements described in Section 3.7.1.

TABLE A.2
Timing of static measurements after addition of mixing water

This table describes static rheological measurements after the mixing procedure.
The timeline refers to the addition of the mixing water.

	Timeline [min : s]	Duration [min : s]
Mixing process see Table 3.4	0:00	-
Temperature measurement	2:30	0:30
Filling of the conus for slump test	3:00	1:30
Slump test	4:30	1:30
Cleaning of test equipment and preparation	6:00	5:00
Homogenization (mixing)	11:00	1:00
Filling of the cup of the rheometer	12:00	1:00
Mounting of the cup in the rheometer and activation	13:00	1:33
Temperature measurement in parallel	14:00	0:30
Pre-shear	14:33	1:24
Beginning of resting time	15:57	0:30
First shear rate peak	16:27	0:06
Alternating shear and rest phases	16:33	min. 25:00
End of static measurements		

The timeline for the pumping tests (Section 3.6.3) including the preparation of samples for further tests is compiled in Table A.3.

Table A.3
Timing of pumping tests after addition of mixing water

This table describes the real pumping tests procedure. The timeline refers to the addition of the mixing water. Some of the tests described in the sections before are conducted on the material before pumping (b.p.) and after pumping (a.p.) in order to determine the evolution of material characteristics during pumping.

		Timeline [min : s]
Start	Preparation of laboratory and materials	
	Lubricating of the hose (pre-wetting with water or primer)	
	Pre-wetting of aggregates and mixing see Table 3.4	
	Addition of mixing water and PCE and mixing according to Table 3.4	0:00
Before pumping	Temperature measurement	4:00
	Fresh concrete density, set material aside for sieving	5:00
	Production of 3 prisms with material before pumping	5:00
	Transfer of 15 l into the filing container of the pump	7:00
	Start pressure recording	10:00
	Start pumping at 7.3 Hz	10:00
Rheology b.p.	Homogenization of the material in the mixer for 1 min	11:00
	Filling of the cup of the rheometer	12:00
	Mounting of the cup in the rheometer and activation	13:00
	Temperature measurement in parallel	14:00
	Pre-shear	14:33
	Beginning of descending steps	15:00
	Slump test in parallel	15:00
After pumping	Determine flow rate three times, each 60 seconds at 7.3 Hz	13:00
	Temperature measurement in parallel	14:00
	Fresh concrete density, set material aside for sieving	15:00
	Determine flow rate three times, each 60 seconds at 15.6 Hz	17:00
	Temperature measurement in parallel	18:00
	Fresh concrete density, set material aside for sieving	19:00
	Determine flow rate three times, each 60 seconds at 26.2 Hz	21:00
	Temperature measurement in parallel	22:00
	Fresh concrete density, set material aside for sieving	23:00
Rheology a.p.	Filling of the cup of the rheometer	19:00
	Mounting of the cup in the rheometer and activation	20:00
	Temperature measurement in parallel	21:00
	Pre-shear	21:33
	Beginning of descending steps	22:00
Aggregates	Production of min. 3 prisms each with material after pumping	25:00
	Sieving of 1 l material before pumping	25:00
	Sieving of 1 l material after pumping	25:00
	End of tests	35:00

The timeline for the so-called "cumulative pressure tests" described in Section 3.6.4 is detailed in Table A.4.

Table A.4
Timing of cumulative pressure tests in the pressure cell after addition of mixing water

This table describes the pressure cell test procedure to evaluate the changes in torque during pressure application. The timeline refers to the addition of the mixing water. The tests are conducted on material without pressure application ($\bar{p}$) and with pressurization (p) in order to determine the evolution of material characteristics during pressure application. Furthermore, it contains rheological measurements at constant shear rate (const.) at increasing pressure levels (incr. pressure) and dynamic rheological measurements (dyn.).

		Timeline [min : s]
Start	Preparation of laboratory, rheometer and materials	
	Pre-wetting of aggregates, addition of cement and mixing see Table 3.4	
	Addition of mixing water and PCE and mixing see Table 3.4	0:00
Preparation	Temperature measurement	2:30
	Homogenization of the material in the mixer for 1 min	11:00
	Set material aside for tests on material without pressure	12:00
	Filling of the cup of the rheometer	12:30
	Mounting of the cup in the rheometer	15:00
Const., incr. pressure	Activation of the constant shear profile	16:00
	Beginning of pre-shear	16:52
	Beginning of measurement at constant shear rate, ambient pressure	17:00
	Increase of pressure by 2 bar (3 bar)	22:00
	Increase of pressure by 2 bar (5 bar)	27:00
	Increase of pressure by 2 bar (7 bar)	32:00
	Increase of pressure by 2 bar (9 bar)	37:00
	Increase of pressure by 2 bar (11 bar)	42:00
	End of measurements, automatic data saving	47:00
Dyn., p	Stripping off the material sticking to the vane device	50:00
	Loading and activation of the dynamic profile	51:00
	Beginning of pre-shear	51:52
	Beginning of descending steps	52:00
	End of measurements, automatic data saving	54:00
Dyn., $\bar{p}$	Empty the cup of the rheometer	55:00
	Filling of the cup of the rheometer with the material set aside	56:00
	Mounting of the cup in the rheometer and activation	57:00
	Beginning of pre-shear	57:52
	Beginning of descending steps	58:00
	End of measurements, automatic data saving	60:00

The timeline for the so-called "static pressure tests" described in Section 3.6.4 is detailed in Table A.5.

TABLE A.5
Timing of static pressure tests in the pressure cell after addition of mixing water

This table describes the pressure cell test procedure to evaluate the increase in shear stress due to pressure. The timeline refers to the addition of the mixing water. The tests are conducted on fresh lightweight concrete at increasing pressure levels of 1 bar (atmospheric pressure), 3, 5, 7, 9 and 11 bar each.

		Timeline [min : s]
Start	Preparation of laboratory, rheometer and materials	
	Pre-wetting of aggregates, addition of cement and mixing see Table 3.4	
	Addition of mixing water and PCE and mixing according to Table 3.4	0:00
Preparation	Temperature measurement	2:30
	Homogenization of the material in the mixer for 1 min	11:00
	Set material aside for tests on material without pressure	12:00
	Filling of the cup of the rheometer	12:30
	Mounting of the cup in the rheometer	15:00
Measurements	Activation of the constant shear profile	16:00
	Beginning of pre-shear	16:52
	Beginning of measurement at constant shear rate, ambient pressure	17:00
	Increase of pressure	19:00
	Removal of pressure and resting for 1.5 minutes	19:30
	End of measurements, automatic data saving	21:00

In addition to the tests described in Table A.5, long-running static rheological measurements are conducted in the same device as the pressure tests at atmospheric pressure in order to combine them for the newly developed buildability prediction approach, see Table A.6.

TABLE A.6
Timing of static rheological measurements in the pressure cell

		Timeline [min : s]
Start	Preparation of laboratory, rheometer and materials	
	Pre-wetting of aggregates, addition of cement and mixing see Table 3.4	
	Addition of mixing water and PCE and mixing according to Table 3.4	0:00
Preparation	Temperature measurement	2:30
	Homogenization of the material in the mixer for 1 min	11:00
	Set material aside for tests on material without pressure	12:00
	Filling of the cup of the rheometer	12:30
	Mounting of the cup in the rheometer	15:00
Measurements	Activation of the constant shear profile	16:00
	Beginning of pre-shear	16:52
	Beginning of dynamic rheological measurement, ambient pressure	17:00
	Automated beginning of static rheological measurement incl. pre-shear	19:00
	Automated beginning of dynamic rheological measurement incl. pre-shear	109:00
	End of measurements, automatic data saving	111:00

The test setup for the further vane tests (see Section 3.7.2) is summarized in Table A.7. It contains two types of tests which are run in parallel when conducting pumping tests or extruding lightweight concrete elements.

TABLE A.7
Timing of further yield stress tests on material after pumping

This table describes the test procedure for the evaluation of static yield stress of material after pumping. The timeline refers to the addition of the mixing water.

		Timeline [min : s]
Preparation	Preparation of laboratory and materials	
	Lubricating of the hose (pre-wetting with sinthetic primer)	
	Pre-wetting of aggregates and mixing see Table 3.4	
	Addition of mixing water and PCE, mixing according to Table 3.4	0:00
	Temperature measurement	4:00
	Transfer of 15 l into the filling container of the pump	7:00
	Start pressure recording	10:00
	Start pumping	10:00
ICAR	Filling of the cup of the ICAR-rheometer	15:00
	Mounting of the measuring device and activation	20:00
	Temperature measurement in parallel	20:30
	Pre-shear for 10 seconds	20:50
	Beginning of first static measurement in the ICAR-rheometer (2 minutes at rest)	23:00
	Static measurement in the ICAR-rheometer for 6 seconds (8 minutes at rest)	29:00
	Static measurement in the ICAR-rheometer for 6 seconds (12 minutes at rest)	33:00
	Static measurement in the ICAR-rheometer for 6 seconds (20 minutes at rest)	41:00
	Static measurement in the ICAR-rheometer for 6 seconds (30 minutes at rest)	51:00
	Static measurement in the ICAR-rheometer for 6 seconds (45 minutes at rest)	66:00
	Static measurement in the ICAR-rheometer for 6 seconds (60 minutes at rest)	81:00
Hand Vane	In parallel preparation of buckets with material for the hand vane tests	17:00
	Insertion of six hand vane devices over 30 seconds	20:30
	Determination of $M_h(t_1)$ with hand vane device (30 minutes at rest)	51:00
	Determination of $M_h(t_2)$ with hand vane device (60 minutes at rest)	81:00
	Determination of $M_h(t_3)$ with hand vane device (80 minutes at rest)	101:00
	Determination of $M_h(t_4)$ with hand vane device (90 minutes at rest)	111:00
	Determination of $M_h(t_5)$ with hand vane device (120 minutes at rest)	141:00
	Determination of $M_h(t_6)$ with hand vane device (150 minutes at rest)	171:00
	End of tests	173:00

The timing for the uniaxial compressive tests (Section 3.7.3) is summarized in Table A.8. The normal specimen are labeled with an A and the time with respect to the beginning of the measurements. The pressurized specimen are labeled with a C and the time with respect to the beginning of the measurements.

TABLE A.8
Timing of uniaxial compression tests after addition of mixing water

This table describes the compression test procedure. The timeline refers to the addition of the mixing water. The tests are conducted on material without pressure application (labeled $\bar{p}$) and with pressurization (labeled p).

		Timeline [min : s]
Start	Preparation of laboratory, formworks, rheometer and materials	
	Pre-wetting of aggregates, addition of cement and mixing see Table 3.4	
	Addition of mixing water and PCE and mixing according to Table 3.4	0:00
Setup	Temperature measurement	2:30
	Homogenization of the material in the mixer for 1 min	3:30
	Filling of the cylindrical formworks, compaction at 2x 10 s at 30 Hz	4:30
	Start compression test with specimen $\bar{p}0$	10:00
	Filling of the cup of the rheometer	12:30
	Mounting of the cup in the rheometer and activation	14:27
	Beginning of static measurements	15:00
Compression tests	Start compression test with specimen $\bar{p}15$	25:00
	Pressurize material mechanically at 5 kN for 10 minutes	30:00
	Fill two formworks with pressurized material	40:00
	Start compression test with specimen $\bar{p}45$	55:00
	Start compression test with specimen $\bar{p}60$	70:00
	Start compression test with specimen $\bar{p}90$	100:00
	Start compression test with specimen $\bar{p}120$	130:00
	End of measurements, automatic data saving	135:00
Start	Pre-wetting of aggregates, addition of cement and mixing see Table 3.4	
	Addition of mixing water and PCE and mixing according to Table 3.4	0:00
Setup	Temperature measurement	2:30
	Homogenization of the material in the mixer for 1 min	3:30
	Pressurize material mechanically at 5 kN for 10 minutes	5:00
	Filling of the cup of the rheometer	12:30
	Mounting of the cup in the rheometer and activation	14:27
	Beginning of static measurements	15:00
Tests	Filling of the cylindrical formworks	15:00
	Start compression test with specimen p2	17:00
	Pressurize material mechanically at 5 kN for 10 minutes	30:00
	Fill formwork with pressurized material	42:00
	Start compression test with specimen p45	60:00
	Start compression test with pressurized specimen p90	105:00
	End of measurements, automatic data saving	110:00

Figure A.3 shows the temperature development for the lightweight aggregate concrete mixes mentioned in Section 4.3. For the reference mixtures M.PS 5min and S.PS 5min, temperature increases with increasing duration of pumping while for the longer pre-saturated mixtures S.PS 2d, S.PS 7d and M.PS 9d, temperature is almost constant over 25 minutes.

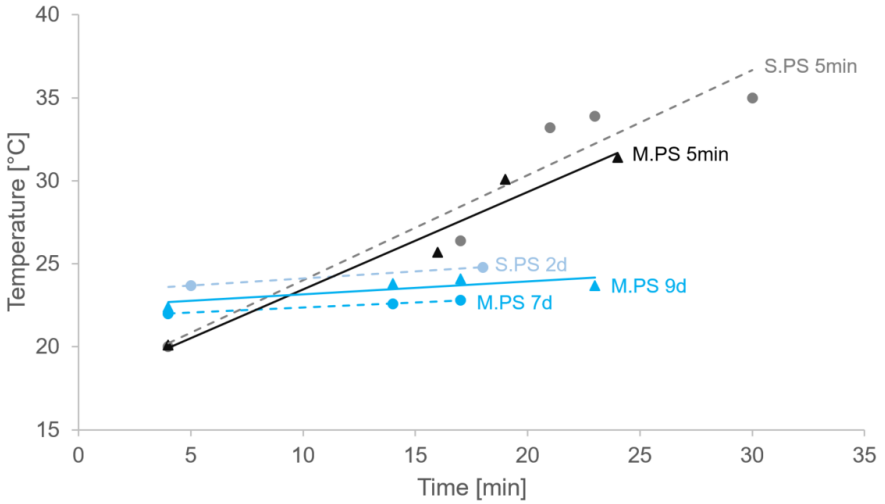

FIGURE A.3: Temperature development during pumping for reference mixtures M.PS 5min and S.PS 5min and mixtures with longer pre-saturation S.PS 2d, S.PS 7d and M.PS 9d

Bibliography

Y. A. Abebe. *Flowable and stable concrete: Design, Characterization and Performance Evaluation.* Dissertation, Leibniz Universität Hannover, 2017.

I. Agustí-Juan and G. Habert. Environmental design guidelines for digital fabrication. *Journal of Cleaner Production*, 142:2780–2791, 2017.

I. Agustí-Juan, F. Müller, N. Hack, T. Wangler, and G. Habert. Potential benefits of digital fabrication for complex structures: Environmental assessment of a robotically fabricated concrete wall. *Journal of Cleaner Production*, 154:330–340, 2017.

P.-C. Aitcin and R. J. Flatt. *Science and technology of concrete admixtures.* Woodhead Publishing, 2015.

O. Arkhipkina, B. Schuler, and M. Stipetic. Impact of the pumping process on the properties of lightweight concrete. *IOP Conference Series: Materials Science and Engineering*, 615:012015, 2019.

ASTM D2166. Test Method for Unconfined Compressive Strength of Cohesive Soil, 2017.

H. Aurich. *Kleine Leichtbetonkunde.* Bauverlag GmbH, Wiesbaden, 1971. ISBN 0 444 871403.

H. A. Barnes, J. F. Hutton, and K. Walters. *An introduction to rheology*, volume 3. Elsevier, 1989.

H. Bauer and W. Poppy. *Grundlagen für das Pumpen von Leichtbeton: Untersuchungen über den Einfluß des Wasserhaushalts leichter poröser Zuschläge auf die Pumpwilligkeit von Leichtbeton.* Hauptverband der Deutschen Bauindustrie, 1974.

H. Bessaies-Bey, R. Baumann, M. Schmitz, M. Radler, and N. Roussel. Organic admixtures and cement particles: Competitive adsorption and its macroscopic rheological consequences. *Cement and Concrete Research*, 80:1–9, 2016.

P. Billberg. Form pressure generated by self-compacting concrete. In *Proceedings of the 3rd international RILEM symposium on self-compacting concrete, Reykjavik, Iceland*, pages 271–280, 2003.

M. Biscoping and M. Beck. B21-Betonieren bei extremen Temperaturen. *Zement-Merkblatt Betontechnik*, B21(12), 2014.

F. Bos, R. Wolfs, Z. Ahmed, and T. Salet. Additive manufacturing of concrete in construction: Potentials and challenges of 3D concrete printing. *Virtual and Physical Prototyping*, 11(3): 209–225, 2016.

D. Briels, S. Kollmannsberger, F. Leithner, C. Matthäus, A. S. Nouman, O. Oztoprak, and E. Rank. Thermal optimization of additively manufactured lightweight concrete wall elements with internal cellular structure through simulations and measurements. *Buildings*, 12(7):1023, 2022.

R. D. Browne and P. B. Bamforth. Tests to establish concrete pumpability. *Journal Proceedings*, 74(5):193–203, 1977.

C. Brumaud, R. Baumann, M. Schmitz, M. Radler, and N. Roussel. Cellulose ethers and yield stress of cement pastes. *Cement and Concrete Research*, 55:14–21, 2014.

R. A. Buswell, W. L. Da Silva, F. P. Bos, H. R. Schipper, D. Lowke, N. Hack, H. Kloft, V. Mechtcherine, T. Wangler, and N. Roussel. A process classification framework for defining and describing Digital Fabrication with Concrete. *Cement and Concrete Research*, 134:106068, 2020.

D. D. Camacho, P. Clayton, W. J. O'Brien, C. Seepersad, M. Juenger, R. Ferron, and S. Salamone. Applications of additive manufacturing in the construction industry–A forward-looking review. *Automation in Construction*, 89:110–119, 2018.

M. Choi, N. Roussel, Y. Kim, and J. Kim. Lubrication layer properties during concrete pumping. *Cement and Concrete Research*, 45:69–78, 2013.

M. S. Choi, S. B. Park, and S.-T. Kang. Effect of the mineral admixtures on pipe flow of pumped concrete. *Journal of Advanced Concrete Technology*, 13(11):489–499, 2015.

G. de Schutter, K. Lesage, V. Mechtcherine, V. N. Nerella, G. Habert, and I. Agusti-Juan. Vision of 3D printing with concrete — Technical, economic and environmental potentials. *Cement and Concrete Research*, 112:25–36, 2018.

Dennert Poraver GmbH. Poraver - Technische Daten, 2018. URL https://www.poraver.com/technische-daten-poraver/.

G. Dielemans, D. Briels, F. Jaugstetter, K. Henke, and K. Dörfler. Additive Manufacturing of Thermally Enhanced Lightweight Concrete Wall Elements with Closed Cellular Structures. *Journal of Facade Design and Engineering*, 9(1), 2021.

L. Domagała. The effect of lightweight aggregate water absorption on the reduction of water-cement ratio in fresh concrete. *Procedia Engineering*, 108:206–213, 2015. ISSN 18777058.

N. Ducoulombier, P. Carneau, R. Mesnil, L. Demont, J.-F. Caron, and N. Roussel. "The Slug Test": Inline Assessment of Yield Stress for Extrusion-Based Additive Manufacturing. In *RILEM International Conference on Concrete and Digital Fabrication*, pages 216–224, 2020.

D. Falliano, D. de Domenico, G. Ricciardi, and E. Gugliandolo. 3D-printable lightweight foamed concrete and comparison with classical foamed concrete in terms of fresh state properties and mechanical strength. *Construction and Building Materials*, 254:119271, 2020.

S. Fataei, E. Secrieru, V. Mechtcherine, and N. Roussel. A first-order physical model for the prediction of shear-induced particle migration and lubricating layer formation during concrete pumping. *Cement and Concrete Research*, 147:106530, 2021. ISSN 00088846.

T. Faust. *Leichtbeton im Konstruktiven Ingenieurbau.* Bauingenieur-Praxis. Ernst & Sohn, Berlin, 2003. ISBN 3433016135.

P. Feng, X. Meng, J.-F. Chen, and L. Ye. Mechanical properties of structures 3D printed with cementitious powders. *Construction and Building Materials*, 93:486–497, 2015.

D. Feys. *Interactions between rheological properties and pumping of self-compacting concrete.* Dissertation, Ghent University, 2009.

D. Feys, G. de Schutter, R. Verhoeven, and K. H. Khayat. Similarities and differences of pumping conventional and self-compacting concrete. In *Design, Production and Placement of Self-Consolidating Concrete*, pages 153–162. Springer, 2010.

D. Feys, G. de Schutter, and R. Verhoeven. Parameters influencing pressure during pumping of self-compacting concrete. *Materials and Structures*, 46(4):533–555, 2013.

D. Feys, K. H. Khayat, A. Perez-Schell, and R. Khatib. Prediction of pumping pressure by means of new tribometer for highly-workable concrete. *Cement and Concrete Composites*, 57: 102–115, 2015.

D. Feys, G. de Schutter, K. H. Khayat, and R. Verhoeven. Changes in rheology of self-consolidating concrete induced by pumping. *Materials and Structures*, 49(11):4657–4677, 2016a.

D. Feys, K. H. Khayat, and R. Khatib. How do concrete rheology, tribology, flow rate and pipe radius influence pumping pressure? *Cement and Concrete Composites*, 66:38–46, 2016b.

L. Forstmaier and C. Matthäus. *Einfluss der Vorsättigung von Leichtzuschlägen auf die Rohdichteveränderung im Pumpprozess*. Kurzbericht, Technische Universität München, Centrum Baustoffe und Materialprüfung, München, 2020.

F. J. Galindo-Rosales, F. J. Rubio-Hernández, and A. Sevilla. An apparent viscosity function for shear thickening fluids. *Journal of Non-Newtonian Fluid Mechanics*, 166(5-6):321–325, 2011.

M. Haist. *Zur Rheologie und den physikalischen Wechselwirkungen bei Zementsuspensionen*. Dissertation, KIT Karlsruhe Scientific Publishing, 2010.

M. Haist and H. Müller. Optimization of the pumpability of self-compacting lightweight concrete. *Proceedings of the 4th International RILEM Symposium on Self-Compacting Concrete, Chicago*, pages 195–202, 2005.

M. Haist, V. Mechtcherine, H. Beitzel, and H. S. Müller. Retrofitting of building structures using pumpable self-compacting lightweight concrete. In *Proceedings of the 3rd international symposium on self-compacting concrete*, pages 776–785, 2003.

K. Henke. *Additive Baufertigung durch Extrusion von Holzleichtbeton*. Dissertation, Technische Universität München, 2016.

K. Henke, D. Talke, and S. Winter. Additive Manufacturing of Building Elements by Extrusion of Wood Concrete. *World Conference on Timber Engineering*, 2016.

K. Henke, D. Talke, and S. Winter. Multifunctional Concrete-Additive Manufacturing by the Use of Lightweight Concrete. In *Proceedings of IASS Annual Symposia*, volume 2017, pages 1–9, 2017.

K. Henke, D. Talke, and C. Matthäus. Additive Manufacturing by Extrusion of Lightweight Concrete - Strand Geometry, Nozzle Design and Layer Layout. *Proceedings of the 2nd RILEM International Conference on Concrete and Digital Fabrication*, pages 906–915, 2020.

V. Hermann. Zum Problem der Pumpbarkeit von Leichtbeton. *Beton*, 24(9), 1974.

S. Jacobsen, J. H. Mork, S. F. Lee, and L. Haugan. Pumping of concrete and mortar - State of the art. *COIN Project Report 5*, pages 1–44, 2008.

J. H. Jeong, K. P. Jang, C. K. Park, S. H. Lee, and S. H. Kwon. Effect of admixtures on pumpability for high-strength concrete. *ACI Materials Journal*, 113(3):323, 2016.

S. P. Jiang, J. C. Mutin, and A. Nonat. Studies on mechanism and physico-chemical parameters at the origin of the cement setting: I. The fundamental processes involved during the cement setting. *Cement and Concrete Research*, 25(4):779–789, 1995.

D. Kaplan. *Pompage de bétons*. Dissertation, Laboratoire Central des Ponts et Chaussees, 2001.

D. Kaplan, F. de Larrard, and T. Sedran. Avoidance of blockages in concrete pumping process. *ACI Materials Journal*, 102(3):183, 2005.

K. Kasten. *Gleitrohr-Rheometer, Ein Verfahren zur Bestimmung der Fließeigenschaften von Dickstoffen in Rohrleitungen*. Dissertation, TU Dresden, 2010.

A. Kazemian, X. Yuan, E. Cochran, and B. Khoshnevis. Cementitious materials for construction-scale 3D printing: Laboratory testing of fresh printing mixture. *Construction and Building Materials*, 145:639–647, 2017.

E. Keita, H. Bessaies-Bey, W. Zuo, P. Belin, and N. Roussel. Weak bond strength between successive layers in extrusion-based additive manufacturing: measurement and physical origin. *Cement and Concrete Research*, 123:105787, 2019.

K. H. Khayat and N. Mikanovic. Viscosity-enhancing admixtures and the rheology of concrete. In *Understanding the rheology of concrete*, pages 209–228. Elsevier, 2012.

B. Khoshnevis. Contour crafting-state of development. In *Solid Freeform Fabrication Proceedings*, pages 743–750, 1999.

E. P. Koehler and D. W. Fowler. *Development of a portable rheometer for fresh Portland Cement concrete*. Research Report ICAR 105-3F, International Center for Aggregates Research, Austin, 2004.

K. Kovler and N. Roussel. Properties of fresh and hardened concrete. *Cement and Concrete Research*, 41(7):775–792, 2011.

T. Kränkel, D. Lowke, and C. Gehlen. Optimization of a Semi-Flowable SCC for the Application in horizontal Slipform Constructions. In *SCC 2010, Proceedings of the 6th International Rilem Symposium on Self-Compacting Concrete*, Berlin, 2010. Springer.

I. M. Krieger. Shear rate in the Couette viscometer. *Transactions of the Society of Rheology*, 12 (1):5–11, 1968.

J. Kruger, S. Zeranka, and G. van Zijl. 3D concrete printing: a lower bound analytical model for buildability performance quantification. *Automation in Construction*, 106:102904, 2019a.

J. Kruger, S. Zeranka, and G. van Zijl. An ab initio approach for thixotropy characterisation of (nanoparticle-infused) 3D printable concrete. *Construction and Building Materials*, 224: 372–386, 2019b.

J. Kruger, S. Zeranka, and G. van Zijl. A rheology-based quasi-static shape retention model for digitally fabricated concrete. *Construction and Building Materials*, 254:119241, 2020.

R. Lapasin, A. Papo, and S. Rajgelj. The phenomenological description of the thixotropic behaviour of fresh cement pastes. *Rheologica Acta*, 22:410–416, 1983.

T. T. Le, S. A. Austin, S. Lim, R. A. Buswell, A. G. F. Gibb, and T. Thorpe. Mix design and fresh properties for high-performance printing concrete. *Materials and Structures*, 45(8): 1221–1232, 2012a.

T. T. Le, S. A. Austin, S. Lim, R. A. Buswell, R. Law, A. Gibb, and T. Thorpe. Hardened properties of high-performance printing concrete. *Cement and Concrete Research*, 42(3):558–566, 2012b.

T. Lecompte and A. Perrot. Non-linear modeling of yield stress increase due to SCC structural build-up at rest. *Cement and Concrete Research*, 92:92–97, 2017.

Li Wang, H. Jiang, Z. Li, and G. Ma. Mechanical behaviors of 3D printed lightweight concrete structure with hollow section. *Archives of Civil and Mechanical Engineering*, 20(1):1–17, 2020.

S. Lim, R. A. Buswell, T. T. Le, S. A. Austin, A. Gibb, and T. Thorpe. Developments in construction-scale additive manufacturing processes. *Automation in Construction*, 21:262–268, 2012.

G. Liu, L. Chen, W. Cheng, and Y. Huang. Research on Pump Primers for Friction Reduction of Wet-Mix Shotcrete Based on Precreating Lubricating Layer. *Advances in Materials Science and Engineering*, 2017(3):1–12, 2017.

E. Lloret, A. R. Shahab, M. Linus, R. J. Flatt, F. Gramazio, M. Kohler, and S. Langenberg. Complex concrete structures: merging existing casting techniques with digital fabrication. *Computer-Aided Design*, 60:40–49, 2015.

D. Lowke. *Sedimentationsverhalten und Robustheit Selbstverdichtender Betone*. Dissertation, Technische Universität München, 2013.

M. Lusche. *Beitrag zum Bruchmechanismus von auf Druck beanspruchtem Normal-und Leichtbeton mit geschlossenem Gefüge*. Beton-Verlag, 1972.

D. Marchon, S. Kawashima, H. Bessaies-Bey, S. Mantellato, and S. Ng. Hydration and rheology control of concrete for digital fabrication: Potential admixtures and cement chemistry. *Cement and Concrete Research*, 112:96–110, 2018.

R. Mark and P. Hutchinson. On the Structure of the Roman Pantheon. *The Art Bulletin*, 68 (1):24–34, 1986.

A. Martínez-Rocamora, R. García-Alvarado, E. Casanova-Medina, L. F. González-Böhme, and F. Auat-Cheein. Parametric Programming of 3D Printed Curved Walls for Cost-Efficient Building Design. *Journal of Construction Engineering and Management*, 146(5):04020039, 2020.

C. Matthäus, D. Weger, T. Kränkel, L. S. Carvalho, and C. Gehlen. Extrusion of Lightweight Concrete: Rheological Investigations. In *Rheology and Processing of Construction Materials*, pages 409–416. Springer, 2019.

C. Matthäus, D. Back, D. Weger, T. Kränkel, J. Scheydt, and C. Gehlen. Effect of Cement Type and Limestone Powder Content on Extrudability of Lightweight Concrete. *Proceedings of the 2nd RILEM International Conference on Concrete and Digital Fabrication*, pages 312–322, 2020.

C. Matthäus, K. Henke, D. Talke, and T. Kränkel. *Leichtbeton-3D-Druck – Additive Fertigung von multifunktionalen, monolithischen Wandelementen durch Extrusion von Leichtbeton.* BBSR-Online-Publikation 05/2021, Bonn, 2021.

V. Mechtcherine, V. N. Nerella, and K. Kasten. Testing pumpability of concrete using Sliding Pipe Rheometer. *Construction and Building Materials*, 53:312–323, 2014.

L. K. Mettler, F. K. Wittel, R. J. Flatt, and H. J. Herrmann. Evolution of Strength and Failure of SCC during Early Hydration. *Cement and Concrete Research*, 89:288–296, 2016.

T. Mezger. *Das Rheologie Handbuch: Für Anwender von Rotations- und Oszillations-Rheometern*. Vincentz network, Hannover, 2016. ISBN 9783866306332.

G. Neroth and D. Vollenschaar. *Wendehorst Baustoffkunde: Grundlagen-Baustoffe-Oberflächenschutz*. Springer, 2011.

A. Neunast and F. Lange. *Leichtbeton Handbuch*. Verlag Bau und Technik, Düsseldorf, 2001. ISBN 9783764004071.

A. Nonat, J. C. Mutin, X. Lecoq, and S. P. Jiang. Physico-chemical parameters determining hydration and particle interactions during the setting of silicate cements. *Solid state ionics*, 101:923–930, 1997.

F. Nübling. *Die Förderung des Frischbetons durch Rohre*. Dissertation, TU Berlin, 1971.

M. Palacios and R. J. Flatt. Working mechanism of viscosity-modifying admixtures. In *Science and Technology of Concrete Admixtures*, pages 415–432. Elsevier, 2016.

B. Panda, S. Chandra Paul, and M. Jen Tan. Anisotropic mechanical performance of 3D printed fiber reinforced sustainable construction material. *Materials Letters*, 209:146–149, 2017.

B. Panda, S. C. Paul, N. A. N. Mohamed, Y. W. D. Tay, and M. J. Tan. Measurement of tensile bond strength of 3D printed geopolymer mortar. *Measurement*, 113:108–116, 2018.

B. Panda, N. A. Noor Mohamed, S. C. Paul, G. Bhagath Singh, M. J. Tan, and B. Šavija. The Effect of Material Fresh Properties and Process Parameters on Buildability and Interlayer Adhesion of 3D Printed Concrete. *Materials*, 12(13), 2019.

A. Paolini, S. Kollmannsberger, and E. Rank. Additive manufacturing in construction: A review on processes, applications, and digital planning methods. *Additive Manufacturing*, 30:100894, 2019.

A. Papo. Rheological models for cement pastes. *Materials and Structures*, 21(1):41–46, 1988.

S. C. Paul, Y. W. D. Tay, B. Panda, and M. J. Tan. Fresh and hardened properties of 3D printable cementitious materials for building and construction. *Archives of Civil and Mechanical Engineering*, 18(1):311–319, 2018.

J. Pegna. Exploratory investigation of solid freeform construction. *Automation in Construction*, 5(5):427–437, 1997. ISSN 09265805.

A. Perrot. *3D Printing of Concrete: State of the Art and Challenges of the Digital Construction Revolution*. John Wiley & Sons, 2019.

A. Perrot, D. Rangeard, and A. Pierre. Structural built-up of cement-based materials used for 3D-printing extrusion techniques. *Materials and Structures*, 49(4):1213–1220, 2016.

J.-Y. Petit, E. Wirquin, and B. Duthoit. Influence of temperature on yield value of highly flowable micromortars made with sulfonate-based superplasticizers. *Cement and Concrete Research*, 35(2):256–266, 2005.

J.-Y. Petit, K. H. Khayat, and E. Wirquin. Coupled effect of time and temperature on variations of yield value of highly flowable mortar. *Cement and Concrete Research*, 36(5):832–841, 2006.

U. Pott and D. Stephan. Penetration test as a fast method to determine yield stress and structural build-up for 3D printing of cementitious materials. *Cement and Concrete Composites*, 121: 104066, 2021.

A. V. Rahul and M. Santhanam. Evaluating the printability of concretes containing lightweight coarse aggregates. *Cement and Concrete Composites*, 109:103570, 2020.

S. Ramakrishnan, S. Muthukrishnan, J. Sanjayan, and K. Pasupathy. Concrete 3D printing of lightweight elements using hollow-core extrusion of filaments. *Cement and Concrete Composites*, 123:104220, 2021.

G. Rapp. Über die Rohrförderung von Leichtbeton. *Zeitschrift Beton*, 5:182 ff., 1971.

W. E. Reilly. Hydrothermal and Vacuum Saturated Lightweight Aggregate for Pumped Structural Concrete. In *Journal Proceedings*, volume 69, pages 428–432, 1972.

L. Reiter. *Structural Build-up for Digital Fabrication with Concrete - Materials, Methods and Processes*. Dissertation, ETH Zurich, 2019.

L. Reiter, T. Wangler, N. Roussel, and R. J. Flatt. The role of early age structural build-up in digital fabrication with concrete. *Cement and Concrete Research*, 112:86–95, 2018.

M. Rossig. *Fördern von Frischbeton, insbesondere von Leichtbeton, durch Rohrleitungen.* Springer, 1974.

N. Roussel. A thixotropy model for fresh fluid concretes: Theory, validation and applications. *Cement and Concrete Research*, 36(10):1797–1806, 2006.

N. Roussel, editor. *Understanding the Rheology of Concrete.* Woodhead Publishing in materials. Elsevier, 2012. ISBN 9780857090287.

N. Roussel. Rheological requirements for printable concretes. *Cement and Concrete Research*, 112:76–85, 2018.

N. Roussel and F. Cussigh. Distinct-layer casting of SCC: The mechanical consequences of thixotropy. *Cement and Concrete Research*, 38(5):624–632, 2008.

N. Roussel, C. Stefani, and R. Leroy. From mini-cone test to Abrams cone test: measurement of cement-based materials yield stress using slump tests. *Cement and Concrete Research*, 35 (5):817–822, 2005.

N. Roussel, G. Ovarlez, S. Garrault, and C. Brumaud. The origins of thixotropy of fresh cement pastes. *Cement and Concrete Research*, 42(1):148–157, 2012.

E. Sakai, T. Kasuga, T. Sugiyama, K. Asaga, and M. Daimon. Influence of superplasticizers on the hydration of cement and the pore structure of hardened cement. *Cement and Concrete Research*, 36(11):2049–2053, 2006.

T. Salet and R. Wolfs. Potentials And Challenges In 3D Concrete Printing. *Proceedings of the 2nd International Conference on Progress in Additive Manufacturing, Singapur*, pages 8–13, 2016.

F. Sartipi and A. Sartipi. Brief review on advancements in construction additive manufacturing. *Journal of Construction Materials*, 1:2–4, 2020.

W. R. Schowalter and G. Christensen. Toward a rationalization of the slump test for fresh concrete: comparisons of calculations and experiments. *Journal of Rheology*, 42(4):865–870, 1998.

E. Secrieru. *Pumping behaviour of modern concretes: Characterisation and prediction.* Dissertation, TU Dresden, 2018.

E. Secrieru, S. Fataei, C. Schröfl, and V. Mechtcherine. Study on concrete pumpability combining different laboratory tools and linkage to rheology. *Construction and Building Materials*, 144: 451–461, 2017.

E. Secrieru, D. Cotardo, V. Mechtcherine, L. Lohaus, C. Schröfl, and C. Begemann. Changes in concrete properties during pumping and formation of lubricating material under pressure. *Cement and Concrete Research*, 108:129–139, 2018.

R. Springenschmid. *Betontechnologie für die Praxis.* Beuth Verlag GmbH, 2018. ISBN 9783410244660.

A. Suiker, R. Wolfs, S. M. Lucas, and T. Salet. Elastic buckling and plastic collapse during 3D concrete printing. *Cement and Concrete Research*, 135, 2020.

A. S. Suiker. Mechanical performance of wall structures in 3D printing processes: Theory, design tools and experiments. *International Journal of Mechanical Sciences*, 137:145–170, 2018.

K. Takahashi and T. A. Bier. Mechanisms of degradation in rheological properties due to pumping and mixing. *Advances in Civil Engineering Materials*, 3(2):25–39, 2014.

G. H. Tattersall and P. F. G. Banfill. *The rheology of fresh concrete.* Pitman Books Limited, Boston and London, 1983.

Y. W. D. Tay, B. Panda, S. C. Paul, N. A. Noor Mohamed, M. J. Tan, and K. F. Leong. 3D printing trends in building and construction industry: a review. *Virtual and Physical Prototyping*, 12(3):261–276, 2017.

K.-C. Thienel. Materialtechnologische Eigenschaften der Leichtbetone aus Blähton. *Baustoffe in Praxis, Lehre und Forschung: Festschrift zum 65. Geburtstag von Prof. Dr.-Ing, Rostásy, FS Schmidt-Döhl, F.(eds.)*, pages 203–210, 1992.

K.-C. Thienel. *Gefügedichter und haufwerksporiger Leichtbeton.* Hochschulschrift, Universität der Bundeswehr München, 2018.

K.-C. Thienel, F. Schmidt-Döhl, and V. Feldrappe. In-situ tests on existing LWAC structures. *Proceedings of the Second International Conference on Structural Lightweight Aggregate Concrete, Kristiansand, Norway*, 2000.

K.-C. Thienel, T. Haller, and N. Beuntner. Lightweight concrete—From basics to innovations. *Materials*, 13(5):1120, 2020.

L. N. Thrane, H. Stang, and M. R. Geiker. Flow induced segregation in full scale castings with SCC. In *5th International Symposium on Self-Compacting Concrete*, pages 449–454, 2007.

W. Urschel and J. Urschel. Wall building machine, 1941. URL https://www.youtube.com/watch?v=nkxe9uK8jSo.

H. Vikan and H. Justnes. Influence of silica fume on rheology of cement paste. In *3rd International Symposium on Self-Compacting Concrete*, pages 190–201, 2003.

J. Vosahlik, K. A. Riding, D. Feys, W. Lindquist, L. Keller, S. van Zetten, and B. Schulz. Concrete pumping and its effect on the air void system. *Materials and Structures*, 51(4):94, 2018.

J. E. Wallevik. Thixotropic investigation on cement paste: Experimental and numerical approach. *Journal of Non-Newtonian Fluid Mechanics*, 132(1-3):86–99, 2005.

J. E. Wallevik and O. H. Wallevik. Analysis of shear rate inside a concrete truck mixer. *Cement and Concrete Research*, 95:9–17, 2017.

O. H. Wallevik and J. E. Wallevik. Rheology as a tool in concrete science: The use of rheographs and workability boxes. *Cement and Concrete Research*, 41(12):1279–1288, 2011.

T. Wangler, E. Lloret, L. Reiter, N. Hack, F. Gramazio, M. Kohler, M. Bernhard, B. Dillenburger, J. Buchli, N. Roussel, and R. Flatt. Digital Concrete: Opportunities and Challenges. *RILEM Technical Letters*, 1:67, 2016.

T. Wangler, N. Roussel, F. P. Bos, T. Am Salet, and R. J. Flatt. Digital concrete: a review. *Cement and Concrete Research*, 123:105780, 2019.

R. Weber. *Rohrförderung von Beton.* Beton-Verlag, Düsseldorf, 1963.

H. Weigler and S. Karl. *Stahlleichtbeton. Herstellung, Eigenschaften, Ausführung.* Bauverlag GmbH, Wiesbaden, 1972.

K. Wesche. *Baustoffe für tragende Bauteile 2 - Beton, Mauerwerk.* Bauverlag GmbH, Wiesbaden und Berlin, 1993. ISBN 978-3-322-80188-3.

S. Winter, K. Henke, and D. Talke. *Additive Fertigung frei geformter Bauelemente durch numerisch gesteuerte Extrusion von Holzleichtbeton.* Abschlussbericht. Fraunhofer IRB Verlag (Forschungsinitiative Zukunft Bau, F3002), Technische Universität München, 2016.

R. Wolfs, F. P. Bos, and T. Salet. Early age mechanical behaviour of 3D printed concrete: Numerical modelling and experimental testing. *Cement and Concrete Research*, 106:103–116, 2018.

R. J. M. Wolfs and A. S. J. Suiker. Structural failure during extrusion-based 3D printing processes. *The International Journal of Advanced Manufacturing Technology*, 104(1-4):565–584, 2019.

B. Zareiyan and B. Khoshnevis. Effects of interlocking on interlayer adhesion and strength of structures in 3D printing of concrete. *Automation in Construction*, 83:212–221, 2017a.

B. Zareiyan and B. Khoshnevis. Interlayer adhesion and strength of structures in Contour Crafting - Effects of aggregate size, extrusion rate, and layer thickness. *Automation in Construction*, 81:112–121, 2017b.